

SEASONAL EVOLUTION OF THE MODES OF INTERANNUAL
VARIABILITY OF THE SOUTH AMERICAN MONSOON

A THESIS SUBMITTED TO THE
GRADUATE DIVISION OF THE
UNIVERSITY OF HAWAI'I AT MĀNOA
IN PARTIAL FULFILLMENT OF THE
REQUIREMENTS FOR THE DEGREE OF

MASTER OF SCIENCE

IN

METEOROLOGY

MAY 2000

By

Alejandro T. Ludert

Thesis Committee:

Dr. Bin Wang, Chairperson

Dr. Pao-Shin Chu

Dr. Fei-Fei Jin

We certify that we have read this thesis and that, in our opinion, it is satisfactory in scope and quality as a thesis for the degree of Master of Science in Meteorology .

THESIS COMMITTEE

Chairperson

Copyright 2000 by
Alejandro T. Ludert

Grandparents, Parents and Uncles,
Grandparents, Parents and Uncles,
from good springs, good rivers flow.
Grandparents, Parents and Uncles.

ACKNOWLEDGMENTS

I wish to thank Professor Bin Wang for his support and advise during my Masters work. I also wish to greatly thank Professors Pao-Shin Chu and Fei-Fei Jin for agreeing to participate in my thesis work as committee members.

This work would not have been possible without the help of Dr. June-Yi Lee. I would also like to thank Dr. Analissa Cherchi, Dr. Andrea Alessandri and Dr. Baoqiang Xiang as well as the other members of our research group for their truly valuable feedback during the development stages of this work.

I would like to thank my fellow graduate students, Aaron Levine, Owen Shieh, Gary Grunseich, Kavina Dayal for the fruitful discussions as well as all my other classmates and graduate students of the department that help create an agreeable work environment.

Finally I would like to thank my parents and family for their never dwindling support and love from afar and Erin Edkins for her love and support here at home.

ABSTRACT

This work focuses on the interannual variability of precipitation during the December-January-February (DJF) season and the seasonal evolution of the modes of variability of precipitation from September to May over the South American continent. For this, we use Empirical Orthogonal Function (EOF) and Seasonal reliant EOF (S-EOF) analysis as well as area averaged precipitation anomalies over Eastern Brazil to characterize precipitation variability over the region.

Using EOF analysis we find that the dominant mode of DJF variability of interannual and longer time scales is characterized by strong precipitation anomalies over Eastern Brazil and anomalies of opposite sign over South East South America (SESA) and the western part of the Amazon Basin. This mode is referred to as the Continental tripole mode in this study. This dominant DJF mode is a robust feature across all datasets examined and shows little correlation to SST anomalies. The second DJF mode is characterized by a meridional dipole of precipitation anomalies forced by ENSO SST anomalies. During SON the first two leading modes of precipitation variability are related to Pacific SST anomalies. The first SON EOF mode is related to SST anomalies over the central Pacific and is characterized by a dipole of precipitation between SESA and the South Atlantic Convergence Zone (SACZ). The second SON EOF mode is related to eastern Pacific SST anomalies and is characterized by a meridional dipole of precipitation over South America. During MAM, the dominant EOF mode is the meridional dipole mode forced by ENSO SST anomalies. Due to the weak relationship between the DJF continental tripole mode (EOF 1) of variability and contemporary SST anomalies, Grimm and Zilli (2009) proposed that precipitation anomalies during the previous SON season may, via local surface-atmosphere interactions, be a contributing factor to the development of this DJF mode. This hypothesis is based on the significant correlation between the time series of the SON EOF 1 and the DJF EOF 1. This type of relationship is only weakly or not at all reproduced by the datasets used in this study.

Using Seasonal reliant EOF analysis (S-EOF) we achieve a clear separation of the seasonally evolving modes of variability of the South American monsoon from 1948-2010 into two individual modes. The first S-EOF mode is strongly linked to ENSO SST anomalies and captures the seasonal evolution of the meridional dipole of precipitation between northern South America and Southern South America. The second S-EOF mode captures the DJF continental tripole of precipitation anomalies and during the preceding SON season shows precipitation anomalies of opposite sign over SESA and the SACZ, supporting the previously observed seasonal evolution of this mode. SST anomalies associated with this second S-EOF mode show negative SSTs over the southern Atlantic underlying the SACZ and weak positive SSTs over the central-western Pacific. S-EOF analysis for the epochs 1948-1979 and 1979-2010 show significant decadal variability of both S-EOF modes. The ENSO related meridional dipole mode is similar in spatial structure and seasonal evolution in both epochs and is the dominant mode of variability during the second epoch but not during the first (accounting for 12% of observed variance during the first epoch and 19% of the variance during the second). This change may be a response to more frequent intense El Niño events during the 1979-2010 period than during the 1948-1979 period. The non-ENSO continental tripole mode is the dominant mode of variability during the 1948-1979 period (13% of observed variance) but is relegated to the second S-EOF mode during the second period (12% of variance) and has markedly different seasonal evolution from SON to DJF. During the 1948-1979 period the continental tripole mode is lead by a dipole of opposite precipitation anomalies over the SESA and the SACZ as observed in the 1948-2010 period and reported in previous studies, but during the 1979-2010 period, the continental tripole mode is lead during the previous SON season by precipitation anomalies of the same sign not showing reversal of anomalies over SESA and the SACZ as shown for the 1948-1979 period. The origin of this changes on decadal time scales are not clear, it appears that precipitation anomalies of opposite sign during the previous SON season serve to intensify the DJF continental tripole mode making it the dominant S-EOF mode during the 1948-1979 period, but are not a necessary factor for the establishment of the DJF continental tripole

mode.

To directly analyse the variability of precipitation over Eastern Brazil, the Eastern Brazil Precipitation Index (EBPI) was defined as the area averaged precipitation anomaly over Eastern Brazil from the Equator to 20S and from 55W to 30W. Analysis using the EBPI index show that there is an abrupt change in the precipitation patterns over Eastern Brazil and SESA from December to January. Regressions of the Continental Tripole mode EOF, S-EOF time series as well as of the January-February EBPI time series to 200mb geopotential heights show that the Continental Tripole mode is strongly linked to an upper level vortex over South America. Using precipitation and 200mb geopotential height pentad data it appears that the upper level circulation appears two pentads before precipitation anomalies associated with the Continental Tripole mode appear and disappears one pentad before precipitation anomalies disappear. This leads us to propose that the upper level cyclone over South America is a major contributing factor to the establishment of the Continental Tripole mode.

Using one month lead seasonal hindcasts from the Coupled Ocean-Atmosphere Global Circulation Models participating in the ENSEMBLES intercomparison project we estimated the performance of the MME in capturing the seasonal evolution of the main modes of variability of South American Precipitation. The ENSO driven mode of variability accounts for most of the variance of precipitation in the MME and compares quite well to the S-EOF mode of observations in terms of temporal variability and spatial patterns of precipitation anomaly for each season. A mode of variability similar to the continental Tripole mode is produced by the MME and captured in the third S-EOF mode of the MME precipitation. This mode shows some similarities to the Continental Tripole mode seen in observations but it is clear that the MME seasonal hindcasts has great difficulty capturing this mode of variability.

TABLE OF CONTENTS

Acknowledgments	v
Abstract	vi
List of Tables	xii
List of Figures	xiii
1 Introduction	1
1.1 The South American Monsoon System (SAMS)	1
1.2 General features of the SAMS.	3
1.2.1 Main structure of the SAMS.	3
1.2.2 Indices for the characterization of SAMS.	7
1.2.3 Evolution and life cycle of SAMS.	9
1.3 SAMS variability.	10
1.3.1 Intraseasonal variability.	10
1.3.2 Interannual Variability.	13
1.3.3 Decadal and Interdecadal variability.	19
1.4 Modeling, prediction and predictability of SAMS.	22
1.5 Scientific questions addressed in this study.	25
2 Materials and Methods	27
2.1 Datasets	27
2.2 Methodology	28
3 The South American Monsoon domain and its variability as observed from EOF and S-EOF analysis.	31

3.1	The South American Monsoon Domain in PREC/L precipitation data. . . .	31
3.2	Results from the standard EOF analysis	34
3.2.1	Precipitation variability in the PREC/L precipitation dataset for the SON DJF and MAM seasons	34
3.2.2	Comparison between the variability captured by EOF analysis in PREC/L, CMAP and GPCP precipitation datasets and the importance of the EOF domain used to study the South American Monsoon	44
3.3	Results from the S-EOF analysis	50
3.3.1	S-EOF analysis of GPCP precipitation data and comparison to PREC/L S-EOF results.	58
3.4	Summary	68
4	Direct study of Eastern Brazil precipitation anomalies, their interannual variability and seasonal evolution.	72
4.1	The Eastern Brazil Precipitation Index as a tool to understand the variability of precipitation over South America.	72
4.1.1	Regression analysis of atmospheric variables onto EBPI.	74
4.1.2	Mean state change over the Indian Ocean From December to January.	82
4.1.3	Eastern Brazil Precipitation Index analysis of GPCP.	86
4.2	Summary	93
5	The seasonal evolution of precipitation variability as captured by a Multi-Model ensemble of Coupled Ocean Atmosphere models.	96
5.1	Summary	103
6	conclusion	105
A	Auxiliary figures for the S-EOF analysis of GPCP and PREC/L data for the period 1979-2010.	112
B	Auxiliary Figures for the Eastern Brazil Precipitation Index Analysis .	114
C	Auxiliary figures from Chapter 4, Section 4.1.3	116

Bibliography **120**

LIST OF TABLES

3.1	Correlation tables between the first three modes of SON and DJF (top table) and DJF and MAM (bottom table). The correlation values with one, two and three asterisks are significant at the 80, 90 and 95 % test level according to a non-naive student t test with a corrected sample size calculated as shown in chapter 2.	42
3.2	Correlation tables between the first two SON EOF modes, the first two DJF EOF modes and the first MAM EOF mode for GPCP (top) and CMAP (bottom) data. The correlation values with one and two asterisks are significant at the 99% test level according to a non-naive student t test with a corrected sample size calculated as shown in chapter 2.	50
4.1	Correlation table between the DJF EOF 1 Principal Component, the S-EOF 2 Principal Component, The DJF EBPI, and the monthly EBPI for December, January and February. Correlations with an asterisk are significant at the 99% test level.	74
5.1	Correlation table between the first three S-EOF modes of observations and MME seasonal forecast. Correlations values with an asterisk are significant at the 90% test level.	99

LIST OF FIGURES

1.1	South American transboundry river basins along with the regions of interest for this study, the Amazon River Basin (ARB), the Nordeste region (NOR), The South Atlantic Convergence Zone (SACZ) and the Southeast South America region (SESA). Figure adapted from the Transboundary Freshwater Spatial Database of Oregon State University, available at http://www.transboundarywaters.orst.edu/database/	2
1.2	Seasonal mean precipitation and standard deviation for JJA, SON, DJF and MAM seasons as captured by NOAA’s Precipitation Reconstruction Over Land (PREC/L dataset) for the period 1984-2011.	4
1.3	First four EOFs (a-d), which explain 37.3% of the variance and REOFs (e-h), which explain 27.7% of the variance for filtered data in the 30/70 day band. From Grimm et al. (2005)	11
1.4	Composite of rainfall anomalies and integrated moisture flux for the Wet phase of REOF 1 (a) and REOF 2 (b) and Dry phase (c and d respectively) for filtered 30/70 band data. From Grimm et al. (2005).	12
1.5	First EOFs for spring and summer. Reproduced from Grimm (2011).	15
3.1	Monsoon precipitation index, MPI (color shading) and monsoon precipitation domain (Black contours) in the CMAP, PREC-L and GPCP datasets. The Monsoon domains here shown are defined as areas with MPI greater than 0.5 and annual precipitation range of above 300mm (see text for details).	33
3.2	Spatial patters of the first three EOF modes of variability for SON (top three panels), DJF (middle three panels) and MAM (bottom three panels) in the PREC/L dataset. The Eigenvectors here presented have been multiplied by the standard deviation of their corresponding PC time series, so that the shading at each gridpoint represents the amount of loading contributed by that gridpoint to the variance of that mode.	36
3.3	PC time series of the first three DJF EOF modes present in PREC-L data along with the power spectrum corresponding to each time series. PC time series presented here have been normalized by their corresponding standard deviation. The red curves in the power spectra represent the spectra of a red noise process fitted to each time series.	38

3.4	Spatial maps of correlation to SST anomalies. Panels A, B and C show the correlations of SON EOF 1, 2 and 3 to contemporary SON SST anomalies. Panels D, E and F, correlations of DJF EOF 1, 2 and 3 to contemporary DJF SSTAs. Panels G, H and I, correlations of MAM EOF 1, 2, and 3 to contemporary MAM SSTAs. Contours represent areas where the correlations are significant at the 90% test level according to a non-naive Student t-test with a modified sample size at each grid-point according to the procedure shown Chapter 2.	40
3.5	Eigenvector maps, principal components and maps of correlation between PCs and SSTAs for the first two SON modes of GPCP and CMAP data. PCs presented here are normalized by their corresponding standard deviation. SST maps show contours of 95% significance level.	46
3.6	Same as in figure 3.5 but for DJF EOF mode 1 and 2.	48
3.7	Same as in figure 3.5 but for DJF EOF mode 1.	49
3.8	Spatial patterns of the first three Seasonal EOF modes of variability in the PREC/L dataset. Each column in this figure represents a single Eigenvector of the S-EOF process which has been remapped into a three season sequence.	51
3.9	Spatial maps of correlation to SST anomalies. Panels A, D and G (left three panels) show the correlation between the S-EOF 1 Principal component and the contemporary SON, DJF and MAM SST anomaly at each gridpoint. Panels B, E and H show the same but for the principal component of S-EOF 2 and panels C, F and I for the principal component of S-EOF 3. Contours represent areas where the correlations are significant at the 95% test level according to a non-naive Student t-test with a modified sample size at each grid-point according to the procedure shown Chapter 2.	52
3.10	Principal Components of the first three S-EOF modes of variability in PREC/L precipitation anomalies and their corresponding power spectra.	54
3.11	Lead-lag correlation coefficients of Niño3.4 SST index to the first three PC of the S-EOF analysis of PREC/L precipitation over South America. The green line represents the 95% significance level according to a naive Student t test.	56
3.12	Regression of the first three PCs of the S-EOF analysis of PREC/L precipitation over South America to 200mb wind anomalies. Shading shows areas where at least one of the components has a 95% significant correlation to the corresponding PC.	57

3.13	Percentage of variance explained by each of the first three S-EOF modes of GPCP and PREC/L for the period 1979-2010. Error bars are calculated according to the North et al. (1982) rule of thumb.	59
3.14	Eigenvector maps of the first three S-EOF modes of GPCP and PREC/L data for the period 1979-2010. The numbers inside the parenthesis represent the % variance explained by each mode.	60
3.15	PC time series of the first three S-EOF modes of GPCP (black) and PREC/L (red) data for the period 1979-2010. Correlations between the PC time series are 0.98 for S-EOF 1, 0.94 for S-EOF 2 and 0.23 for S-EOF 3.	62
3.16	Percentage of variance explained by each of the first three S-EOF modes of PREC/L for the periods 1948-1979 and 1979-2010. Error bars are calculated according to the North et al. (1982) rule of thumb.	63
3.17	Eigenvector maps of the first three S-EOF modes of PREC/L data for the sub-periods 1948-1979 and 1979-2010. The numbers inside the parenthesis represent the % variance explained by each mode.	64
3.18	SST correlation maps between the PC time series of the first three S-EOFs of PREC/L precipitation for the 1948-1979 period. Contours represent areas where the correlations are significant at the 95% test level according to a non-naive Student t-test with a modified sample size at each grid-point according to the procedure shown Chapter 2.	65
3.19	Same as in figure 3.18 but for the 1979-2010 period.	66
3.20	200mb Hgt regression maps between the PC time series of the first three S-EOFs of PREC/L precipitation for the 1948-1979 period. Shading represent areas where the correlations are significant at the 95% test level according to a non-naive Student t-test with a modified sample size at each grid-point according to the procedure shown Chapter 2.	67
3.21	Same as in figure 3.20 but for the 1979-2010 period.	69
4.1	Climatological mean DJF precipitation from the PREC/L dataset from 1948-2011, standard deviation of DJF seasonal mean precipitation and first DJF EOF mode of PREC/L data for the same period. The black boxes over the maps represent the area where the EBPI is defined.	73

4.2	Regression maps of monthly precipitation anomalies onto the Jan-Feb EBPI time series, red colors are positive anomalies and blue colors are negative anomalies in units of mm/day. Black contours outline regions where the correlation between precipitation anomaly and EBPI is significant at the 90% test level.	75
4.3	Regression maps of monthly 200mb geopotential height anomalies onto the Jan-Feb EBPI time series. Contour interval is 4m and solid and dashed contours represent positive and negative values respectively. Gray shaded areas show regions where the correlation between geopotential height anomaly and EBPI is significant at the 90% test level.	77
4.4	Map of SST correlations to EBPI precipitation time series. Contoured areas show regions where the correlation between SST anomaly and EBPI is significant at the 90% test level.	78
4.5	Regression of 200mb wind anomalies onto EBPI over the South American continent. Shaded areas show regions where the correlation EBPI and at least one of the wind component anomalies is significant at the 90% test level.	79
4.6	Same as in figure 4.6 but for 850mb winds anomalies.	80
4.7	925mb winds (upper panels) and specific humidity (lower panels) regressed onto the EBPI time series for the months of December, January and February. Grey areas in the wind anomaly maps represent areas where the correlation between the EBPI time series and at least one of the wind components is significant at the 90% test level. Specific humidity is in units of grams per kilogram and contours represent areas where the correlation between EBPI and specific humidity anomalies is significant at the 90% test level.	81
4.8	December, January and February monthly mean fields of GPCP precipitation from 1979-2010 (top three panels), 850mb geopotential heights from NCEP reanalysis (Mid three panels) and ERSST sea surface temperatures (bottom three panels). Precipitation is in units of mm/day, geopotential heights in units of meters with contour intervals every 20 meters and SST in Celsius with contour intervals every two Celsius.	82
4.9	Spatial maps of January mean state minus December mean state for precipitation (units of mm/day), 850mb height (units of meters with contour intervals every 5 meters), 925mb specific humidity (in units of grams/kilogram) and 925mb wind divergence (in units of $10^{-6}s^{-1}$)	84

4.10	EBPI regressed to 200mb anomalies (contours) and January-December 200mb zonal wind (red shading). Gray hashing regions shows regions where the correlation between EBPI and 200mb geopotential height anomalies are significant at the 90% test level.	85
4.11	Regression maps of monthly GPCP precipitation anomalies onto the Jan-Feb EBPI time series calculated from GPCP data for the period 1980-2010. Red colors are positive anomalies and blue colors are negative anomalies in units of mm/day. Black contours outline regions where the correlation between precipitation anomaly and EBPI is significant at the 90% test level.	88
4.12	Correlations of the JanFeb. EBPI index to individual pentads. Points marked with orange Xs show pentads for when the correlation between JanFeb EBPI and the EBPI for that individual pentad is significant at the 95% test level.	89
4.13	Regression maps of GPCP pentad anomalies to the EBPI calculated from GPCP for the pentads spanning from Jan 16 to Feb 9 (pentads 3 to 7 of the year). The numbers in parenthesis represent the lead of lag of the pentads with respect to the EBPI time series, see text for details. Contours indicate areas where correlations between the EBPI and the pentad precipitation anomalies are significant at the 90% test level.	90
4.14	Regression maps of NCEP 200mb geopotential height pentad anomalies to the EBPI calculated from GPCP for the pentads spanning from Jan 16 to Feb 9 (pentads 3 to 7 of the year). The numbers in parenthesis represent the lead of lag of the pentads with respect to the EBPI time series, see text for details. Shading indicate areas where correlations between the EBPI and the pentad precipitation anomalies are significant at the 90% test level.	91
5.1	Correlation skill maps of MME seasonal precipitation forecast for the period 1982-2005 as compared to GPCP precipitation data for the same period. Dashed contours represent areas of 90% significance while solid contours represent areas of 95% significance.	97
5.2	Eigenvector maps of the first three S-EOF modes of PREC/L precipitation and MME seasonal forecast for the period spanning 1960-2005. The Eigenvectors here have been multiplied by the standard deviation of their corresponding PC so that the shading represents the amount of loading contributed to a particular mode by a particular grid point in a particular season. Areas with values between -0.01 and 0.01 have been made white to facilitate differentiation between negative and positive areas.	98
5.3	Correlation maps of the PC time series of the first three MME seasonal forecast S-EOF modes to MME SST anomalies. Contours denote areas where correlations are significant at the 95% test level.	101

5.4	Regression maps of the PC time series of the first three MME seasonal forecast S-EOF modes to MME 200mb wind anomalies. Shading denote areas where correlations are significant at the 99% test level for the S-EOF 1 panels and the 90% test level for the S-EOF2 and S-EOF 3 panels.	102
A.1	Correlation maps of the first three S-EOF modes of GPCP data 1979-2010 to seasonal SST anomalies. Maps A, D and G represent the correlation of PC 1 to seasonal SST anomalies. Maps B, E and F represent the correlations for PC2 while C, F and I the correlations for PC3. Contours show areas where the correlations are significant at the 90% test level.	112
A.2	Correlation maps of the first three S-EOF modes of PREC/L data 1979-2010 to seasonal SST anomalies. Maps A, D and G represent the correlation of PC 1 to seasonal SST anomalies. Maps B, E and F represent the correlations for PC2 while C, F and I the correlations for PC3. Contours show areas where the correlations are significant at the 90% test level.	113
B.1	Regression maps of monthly 850mb geopotential height anomalies onto the Jan-Feb EBPI time series. Contour interval is 4m and solid and dashed contours represent positive and negative values respectively. Gray shaded areas show regions where the correlation between geopotential height anomaly and EBPI is significant at the 90% test level.	114
B.2	Monthly mean precipitation maps over the Indian Ocean for the months of September through May from GPCP precipitation data 1979-2010. Precipitation in units of mm/day.	115
C.1	Correlation maps of GPCP January-February EBPI index to monthly precipitation anomalies. Contours show areas where the correlations are significant at the 90% test level.	116
C.2	Regression maps of GPCP January-February EBPI index to monthly 200mb geopotential height anomalies. Shading show areas where the correlations are significant at the 90% test level.	117
C.3	Correlation maps of GPCP January-February EBPI index to monthly SST anomalies. Contours show areas where the correlations are significant at the 90% test level.	118

C.4 Regression of the EBPI index calculated using only pentad 3, Jan 16-20 to precipitation and 200mb HGT anomalies. Contours in anomaly maps and shading in geopotential height maps show regions where the EBPI time series and the pertinent variable show correlations significant at the 90% significance level. 119

CHAPTER 1

INTRODUCTION

1.1 The South American Monsoon System (SAMS)

The South American continent extends from 10N to 55S and occupies 17 million square kilometres. The considerable meridonal extent of the continent make it so that it exhibits diverse weather patterns including tropical, subtropical and extratropical features. South America has an estimated population of 385 million people of which 85% are located in urban areas and 15% in rural areas. The South American monsoon system is responsible for the precipitation over most of the South American continent which is heavily dependent on this rainfall for hydroelectric power and crop irrigation. The Andes cordillera extends continuously along the western coast of the continent with elevations in excess of 4 km and a large plateau area, the Altiplano, at around 3.8km above sea level and an approximate 100 000 km²area. To the east of the Andes the Amazon River Basin is one of the largest and most densely vegetated areas in the world, holding an estimated 45% of the worlds liquid fresh water reserve and acting as the worlds largest CO₂ sink. Figure 1.1 has a schematic depiction of the different regions relevant to the discussion of the SAMS including the Amazon River Basin, the Nordeste region of Brazil, the South Atlantic Convergence Zone region and the south-eastern South America (SESA) or subtropical region. The exact definition of these geographical regions may vary from author to author but in general we may use them to describe our findings.

The South American rainfall patterns and their variability have been the object of study for decades and gained momentum since the advent of satellite observations that provided an insight into the precipitation patterns over the largely unpopulated areas of the Amazonia (Kousky, 1988, Horel et al. 1989). Horel et al. (1989) identified the preferred locations of convective activity during the northern and southern hemisphere wet seasons as well as their onset periods. They found that the annual cycle of convective activity has a large



Figure 1.1: South American transboundary river basins along with the regions of interest for this study, the Amazon River Basin (ARB), the Nordeste region (NOR), The South Atlantic Convergence Zone (SACZ) and the Southeast South America region (SESA). Figure adapted from the Transboundary Freshwater Spatial Database of Oregon State University, available at <http://www.transboundarywaters.orst.edu/database/>.

degree of regularity and symmetry about the equator with the maxima of convective activity coinciding with the period maximum solar insolation (DJF in the southern hemisphere and JJA in the northern hemisphere). In spite of these findings, it has been only recently that the South American climate system has been regarded as a monsoon system in the general literature, Zhou and Lau (1998) being among the first to use this description. Zhou and Lau found that although the canonical reversal of low level winds of a monsoon regime was not observed in South America, once the annual mean is removed, a clear reversal of the wind anomalies is observed creating a seasonal cycle of moisture transport and precipitation into the South American monsoon region.

Wang and Ding (2008) define the global monsoon domain in terms of precipitation and westerly wind variability based on the definition of a Monsoon Precipitation Index (MPI) as the annual range of precipitation, wet season mean precipitation minus dry season

precipitation, divided by the annual mean precipitation. In the same way they define a Monsoon Westerly Index using the Annual range of 850mb zonal wind intensity divided by the annual mean of 850mb zonal wind. Using these criteria, the authors propose that areas that show a MPI greater than 0.5 and a annual range of precipitation greater than 300mm be considered monsoon domains, with areas that show and MWI greater than 0.5 be considered "strong" monsoons and areas where the MWI criteria is not met be considered weak monsoons. Using this definition, large areas of the South American continent fall under the "strong" monsoon category, with areas fulfilling the wind criteria being smaller but still present over South America. Considering the climate of South America as a monsoon system provides a useful framework for understanding and diagnosing warm season climate controls and the nature and cause of the climate variability in the region.

1.2 General features of the SAMS.

1.2.1 Main structure of the SAMS.

The South American monsoon system is the dominant climate system during austral summer over South America and can be sometimes considered as a part of the larger monsoon system of the Americas. Like its Asian and African counterparts, SAMS exhibits most of the canonical characteristics of monsoon climate systems including a large annual cycle of precipitation, large-scale land sea temperature contrasts and reversal of the winds (only winds anomalies).

Precipitation over South America south of the Equator peaks during austral summer (DJF) following the march of the maximum solar radiation in a north-west to south-east propagation (Horel et al., 1989). Figure 1.2 shows the seasonal mean accumulated precipitation as well as precipitation standard deviation. For JJA and DJF we can observe that the seasonal cycle has a large degree of symmetry with respect to the equator as well as a large seasonal regularity.

In the western part of the Amazon Basin ($\sim 5^{\circ}\text{S}$), rainfall is abundant year round but can

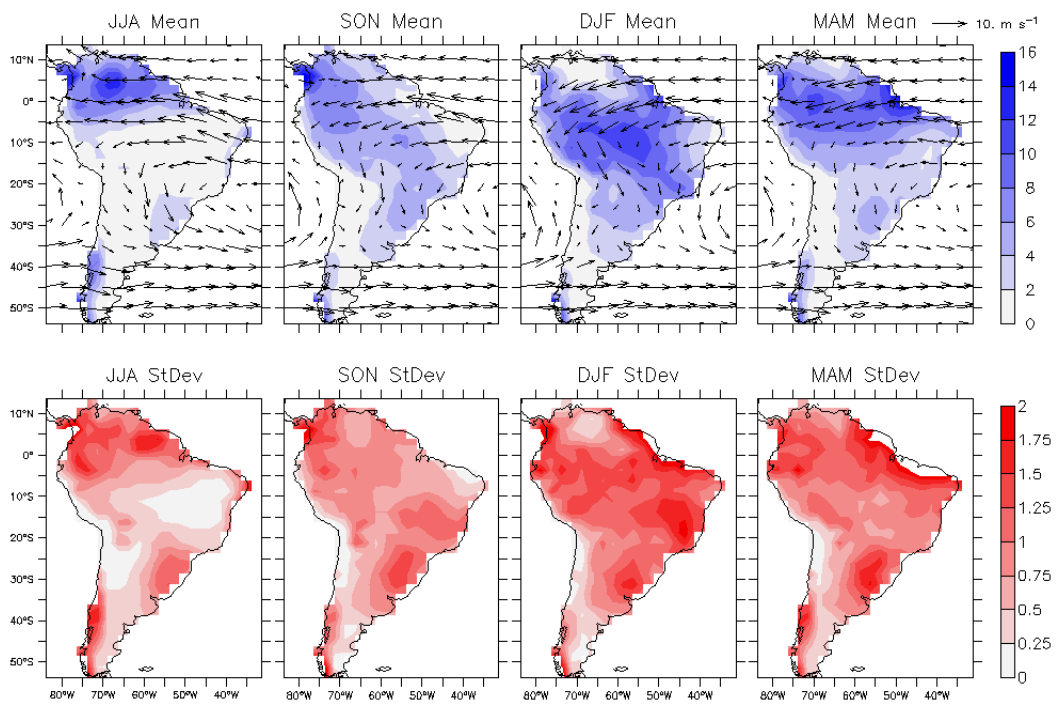


Figure 1.2: Seasonal mean precipitation and standard deviation for JJA, SON, DJF and MAM seasons as captured by NOAA's Precipitation Reconstruction Over Land (PREC/L dataset) for the period 1984-2011.

double from from winter to summer. The largest precipitation contrasts in the SAMS region occur in the central east part of the Amazon Basin ($\sim 10^{\circ}\text{S}$) with almost all rainfall occurring during the summer season. Over the eastern part of the Brazil, rainfall tends to peak slightly later in the season (May-March) due to a later arrival of the ITCZ, which modulates rainfall in this region, that lags the solar maximum. Southeastern Brazil, Paraguay and northern Argentina have essentially even rainfall year round. An important part of the SAMS is the northwest-southeast band of precipitation shown in the DJF panel of 1.2 called the South Atlantic Convergence Zone (SACZ). The establishment of the SACZ is a hallmark of the mature monsoon systems across the South American continent. Moisture flux from the Amazon (as depicted in figure 1.2) is crucial for the maintenance of the SACZ while local topography plays a important role in its location. Southern Hemisphere frontal systems also play a role in the establishment of the SACZ (Garreaud et al., 2009).

A characteristic dipole-like pattern of variability established between the SACZ and the southeast South America region has been identified on a variety of time scales from intraseasonal to interdecadal (Nogues-Paegle and Mo, 1997, Grimm and Zilli, 2009, Grimm, 2011). One phase of the dipole is characterized by enhanced convection in the SACZ and suppressed precipitation to the south while the opposite phase shows reversed patterns. This dipole of variability has been linked to the establishment of circulation anomalies off the southern coast of Brazil that alter the moisture transport of the lower level flow.

As the major solar heating zone migrates south during austral spring and summer, a strong thermal low pressure systems develops over the Chaco region of northern Argentina and western Paraguay. This low pressure area intensifies the inter hemispheric pressure gradient between South America and the northwestern Sahara regions increasing the intensity of the northeasterly trade winds. As these intense and moist trade winds are channelled along the eastern flank of the Andes mountain range they become the northwesterly South America Low Level Jet (SALLJ) responsible for a great deal of the moisture flux into the SAMS region (also seen in figure 1.2). Variability in the SALLJ also plays a role in the dipole of variability mentioned earlier. An enhanced SALLJ is capable of transporting

large amounts of moisture into the SESA region (Silva and Berbery, 2006) and are linked to short term extreme precipitation events in the plains of central Argentina (Liebmann et al., 2004). Over the adjacent oceans, surface high pressure features and corresponding anticyclonic circulations are persistent year round. Convergence between the flow from the Atlantic subtropical high and the SALLJ is also involved in the generation of precipitation over the SACZ and SESA.

In the upper levels, the circulation over South America is characterized by a well defined anticyclonic circulation referred to as the Bolivian High centred near 15S, 65W and an upper level trough near the coast of northeast Brazil usually referred to as the Nordeste low. The origin of the Bolivian high has been attributed to many different phenomena. Gutman and Schewerdtfeger (1965) were among the first to study this upper level circulation and concluded that intense sensible and latent heating over the Andean Altiplano were responsible for the generation of the upper level circulation. Rao and Erdogan (1989) performed a detailed heat budget analysis over the Altiplano and concluded that large amounts of net heating (as strong during January as over the mid- and eastern Tibetan plateau in July) occurred over most of the Altiplano, but did not link it explicitly to the Bolivian high.

Other studies have described the origin of the Bolivian high as a Rossby wave response to the large amounts of latent heat release from convection over the Amazon basin (Silva Dias et al., 1983, DeMaria, 1985). Lenters and Cook (1997) used a GCM, a linear model and observational data and draw similar conclusions, attributing the formation of the Bolivian high and Nordeste low as a response to precipitation over the Amazon, Central Andes and the SACZ, with direct mechanical and sensible heat effect by the Andes being minimal. Chen et al. (1999), studying the stationary eddies in the southern hemisphere during austral summer found that the structure of the Bolivian high-Nordeste low system was formed by a short wave train (wave number 2-6) modulated by a ultra-long wave regime (wave number 1). The authors found that the short-wave exhibited classical monsoon characteristics such as a phase reversal in the midtroposphere and quarter-wavelength shift between the velocity potential fields and the streamfunction divergence fields. They found that the short wave

part of the system may be formed via Sverdrup balance by adiabatic heating and also concluded that remote African heating contributed not only to the intensification of the Nordeste low, but to the formation of the Bolivian high. On the other hand, Garreaud (2000) found no direct cause effect link between Altiplano and Amazon convective activity. Still today there is some debate as to the exact mechanisms behind the formation of the Bolivian high-Nordeste low system (Zhou and Lau, 1998, Liebmann and Mechoso, 2011).

Individual thunderstorms over South America tend to organize into Mesoscale Convective Systems as large scale weather patterns with contiguous precipitation areas and copious amounts of rainfall (Zipser et al., 2006). Sub-tropical MCS over South America are larger and longer lived than those observed in the United States and feature very little polarward migration (Durkee et al., 2009, Durkee and Mote, 2010). Rickenbach et al. (2011) found that MCSs prior to monsoon onset in the west-central Amazon region and in the Nordeste region had a distinct maximum in intensity about 2 months prior to monsoon onset in each region. MCSs in the SACZ and SESA have a weaker and more variable annual cycle in all MCS metrics used in the study, which is likely to be related to the strong influence of baroclinic and frontal systems in those regions.

1.2.2 Indices for the characterization of SAMS.

First efforts in defining a monsoon onset date were set around using OLR as a proxy for precipitation in the South American region. Kousky (1988) defined monsoon onset using pentad average OLR dropping below 240 W/m^2 , provided that it was above this threshold for 10/12 of the preceding pentads and remained below for 10/12 of the following pentads. Using this method, the northwest to southeast migration of precipitation associated with the monsoon transition appears clearly (Kousky 1988, Horel et al. 1989). Marengo et al. (2001) noted that SAMS onset dates using OLR composites were very sensitive to changes in threshold values and that in fact, if the threshold value was doubled, onset direction is reversed and appears to occur from southeast to northwest. Marengo et al. (2001) and Liebmann and Marengo (2001) defined onset in terms of precipitation alone, the latter using

the time variability of the integral of daily increments (S_{day}) of the seasonal precipitation anomaly (annual mean removed) between two dry seasons. This method has the advantage that it depends on precipitation alone, nevertheless, because onset is determined by the change in the curvature of the S_{day} time series, it cannot be used in real time.

Four different monsoon indices using wind data were proposed by Gan et al. (2005) The meridional wind shear index (MWSI), the zonal wind shear index (ZWSI), the 850-hPa zonal wind index (850ZWI) and the 850-hPa zonal and meridional wind index (UVI), all based on the characteristics of the wind circulation, where used to identify the onset and demise dates and intraseasonal variability of the west central Brazil (WCB) region. The MWSI index is directly associated with the local Hadley cell whose meridional variations control monsoon variability over this region, hence strongly linking the MWSI to the variability of the monsoon in WCB. The 850ZWI, UVI and MWSI are well suited for detecting the intraseasonal variability of precipitation in the region, capturing variations in the SALLJ and its transport of moisture into the WCB region.

The large-scale index for South America monsoon (LISAM), proposed by da Silva and de Carvalho (2007) is based on the first combined EOFs of the anomalies of precipitation, specific humidity, air temperature and zonal and meridional winds at 850-hPa. The authors show through correlations between the time coefficient of the LISAM index and the anomaly fields of each variable that LISAM is able to capture appropriately the main spatial features of SAMS. Onset and demise of SAMS was defined when the three-pentad moving average of LISAM became positive or negative, with average onset on pentad 61 (October 28 to November 1) and demise on pentad 58 (October 13 to 17). Sensitivity tests showed that including less variables in the cEOF analysis altered the onset dates, the largest difference occurring when only circulation is considered, spatial patterns of the intraseasonal variability where also significantly altered. The LISAM index is also able to retain the intraseasonal variability of SAMS related to the MJO (30 to 60 day band). Finally, two of the major advantages of the LISAM is that it is continuous in time and therefore properly defined in the wet and dry season and that it does not depend on past observations, and can be use

in real time to diagnose SAMS.

1.2.3 Evolution and life cycle of SAMS.

As discussed in section 1.2.2, different indicators of SAMS activities yield small differences in onset and demise dates of the SAMS, but it is possible to paint a general picture of the monsoon life cycle. During austral spring, a rapid shift occurs in the location of the region of intense convection from the Caribbean and northwestern South America to the southern Amazon basin and the Brazilian highlands reaching south east Brazil by November (compare JJA and SON mean seasonal precipitation in figure 1.2). The relocation of convection and reduction of pressure over the continent shift the Atlantic high eastward. The onset of SAMS is preceded by an increase in northerly cross equatorial surface winds over South America (Marengo et al., 2001, Wang and Fu, 2002) transporting moisture into the region, this, combined with cooling at the top of the boundary layer alter the regional thermodynamic structure and give prime conditions for the onset of convection. Comparing the seasonal mean precipitation maps shown in figure 1.2 we can observe the clear northwest to southeast march of convection from the JJA season to the DJF season. The onset of the wet season typically occurs between the late September and early October and deep convection has been established over most of central South America by November. Onset in the eastern Amazon and northeast Brazil occurs later in the season due to a later arrival of the ITCZ, which is responsible for most convection over these regions.

Transient activity occurring when the atmosphere becomes less stable (Gonzalez et al., 2007) and cold fronts forcing ascent in a thermodynamically primed atmosphere (Raia and Cavalcanti, 2008) have been proposed as possible mechanisms for the quick transition into the monsoon wet season.

SAMS monsoon indices place onset between the 58 pentad of the year for (precipitation based indices by Gan et al. 2004 and Ferreira et al. 2003) and the 62 pentad (wind indices by Gan et al. 2005). The LISAM monsoon index places climatological monsoon onset at pentad 60 (da Silva and de Carvalho 2007). Studies show no apparent association between

SAMS onset and ENSO (Marengo et al. (2001), Gan et al. 2005 and references therein). Ferreira et al. (2003) detect a mixture of late and early onset dates for El Nio and La Nina years in agreement with these results but finds that for the 5N-5S portion of SAMS, onset is influenced by ENSO, with late onsets during El Nio and early onsets during La Nina episodes.

In the beginning of March, the SAMS starts to weaken as the areas of deep convection begin to retreat northwestward as seen in the MAM mean precipitation map shown in figure 1.2. This retreat occurs at faster speeds over the central and western sections of the SAMS region. The northern coastal parts of Brazil still experience rain during April through June, when the ITCZ is at its southernmost position.

1.3 SAMS variability.

1.3.1 Intraseasonal variability.

The intraseasonal variability SAMS DJF precipitation is concentrated over the eastern part of the South American continent affecting primarily the South American see saw variability pattern between the SACZ and SESA (Carvalho et al. (2002), Grimm et al. (2005), Marengo et al. (2010)). Figure 1.3 shows the first four EOFs and rotated EOFs of precipitation filtered to the 30/90 day band, from Grimm et al. (2005).

The first mode of variability represented by EOF 1 (Figure 1.3 a) shows a dipole pattern with strong variability over the SACZ and eastern Brazil and a weaker variability center of opposite sign over SESA. This first mode of variability explains 16.3% of the observed variance. From the REOFs we can see that the first mode of variability can be separated into two modes, one concentrated over central east Brazil (explaining 10% of the variance) and a second mode over the SACZ (explaining 7.3% of the variance). The patterns of variability captured in the first two REOFs are associated with cyclonic and anticyclonic circulation anomalies as shown in Figure 1.4. During the wet phases of REOF 1 and 2, cyclonic anomalies redirect moisture flow from the SALLJ to the eastern Brazil region

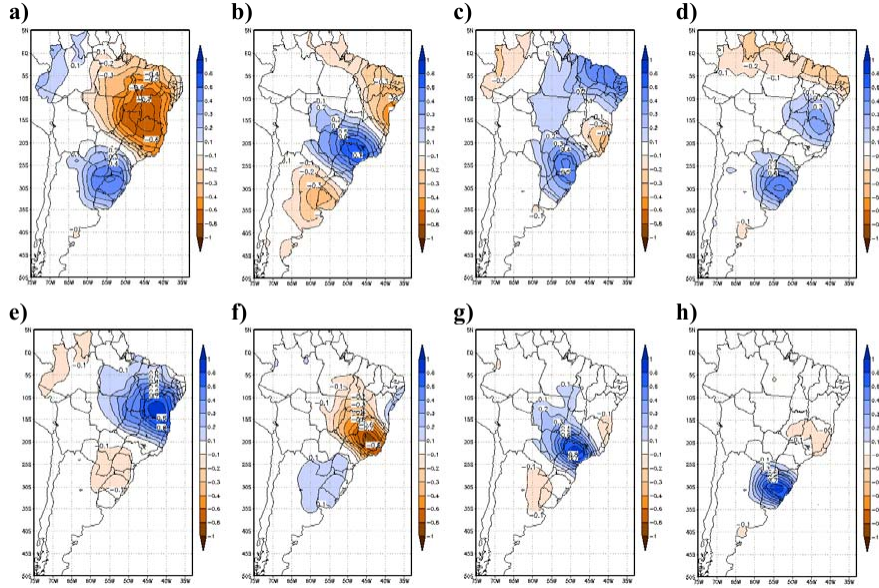


Figure 1.3: First four EOFs (a-d), which explain 37.3% of the variance and REOFs (e-h), which explain 27.7% of the variance for filtered data in the 30/70 day band. From Grimm et al. (2005)

(panel a representing REOF1) and the SACZ (panel b representing REOF2). In the dry phases of the variability pattern, anticyclonic anomalies enhance moisture flux to south east South America and the subtropical plains.

Herdies et al. (2002) identified two distinct regimes of low level winds (easterly and westerly) over the core of the monsoon region (ABARCOS station in the Rondonia State of Brazil, 10deg46minS 62deg20minW). Westerly winds over this region were associated with enhanced convection over the SACZ, the opposite being true during the easterly regime. Jones and Carvalho (2002) found that active and break phases in the monsoon precipitation are associated with reversal of the winds over the Rondonia state. The variability pattern of these active and break phases is oriented from North West to South East, between the central Amazonia region and eastern Brazil.

During the westerly active period, low level cross equatorial flow is enhanced, transporting moisture to central and east Brazil and enhancing convection in those areas and suppressing convection over the Bolivian Altiplano and the northern part of the continent.

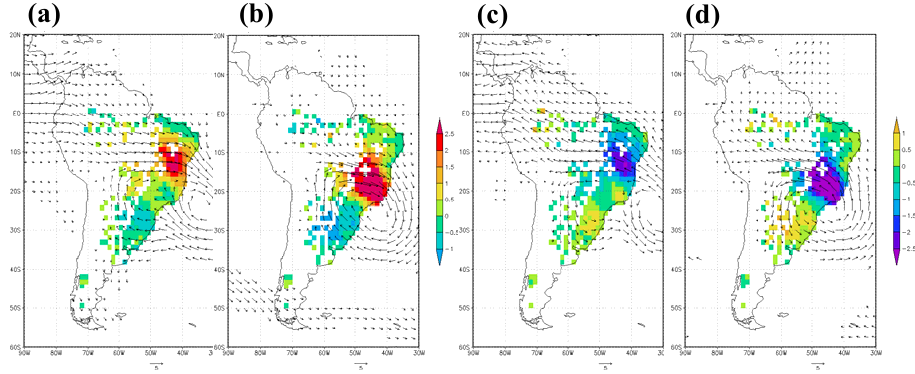


Figure 1.4: Composite of rainfall anomalies and integrated moisture flux for the Wet phase of REOF 1 (a) and REOF 2 (b) and Dry phase (c and d respectively) for filtered 30/70 band data. From Grimm et al. (2005).

Easterly or break periods show opposite patterns of wind and precipitation. The median duration of these events is 4-5 days.

The Madden-Julian Oscillation seems to be the best understood source of intraseasonal variability in the SAMS region. Jones et al. (2004) proved that the MJO represents a robust source of predictability for the eastern region of South America, where active periods are linked to statistically significant increases in extreme rainfall events. The authors concluded that the number of correct forecasts of extreme events during active MJO period doubled that of correct forecasts during inactive MJO periods for the region.

The intraseasonal variability of the SAMS linked to the MJO can be forced by two mechanisms as proposed by Grimm and Ambrizzi (2009) using teleconnection arguments. They attribute the first mode of variability shown in Figure 1.4a to a tropical-tropical interaction on the argument that, as Figure 1.4a shows, the wind field corresponding to this mode has more connection to the tropics than the extratropics. This interaction is produced when the ascending branch of the walker circulation linked to the MJO is over New Guinea and the descending branch over northern South America, and so, enhanced convection over New Guinea will be linked to suppressed convection over central-eastern Brazil. The second mode is attributed to a tropical-extratropical teleconnection pattern again arguing that the wind fields in linked to the second REOF presented in Figure 1.4b have a strong extrat-

ropical component. When anomalous MJO convection reaches the SPCZ, enhancing it and displacing it eastward, this enhanced convection produces a wave train that can stimulate the SACZ by enhancing the cyclonic anomaly to the southwest of the SACZ. Similar modes in the variability of the SACZ have also been identified by Castro Cunningham and De Albuquerque Cavalcanti (2006) as a tropical mode associated with the MJO that displaces the SACZ northward and features a see saw pattern of precipitation between Indonesia and the northern part of the SACZ and a tropical-extratropical mode associated with the PSA pattern that displaces the SACZ southward. Carvalho et al. (2004) linked the decaying phase of the MJO to an increase in the extreme rainfall events over the SACZ and Liebmann et al. (2004) proposed that the MJO influence on the phase of synoptic disturbances played a role in the modulation of the SACZ.

Variability on shorter times scales has also been identified in this region.

1.3.2 Interannual Variability.

As seen from the standard deviation of seasonal mean precipitation shown in figure 1.2, South American precipitation shows strong interannual variability over the SESA for all seasons. During SON we observe the development of precipitation variability over the SACZ. During, DJF, the variability centres over the SACZ and SESA greatly intensify as well as precipitation variability over the Nordeste region and Amazon River Basin. Finally during the MAM season, precipitation variability over the SESA region remains strong while variability over the SACZ and Amazon river Basin is greatly reduced, leaving strong variability only over the Nordeste region and easternmost parts of the Amazon River Basin.

Most of the interannual variability of South American precipitation can be attributed to ENSO with modes linked to ENSO clearly dominating the variability over the region for the JJA, SON and MAM seasons. During DJF on the other hand, only a modest fraction of precipitation variability can be attributed to ENSO ranging from 10 to 27% of the observed variance for previous studies using EOF analysis of precipitation over the region (Zhou and Lau (2001), Paegle and Mo (2002) and Grimm (2011)). Direct ENSO

influence over the region is characterized by suppressed convection over the northern parts of the continent and enhanced precipitation over SESA for the warm phase of ENSO (with the opposite anomalies during the cold ENSO phase). The remote influence of ENSO over South American precipitation is achieved by a combination of mechanisms. The anomalous tropical circulation patterns associated with the Walker and Hadley circulations during El Niño events produce anomalous subsidence over the northern part of the South American continent and anomalous ascent over the subtropical parts of southern South America, this mechanism being dominant over the tropical parts of the continent. In addition to direct circulation anomalies, anomalous Rossby wave activity in the form of the Pacific South America teleconnection patterns produce cyclonic or anticyclonic circulation anomalies over SESA during the negative and positive phases of ENSO. These circulation anomalies greatly determine precipitation anomalies over SESA making this mechanism dominant in this region (Souza et al. (2004), Vera et al. (2004), Grimm and Ambrizzi (2009)).

In spite of this general understanding of main mode of interannual variability over South America, some questions remain about the main mode of variability during peak monsoon season as well as to the evolution of the precipitation variability within the monsoon season (roughly October to May as discussed in section ??).

The first of these issues is what drives the main mode of variability during the peak monsoon season (DJF). Zhou and Lau (2001) and Paegle and Mo (2002) determined, using EOF of filtered monthly CMAP data (81-93) and Rotated EOFs of unfiltered DJF mean merged satellite derived and rain gauge data (1948-2000) respectively, that the main mode of DJF variability was ENSO related, with somewhat dissimilar spatial patterns over the equatorial and northern parts of the continent but agreeing on the sign and spatial distribution of precipitation anomalies over SESA. Grimm and Zilli (2009) on the other hand find quite different results using EOFs of rain gauge data collected from the local weather agencies (1960-2000). The authors find that the major mode of variability during DJF is not ENSO related, and in fact has little SST signature associated with it with the exception of SST over the subtropical Atlantic off the Brazilian coast. This mode is characterized by a

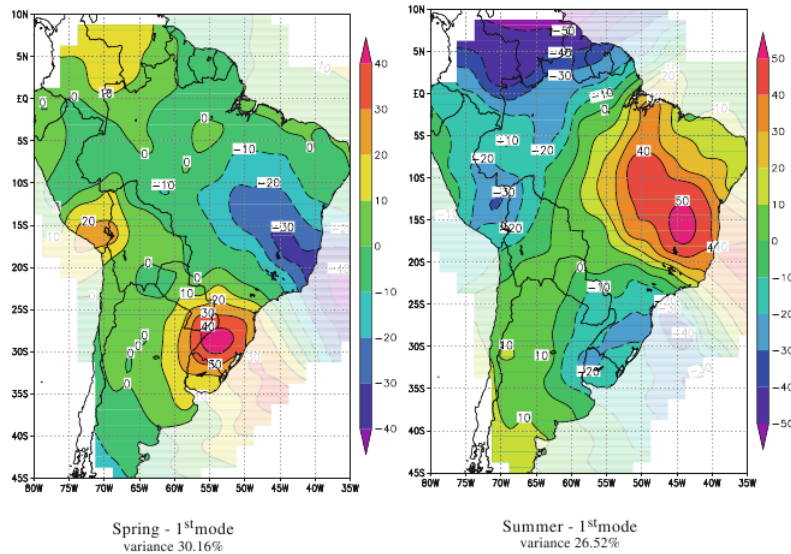


Figure 1.5: First EOFs for spring and summer. Reproduced from Grimm (2011).

strong dipole of precipitation anomalies between SESA and central eastern Brazil and only appears in the results published by Paegle and Mo (2002) as the fourth mode of variability, not being present in the results presented by Zhou and Lau (2001).

The seasonal evolution of precipitation within the monsoon season has been a topic of study only recently. Grimm (2003) found that over central eastern South America, dry anomalies during November tend to be followed by wet anomalies during January for El Niño years, this relationship also existing for La Niña years (Grimm (2004)) and for non ENSO years (Grimm et al. (2007a)). This type of reversal of anomalies is also observed in the EOFs of SON and DJF (Grimm and Zilli (2009), Grimm (2011)). The first modes of SON and DJF as presented in Grimm and Zilli (2009) are reproduced in figure 1.5. The first SON EOF mode (associated with ENSO) is found to be significantly negatively correlated to the first DJF EOF mode (Not associated with ENSO). It is apparent from the relationship between these two EOF modes that the precipitation dipole observed during SON reverses during DJF.

Grimm et al. (2007a) propose a possible mechanism behind this seasonal reversal as follows; El Niño SST anomalies via tropical-extratropical teleconnection to South America

prescribe anticyclonic anomalies over SESA that enhance precipitation over this region and suppress precipitation over central eastern Brazil (as shown in figure 1.5). These spring dry conditions over central-east Brazil lead to reduced soil moisture and enhanced surface temperature anomalies in the region as well as increased net solar radiation and positive SSTAs off Southeaster Brazil. These conditions lead to lower surface pressure, enhanced convergence and convection over the mountainous terrain of south-east Brazil which in turn leads to cyclonic circulations anomalies over the region. These cyclonic anomalies enhance moisture convergence into eastern Brazil and thus promote peak summer wet conditions over central-eastern Brazil. During SON, the teleconnection influence of ENSO over the region dominates, since this is the most favourable season for this type of teleconnection (Grimm (2003), Cazes-Boezio et al. (2003)), while during DJF, this teleconnection is less dominant allowing for local surface-atmosphere processes to take over.

The influence of ENSO variability is most pronounced in alterations in the frequency of extreme events than on total seasonal precipitation amounts, and the most pronounced effect is during the rainy season (Grimm and Tedeschi, 2009). During an El Niño event, an area of reduced frequency in extreme rainfall appears in northwestern South America in August(0) and expands south eastward reaching the SACZ by November(0), meanwhile, south east South America experiences an increase in heavy rainfall frequency. By January(+) during the peak of the monsoon season, this tendency reverses over the SACZ and the extreme rainfall frequency forms a tripole pattern, with enhanced frequency in the southernmost part of south east South America and the SACZ and reduced frequency over the north of the south east South America region. The variability patterns of extreme events during El Niño and La Niña are nearly symmetrical, but present some examples of non linearity in the response to ENSO (Pscheidt and Grimm, 2009).

The impact of ENSO on the SAMS is also present as a modulation of the intensity of the SALLJ and its southerly moisture transport (enhanced during El Niño). This effect has been observed for the three strongest El Niño events between 1980 and 2000 (Berbery and Barros, 2002) and in modelling studies (Misra, 2005). Other studies, found that the SALLJ

was more intense and transported more moisture during JFM of the El Niño 1998 than during La Niña 1999. This intensification of the southerly moisture transport during El Niño is a likely cause of the observed rise in frequency of extreme events discussed previously. The enhancement of the SALLJ is due to an increase in the easterly trade winds in the tropics during El Niño that are channelled along the eastern part of the Andes to form the SALLJ.

Upper level circulation variability over South America is in part dominated by a continental scale vortex which appears as either the first or second EOF mode of upper level wind anomalies over the region and which is significantly correlated to bimonthly precipitation anomalies during all seasons except winter (Zamboni et al. (2009)). This upper level vortex is of quasi-barotropic structure during all seasons. Moisture transport from the SALLJ is modified by the upper level vortex creating precipitation anomalies of opposite sign over SESA and the SACZ during October-November (spring) and January-February (summer) (Robertson and Mechoso (2000), Zamboni et al. (2009)). Zamboni et al. (2011) investigate the relationship between this continental scale vortex and the Pacific South America 1 pattern which is the leading mode of interannual variability over the Southern Hemisphere. During spring the authors find that the upper level vortex over South America is primarily associated with the PSA1 pattern but can also arise from internal variability, greatly reducing the predictability of this circulation center compared to that of the PSA1 pattern. During summer, on the other hand, it is found that the upper level vortex over South America is not linked to the PSA1 pattern and in fact, the PSA1 pattern was barely present during this season. This leads the authors to conclude that the this upper level vortex may be a product of internal variability and a product of local features of the South American continent such as orography and possibly, specially during the summer, strongly related to the South American Monsoon as proposed by Grimm (2003) and Grimm et al. (2007a).

Studies linking South American precipitation to Atlantic SSTs are less numerous and univoque relationships are hard to establish. In general, enhanced precipitation in the SACZ is related to colder SSTs in the subtropical south western Atlantic near the SACZ, implying

atmospheric control over the SSTs in this region. The upper level circulation anomalies that modulate the intensity of the SACZ discussed in the previous section have been shown to be accompanied, on the interannual time scale, by significant SST anomalies that form a zonally elongated north-south dipole pattern centred at about 40S over the Atlantic (Robertson and Mechoso (2000)) with negative anomalies to the north underlying the SACZ and positive anomalies to the south. Cold SST anomalies underlying an intensified SACZ are consistent with reduced incidence of solar radiation and warm anomalies to the south coincident with decreased westerly winds in the region are consistent with reduced evaporation in the area, both imply atmospheric control of this SST dipole. Doyle and Barros (2002) showed that a northward displaced and intensified SACZ is coincident with strong cold SST anomalies off the Brazilian coast between 15S and 35S and extend from Brazil east reaching the Greenwich meridian , conversely a weakened southward displaced SACZ is coincident with weak warm SSTs in the same region (these phases are not exactly antisymmetric). The authors argue that these cold SSTs off the coast of Brazil promote anticyclonic flow that blocks moisture transport of the SALLJ towards SESA and is thus redirected towards the SACZ where it converges with flow from the subtropical South Atlantic high. This mechanism of SACZ variability is in fact quite different than others proposed.

Grimm (2003) found that January rainfall in east-Central Brazil is positively correlated with previous November SSTs and negatively correlated with January SSTs for the ocean in the region of the SACZ of the south east coast of Brazil. This suggests that warm SSTs in November help trigger the circulation anomalies that enhance rainfall in east-central Brazil in January, enhancing the observed reversal of rainfall anomalies. The important of this two way interaction between SAMS and atlantic SSTs is key to capturing the variability of the SACZ properly as showed by Misra (2008) by contrasting the SAMS response in AGCMs forced by observed SSTs and coupled Ocean-Atmosphere GCMs.

A clear relationship has been shown between Atlantic SSTs and precipitation in North-east Brazil (Nordeste region) where precipitation is modulated by the ITCZ (Uvo et al. 1998, Paegle and Mo 2002, Ronchail et al. 2002) and this relationship is strongest during

March and May when precipitation in this region reaches its peak. Positive precipitation anomalies in this region are correlated with positive SST anomalies south of the Equator that induce a southward displacement of the ITCZ. This mechanism of Atlantic SST influence on monsoon rainfall is most pronounced if the positive SST anomalies south of the Equator, and the rainfall anomalies associated with them, occur early in the season.

The relative effect of Atlantic SST anomalies during the different phases of ENSO has been explored by Pezzi and Cavalcanti (2001-01-08) using AGCM experiments forced by mean El Niño or La Niña conditions over all ocean basins with the exception of the tropical Atlantic where an anomalous cross equatorial dipole of SSTs was set as the boundary condition. They found that during El Niño positive SST anomalies over the northern tropical Atlantic and negative anomalies to the south resulted in dry conditions over the Nordeste region intensifying the effect of El Niño with the opposite SST dipole resulting in wet anomalies over the Nordeste, reversing the effect of El Niño over the region. The effect of Atlantic SST anomalies during El Niño years is confined to the Nordeste region. During La Niña conditions positive anomalies over the northern tropical Atlantic and negative anomalies to the south resulted in below average precipitation over the Nordeste region as during El Niño but when the reverse tropical Atlantic SST pattern was applied (negative to the north and positive to the south), positive precipitation anomalies over the Nordeste were produced as well as negative anomalies over a large portion of the South American continent.

1.3.3 Decadal and Interdecadal variability.

Precipitation and river flow records in South America show modes on interdecadal variability related to non-ENSO SST variability like the PDO, the NAO (Robertson and Mechoso 2000; Zhou and Lau 2001; Paegle and Mo 2002), the AAO (Silvestri and Vera 2003, 2009) and the AMO Chiessi et al. (2009).

The Antarctic Oscillation (AAO) has been shown to have strong impact of SESA rainfall during winter and spring. During the spring season, a positive phase of the AAO is related

to an intensified upper-level anticyclonic anomaly, weak moisture transport and decreased rainfall over SESA. The AAO also shows a strong modulating effect of the impact of ENSO on SESA rainfall during the springtime (Silvestri and Vera, 2003). Recent developments (Silvestri and Vera, 2009) have shown that the influence of the AAO on South America show interdecadal variability, having very different effects in the 60-70s and in the 80-90s. In general, the position of the anticyclonic anomaly induced by the positive phases of the AAO has changed leading to different effects of the AAO on South America Silvestri and Vera (2009).

Chiessi et al. (2009) investigated the impact of the Atlantic Multidecadal Oscillation (AMO) on SAMS rainfall using a ~ 4500 year proxy record of the discharge variability of the La Plata River Basin. Their study used a marine sediment core (taken off the coast of Brazil, north of the mouth of the La Plata River) to measure stable oxygen composition of planktic foraminifera (related to the extent of the river plume) and Ti intensity in bulk sediment (related to the source of terrigenous sediments). An oscillation with period ~ 65 years was found in the records that can be associated with AMO modulation of SAMS rainfall.

The North Atlantic Oscillation influence on SAMS has been characterized in early variability studies by Zhou and Lau (2001) and Paegle and Mo (2002) and in both cases appears linked to the second mode of interannual variability. Zhou and Lau (2001) find anomalous high and low pressure centers resembling the NAO pattern in regression patterns between SLP and their PC2. Paegle and Mo (2002) reveal a more complex relationship, finding that the strongest correlation between their PC2 and the NAO is when the later leads by 3 years. They conclude that if SST signals from the Pacific do not interfere, a positive NAO phase enhances rainfall over the northeast corner of Brazil. River flow studies on the Parana and Paraguay rivers show a 8-9 year variability component apparently related to the NAO (Robertson and Mechoso, 1998) implying that the NAO influence reaches farther south than previously suggested. Finally, Marengo et al. (2004) showed positive trends in the SALLJ activity coinciding with trends in the NAO and the PDO.

The Pacific Decadal Oscillation is often described in literature as ENSO-like due to the resemblance of its spatial patterns of climate variability with those of ENSO. Figure ?? from Garreaud et al. (2009) shows South American mean annual precipitation and temperature regressed upon the Multivariate ENSO Index (MEI), the PDO Index and the Antarctic Oscillation Index (AAOI). The PDO related anomalies over South America are also ENSO-like with suppressed rainfall in the northern part of the continent and enhanced rainfall in SESA. Silva et al. (2011) studied the effect of the PDO phase on the impact of El Niño over South America and found that the PDO has a modulating effect on the intensity of the variability patterns produced by El Niño without much change to the spatial distribution of the anomalies.

Several studies have documented increases in precipitation and streamflow over southeastern South America (Robertson and Mechoso 2000, Garcia and Vargas 1998) along with a decrease of precipitation over northern Amazonia (Marengo et al., 2004) since the mid 70s relative to the previous two decades. Garcia and Kayano (2008) found that the Hadley and monsoon circulations had slight differences between the 1958–1976 and 1977–1995 periods as observed in 200hPa potential velocity analyses. They also observe a Walker circulation with weaker action centers during the second period with its western Pacific center located further west than its climatological position. They attribute these changes to PDO influences.

Carvalho et al. (2011) studied the effects of the climate transition in the 1970s on the South American monsoon using NCEP/NCAR reanalysis data. They showed that monsoon onset becomes steadily earlier from 1940 to the early 1970s and has remained earlier than October 23-27 since and that monsoon demise has remained later than April 21-25 since mid to late 1970s. They find a statistical changepoint in SAMS duration in summer 1972 with monsoon duration changing from ~ 170 to ~ 192 days. They also found significant changes in circulation and moisture transport in the SAMS system after this climate transition. This change in climatology is also detected in rainfall records by Marengo 2004 and Satyamurty et al. 2010.

1.4 Modeling, prediction and predictability of SAMS.

The most prominent features of the South American Monsoon System are well captured by AGCMs (Marengo et al., 2010) and regional simulations (Vera et al., 2006), including the Bolivian High and Atlantic trough system, the SACZ, the sub-tropical Atlantic high and the ITCZ, all with their observed position and magnitude. Some shortcomings are found as precipitation over the Amazon region tends to be underestimated (Vera and Silvestri, 2009) and overestimated in the northern part of the SACZ. According to Marengo et al. (2010), SAMS onset and demise as identified in observations are well reproduced in climate simulations with the CPTEC/COLA AGCM when using criteria based on atmospheric humidity flux as defined by Raia and Cavalcanti (2008), the model exhibiting the main features associated with the SAMS life cycle. Silvestri et al. (2009) generated a high-resolution hindcast using the MPI regional model and dynamically downscaled ECMWF-ERA40 reanalysis data and found good agreement between model output and observations of low level monsoon circulation, upper level circulation, surface temperature and SLP. The model showed good skill representing the general features and mean seasonal cycle of precipitation but showed systematic overestimation over both tropical and subtropical regions, still outperforming the global reanalysis specially in the region between 25 and 40 south.

Study of intraseasonal oscillations in 5-year results of 50-day mid range forecasts by a coupled ocean-atmosphere model show more skill over the SACZ during periods of strong MJO activity than periods of weak activity (Jones and Schemm, 2000). On the other hand, forecast skill was low for this region when convection was associated with the 10-30 day variability mode. This result shows that considering the intraseasonal variability increases extended range predictability in the SAMS region. Regional climate simulations over South America using the MM5 model performed by Solman and Pessacg (2011) for different cumulus and planetary boundary layer schemes were able to capture the SACZ-SESA variability see-saw patterns but with underestimated precipitation, particularly over SESA, due to misrepresented moisture convergence. They show that grid nudging of winds

over above the planetary boundary layer improves the performance of experiments. They conclude that no single sensitivity experiment outperforms others over all of South America and that the ensemble of model runs does a better job than any individual experiment.

Misra (2005) showed a diurnal rectification of the intraseasonal variability of OLR anomalies over the SAMS region and attributed this to the coarse horizontal resolution of the model (COLA AGCM). Simulations on the seasonal mean variance of the intraseasonal anomalies of OLR improved significantly when a Regional Spectral Model (RSM) was used with NCEP-NCAR data downscaled by about a factor of 2.5. Using anomaly nesting simulations, which replace the climatology COLA AGCM of the nested variables at the lateral boundaries of the RSM with NCEP-NCAR reanalysis climatology, the simulation of the intraseasonal variance of OLR improves significantly. This implies that systematic errors in the COLA AGCM climatology imposed on the RSM prevent the proper generation on intraseasonal variability. The CPTEC/COLA AGCM has reproduced the observed intraseasonal variability of the SACZ over the South American summer season, including the north-south OLR pattern but not the westward propagation of the OLR anomalies related to the MJO (Marengo et al. 2010, Rodriguez and Cavalcanti 2006).

On an interannual time scale, the variability shows good predictability in most models for eastern Amazonia, the northern part of South America and the northeast region of Brazil showing high positive anomaly correlations and convergence among ensemble members. This is probably due to ENSOs direct influence on these regions. Model skills tend to be very low for the central and south eastern parts of the monsoon region where ensemble members show large dispersion. Cavalcanti et al. (2002) show for several two tier AGCM experiments negative correlations between observed and modelled summer rainfall over the SACZ region at interannual timescales.

Chaves and Nobre (2004) stated the importance of ocean-atmosphere feedbacks and the predominance of SST-cloud-solar radiation feedbacks over the southwest tropical Atlantic as modulators of the intensity and position of the SACZ. They found that warm SSTs over the south tropical Atlantic tend to intensify and shift northward the SACZ while cold

SSTs in that area tend to weaken the SACZ. OGCM performed by the authors showed that the intensification of the SACZ contributes to cool the underlying ocean reversing the pre existing SST anomalies and that this effect on underlying SSTs is about one order of magnitude larger than the dynamic feedback associated with Ekman pumping. These results suggest that the negative SST anomalies observed below the SACZ are a response to atmospheric forcing. On decadal time scales, Barreiro et al. (2002) show, using the NCAR CCM3 model forced with observed SSTs that the precipitation field over eastern South America and the SACZ shows a strong response to local anomalous SSTs over the Atlantic ocean. The first EOF of SST anomalies over the Atlantic which is characterized by a dipole of SST anomalies centred around 25S (positive SST anomalies to the north and negative to the south) is seen to create a dipole like precipitation pattern close to the coast, shifting the SACZ northeast and generating anomalous cyclonic circulation over the region. The response of precipitation to this SST pattern is limited to the coastal regions and has little impact over land.

In general a proper representation of ocean-atmosphere interactions is crucial to capturing appropriately not only the SACZ variability and dynamics, but also the SAMS ENSO teleconnection, as demonstrated by Misra (2008), who attributed the improvement with respect to ENSO to the importance of ocean-atmosphere coupling in modulating the large-scale east-west circulation associated with ENSO.

Studies using the ICTP RegCM3 regional model performed by Grimm et al. (2007b) show that the first modes of spring and summer variability are dipolike as in observations but that the northern part of the dipole pattern is displaced too far north. The reversal between spring and summer variability modes is not reproduced in these model experiments, probably due to the inability of the model to properly capture the surface atmosphere interactions and topographical features that contribute to this local process. This also translates into very low predictability of the monsoon rainfall anomalies during the austral summer in east-central Brazil (Grimm et al., 2007a).

IPCC global coupled model simulations of the South American Monsoon system show

good representation of the spatial and temporal variability of the annual cycle over central and eastern Brazil, with realistic phase of the dry and wet season, onset dates and duration of the rainy season. It was also found that most IPCC models misrepresent the ITCZ over the Atlantic and hence do not capture well the total monsoonal rainfall over the Amazon and Nordeste region.

1.5 Scientific questions addressed in this study.

This work will concentrate on precipitation variability over South America on the interannual and longer time scales giving special focus to the seasonal evolution of the modes of precipitation variability over the region. Relevant questions will be formulated to improve our understanding of precipitation variability over the South American continent.

First among these questions is: is the DJF mode of variability reported by Grimm and Zilli (2009) a robust feature across datasets. Thoroughly understanding which are the main modes of summer precipitation over South America as well as their mechanisms is of crucial importance in the estimation of precipitation predictability over the region as well as the possible implications of climate change over the region.

The second, and most important focus of work is to consider whether the link between the SON EOF1 (ENSO mode) and the DJF EOF1 (Non-ENSO mode) reported by Grimm and Zilli (2009) present in other available data sets such as NOAA's Precipitation Reconstruction Over Land (PREC/L), CMAP and GPCP. If so, does this link withstand more rigorous statistical testing that accounts for the sample size reduction due to non 0 lagged autocorrelation in the PC time series of the EOF modes? If the answer to the previous question is yes then; what additional information can Seasonal Reliant EOF (S-EOF) analysis give us about the seasonal evolution of the modes of variability of the South American Monsoon? On the other hand if the answer to question 2 is no; what new information about the seasonal evolution of SAM variability can S-EOF analysis give us, specially in terms of a clear understanding of the seasonal evolution of precipitation variability over the region and possible clues as to the origin of the strong Non-ENSO DJF mode.

And finally; How well is the seasonal evolution of variability captured in CGCM simulations? and specially, does the Multi Model Ensemble of these CGCMs capture the non-ENSO mode of DJF variability reported by Grimm and Zilli (2009)? Other issues like; What is the predictability of the South American Monsoon? Can CGCMs capture the temporal variation of precipitation over Eastern Brazil, where large variance is observed? Can we develop a circulation based index highly correlated to the EBPI index that CGCMs can capture more appropriately so that using this index we may improve the predictability of the South American Monsoon?

To answer these questions, this work will be structured as follows; Section 2 will review the data and methodology used in this work. Section 3 will encompass EOF analysis of PREC/L, GPCP and CMAP precipitation data and the application of S-EOF analysis to RPEC/L and GPCP data. Section 4 will propose two different approaches to the study of South American precipitation and it's seasonal evolution via a simple precipitation index for Eastern Brazil as well as S-EOF analysis of bimonthly seasons. Chapter 5 will describe the performance of Ocean-Atmosphere Coupled Models participating in the DEMETER project in reproducing the seasonal evolution of the main modes of variability of South American precipitation. Finally, Chapter 6 will summarize the findings of this work and present further questions for study.

CHAPTER 2

MATERIALS AND METHODS

2.1 Datasets

Our main area of focus will be the South American Continent in the area defined by 15N-55S and 85W-30W. Because we wish to focus on the interannual and long term variability of South American Rainfall as well as the seasonal evolution of the variability, the majority of the analysis presented in this work where carried out using the Precipitation Reconstruction over Land (PREC/L) dataset Chen et al. (2002). Prec/L data spans from 1948 to present day of monthly average precipitation totals in units of mm/day. This data is provided by the NOAA/OAR/ESRL PSD, Boulder, Colorado, USA, from their Web site at <http://www.esrl.noaa.gov/psd/>. This dataset consists of precipitation observatiopns over land from more than 1700 stations with ten years or more of reporst collected in the Global Historical Climatology Network (GHCN) and the Climate Anomaly Monitoring System (CAMS) and are interpolated to a 2.5x2.5 degree grid using an Optimal Interpolation (OI) algorithm. For the South American continent, the PREC/L dataset shows good station coverage (5 or more gauge stations per 2.5 degree box) over Pacific coastal and Andean regions from Colombia to Bolivia and over Eastern Brazil with more sparsely distributed rainfall gauges over the Amazonian.

The Global Precipitation Climatology Project (GPCP, Adler et al. (2003)) and the Climate Prediction Center (CPC) Merged Analysis of Precipitation (CMAP, Xie and Arkin (1997)) datasets where also used in this study specially for intercomparison and to give more complete picture of how the observed modes of variability behave over the oceans adjacent to the South American Continent. Both CMAP and GPCP are merged precipitation datasets that include rainfall rain gauge measurements as well as satellite derived precipitation estimates with some differences in the input data used as well as the merging methodology. Although both datasets capture the known major global precipitation pat-

terns some differences in magnitudes arise specially over the oceans where CMAP tends to overestimate rainfall over the tropical oceans (Yin et al. (2004)). The differences in the leading DJF EOF modes of precipitation over South America present in CMAP and GPCP data were touched upon by Negron Juarez et al. (2009) and will be discussed further in this study. For SST data we used the Extended Reconstruction Seas Surface Temperature Version 2 (ERSST.v2) dataset Smith and Reynolds (2004) and for winds and other atmospheric variables the NCEP/NCAP reanalysis Kalnay et al. (1996) all provided by the NOAA/OAR/ESRL PSD, Boulder, Colorado, USA, via their Web site at <http://www.esrl.noaa.gov/psd/>.

The Multi Model Ensemble (MME) seasonal forecast data used in this study was compilation of the 5 models participating in the ENSEMBLE-based predictions of climate change and their impactS (ENSEMBLES) project (Weisheimer et al. (2009) and references therein) contributed by the UK Met Office, Meteo France, the European Center for Medium Range Weather Forecast, the Leibniz Institute of Marine Sciences at the University of Kiel and the Euro-Mediterranean Centre for Climate Change, and one model (POAMA) from the Asia-Pacific Economic Cooperation Climate Center/Climate Prediction and its Application to Society (APCC/CliPAS) (Wang et al. (2009), Lee et al. (2010)). These models form a MME of seasonal forecast from 1960 to 2005 providing precipitation, 500mb geopotential heights and 200 and 850 mb level wind data. Model hindcast runs were initialized on February 1, May 1, August 1 and November 1 to generate forecasts corresponding to the MAM, JJA, SON and DJF seasons.

2.2 Methodology

The South American domain defined in this study is delimited by 15N-55S and 85W-30W and rainfall anomaly fields for this region are analysed using EOF and S-EOF analysis. Because we are mostly interested on the southern summer rainfall variability and its evolution from the previous and into the following season, we concentrate our attention on the tree seasons starting during SON of one year and trough to the MAM of the following year.

The S-EOF methodology can be summarized as follows. Instead of isolating the seasonal mean anomalies for a particular season, the seasonal sequence of precipitation anomalies from austral spring of the previous year (SON(0)) to austral fall on the following year (MAM(1)) was taken as one time step for year 0 in the data matrix as shown in 2.1.

$$\text{data} = D = \overbrace{\begin{pmatrix} \text{SON}(t_1) & \text{DJF}(t_1) & \text{MAM}(t_1) \\ \text{SON}(t_2) & \text{DJF}(t_2) & \text{MAM}(t_2) \\ \dots & \dots & \dots \\ \text{SON}(t_N) & \text{DJF}(t_N) & \text{MAM}(t_N) \end{pmatrix}}^{\text{lat}*\text{lon}*\text{season}} \quad (2.1)$$

A covariance matrix of this data matrix $C = D^t D$ was constructed and standard EOF decomposition is applied and the resulting Eigenvectors, as exemplified in 2.2, are then separated into three maps representing the spatial pattern of variability for each season for that S-EOF mode. The resulting spatial pattern for each S-EOF will have three sequential spatial patterns representing the seasonal evolution of the precipitation anomalies.

$$\text{EV} = \left(\overbrace{x_1 \dots x_{\text{lat}*\text{lon}}}^{\text{SON}} \overbrace{x_{\text{lat}*\text{lon}+1} \dots x_{2*\text{lat}*\text{lon}}}^{\text{DJF}} \overbrace{x_{2*\text{lat}*\text{lon}+1} \dots x_{3*\text{lat}*\text{lon}}}^{\text{MAM}} \right) \quad (2.2)$$

The tree season sequential pattern has one single PC of yearly values that characterizes the interannual variation of this single S-EOF.

S-EOF has some beneficial characteristics compared to other variations of the EOF methodology such as extended EOF analysis Weare and Nasstrom (1982) and cyclostationary EOFs Kim (2002). S-EOF analysis can isolate the seasonal evolution of a mode of variability with respect to the annual cycle instead of an arbitrary four season sequence started on any season as done in extended EOF analysis, and does not rely on data pre-filtering or a prescribed periodicity of the variability as done for cyclostationary EOFs.

Standard regression and correlation analysis of the PCs of EOF and S-EOF modes of variability are used to determine the relationship between the observed modes of variability and different atmospheric variables such as winds at the 200 and 850mb levels and geopo-

tential heights. Student t test were performed to estimate the statistical significance of all correlations calculated. To account for autocorrelations in the PC and anomaly time series that may reduce the effective number of degrees of freedom in the statistical test, we estimated the effective number of degrees of freedom n as

$$n = \frac{N\Delta t}{\tau} \quad (2.3)$$

where τ is the integral time scale represents the period of time required to gain a new degree of freedom in the estimation of the correlation between two time series and is calculated as

$$\tau = \sum_{i=-\infty}^{\infty} C_{xx}(i\Delta t)C_{yy}(i\Delta t)\Delta t \quad (2.4)$$

C_{xx} and C_{yy} are the discrete autocorrelation coefficients of the $X(t)$ and $Y(t)$ variables in the calculation (Davis (1976), Chen (1982), Cazes-Boezio et al. (2003)).

CHAPTER 3

THE SOUTH AMERICAN MONSOON DOMAIN AND ITS VARIABILITY AS OBSERVED FROM EOF AND S-EOF ANALYSIS.

This chapter will be divided into three sections dedicated to the definition of the South American Monsoon domain in PREC/L data (Section 3.1) and the characterization of variability in this domain via EOF and S-EOF analysis (Sections 3.2 and 3.3 respectively).

Standard EOF analysis of South American monsoon precipitation have already been performed in other studies such as Zhou and Lau (2001), Paegle and Mo (2002) and Grimm and Zilli (2009), but none of these studies have been performed using the PREC/L dataset. For this reason it is necessary to perform these standard analysis to characterize the modes of variability present in this dataset so that appropriately compare our results to those previously mentioned. These EOF analysis will also show that the previously reported relationship between the first EOF mode of SON and the first EOF mode of DJF reported by Grimm (2003), Grimm et al. (2007a) and Grimm and Zilli (2009) is not clearly present in the any of the datasets used in this study opening the possibility for a new interpretation of the main mode of of summer precipitation variability and the mechanisms that drive it.

S-EOF analysis of seasonal precipitation anomalies of the SON-DJF-MAM seasons are presented in section 3.3, and will provide a new and clear understanding of the characteristics of the seasonal evolution of the ENSO influence over the South America region. This analysis will also give us new insight as to the characteristics of the precipitation variability during the SON season that evolve into the strong non ENSO mode observed during the DJF season ans how this mode later evolves during MAM.

3.1 The South American Monsoon Domain in PREC/L precipitation data.

Because EOF analysis are very sensitive the choice of domain used, it is important to have a clear definition what is the domain of the South American Monsoon. Here we will use

the definition of monsoon domain based on precipitation using the Monsoon Precipitation Index (MPI) and Annual range of precipitation between the dry and wet season as proposed by Wang and Ding (2008).

The annual range of precipitation is defined as the accumulated summer precipitation minus the accumulated winter precipitation. For the northern hemisphere the summer season is defined as May, June, July August and September (MJJAS) while the winter season is defined as November, December, January, February and March (NDJFM), these definitions leaving out the months of October and April which are considered transition months. Hence for the Northern Hemisphere the annual range of precipitation is defined as summer MJJAS minus winter NDJFM accumulated rainfall while the opposite is true for the Southern Hemisphere.

The Monsoon Precipitation Index is defined as the ration of annual range of precipitation over the annual mean precipitation at each gridpoint so that

$$MPI = \frac{\text{Annual range of precipitation}}{\text{Annual mean precipitation}} \quad (3.1)$$

Using these definitions Wang and Ding (2008) propose that areas around the globe where the MPI is above 0.5 and the annual range of precipitation is above 300mm be classified as monsoon domains. Figure 3.1 shows the spatial distribution of MPI, as color shading, and the monsoon domains that fit these two criteria, in black contours, for CMAP, PREC-1 and GPCP precipitation data.

The monsoon domains depicted in figure 3.1 for CMAP data correspond very well to those shown by (Wang and Ding, 2008) for the same dataset. Results for PREC-L and GPCP data correspond well with those of CMAP giving us confidence in the robustness of this definition of monsoon domain. Over South America we see that two monsoon domains can be observed, one over the northern part of the continent including Venezuela and Colombia and extending north towards Mexico and one over the southern part of the continent south of the equator that includes the Amazon River basin and extends south towards South East South America and includes, in the case of CMAP and GPCP data

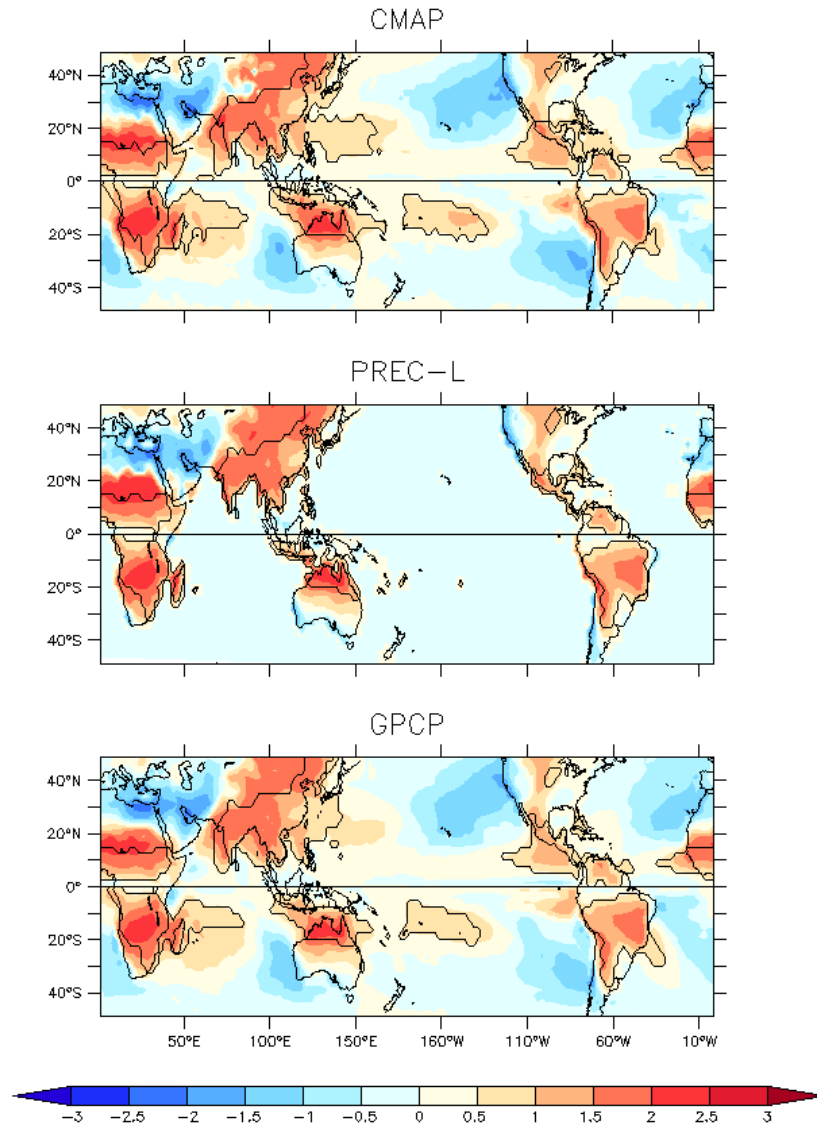


Figure 3.1: Monsoon precipitation index, MPI (color shading) and monsoon precipitation domain (Black contours) in the CMAP, PREC-L and GPCP datasets. The Monsoon domains here shown are defined as areas with MPI greater than 0.5 and annual precipitation range of above 300mm (see text for details).

some part of the oceanic South Atlantic Convergence Zone (SACZ). Because we wish to isolate the modes of variability present in each one of these monsoon domains we define our EOF and S-EOF analysis domain as 85W to 30W and from the equator south to 55S. We extend the domain to 55S to facilitate a more direct comparison of our EOF results with those of Grimm and Zilli (2009) who use a similar domain in their EOF analysis, hoping to minimize the differences in our results that may be attributed to domain selection.

3.2 Results from the standard EOF analysis

This section will discuss, in subsection 3.2.1, the results from our EOF analysis of PREC/L precipitation variability focusing the bulk of our attention on the first three modes of the DJF season and thoroughly comparing them to the results previously reported by Zhou and Lau (2001), Paegle and Mo (2002) and Grimm and Zilli (2009). We will also extend our analysis to the SON and MAM seasons testing the hypothesis of correlation between the dominant EOF SON and DJF modes proposed by Grimm and Zilli (2009).

This section also provides a short comparison between the EOF modes present in the EOF analysis of CMAP, GPCP and PREC/l data, to verify the robustness of EOF results across datasets and to test the reproducibility of the possible relationship between the SON and DJF modes of variability.

3.2.1 Precipitation variability in the PREC/L precipitation dataset for the SON DJF and MAM seasons

The first three SON EOF modes of variability in the PREC/L dataset account for 18%, 13.5% and 8.5% of the total variance observed for the SON season. According to the North et al. (1982) rule of thumb, the first two modes show some degeneracy among each other but are well separated from the third and fourth mode which also show some degeneracy with each other.

The first SON EOF mode (3.2 panel A) shows a strong dipole pattern of variability with negative loading over eastern Brazil and positive loading over SESA with a minor positive

center of variability over the Chilean coast. We will refer to this type of precipitation pattern as a SESA-SACZ dipole pattern. Spatial maps of SSTA correlations for this mode (3.4 panel A) show a clear ENSO pattern over the Pacific Ocean along with positive SSTAs over the Indian Ocean. Over the Atlantic SSTA associated with this mode show an alternating negative positive negative pattern extending south from the equator to about 50S, as well as some positive correlation area off the eastern coast of the USA. This pattern of variability associated is characteristic of the of the ENSO over the South American monsoon region during the SON as revealed (Ropelewski and Halpert (1987) and Aceituno (1989)). Enso influence over the South American continent is mediated by both alterations to the Walker circulation which is of prevalent influence over the northern and equatorial part of the continent (Grimm and Ambrizzi (2009)) as well as via extratropical teleconnection patterns which mediate the influence of ENSO over the extratropical parts of the South American continent and that are strongest during the transition seasons such as SON (Cazes-Boezio et al. (2003)).

The second SON EOF mode of variability is also a dipole type of pattern but with the centres of variability shifted northward with respect to the first SON mode. For the second SON EOF mode, negative anomalies dominate the equatorial region of the continent with largest negative values over the region of the mouth of the Amazon river and positive anomalies directly to the south extending from Eastern Brazil westward over the continent reaching almost the Peruvian coast. We will refer to this type of variability pattern as a meridional dipole pattern. The SST anomalies that accompany this mode of variability (Figure 3.4 panel B) are characterized by pattern reminiscent of ENSO anomalies but with positive anomalies contained to the eastern Pacific. Over the Atlantic Ocean, the second SON EOF mode is accompanied by cold SSTAs over the tropical Atlantic and warm SSTAs over the subtropical South Atlantic in the oceanic portion of the SACZ. This mode possibly represents the weaker effect of ENSO SST anomalies over South America via the modification of the Walker circulation during SON. Anomalous SST anomalies over the eastern Pacific may enhance precipitation in this region leading to enhanced subsidence

over northern South America and reduced precipitation (Grimm and Ambrizzi (2009)). Because both of these modes appear linked to Pacific SSTs, they therefore form a somewhat degenerate EOF pair.

Finally the third SON EOF mode (3.4 panel C) is characterized by negative precipitation anomalies over most of the South American continent, with the exception of small areas of weak positive anomalies over the eastern Brazilian coast and northern Argentina. This mode has almost no SST anomalies associated with it (3.4 panel C).

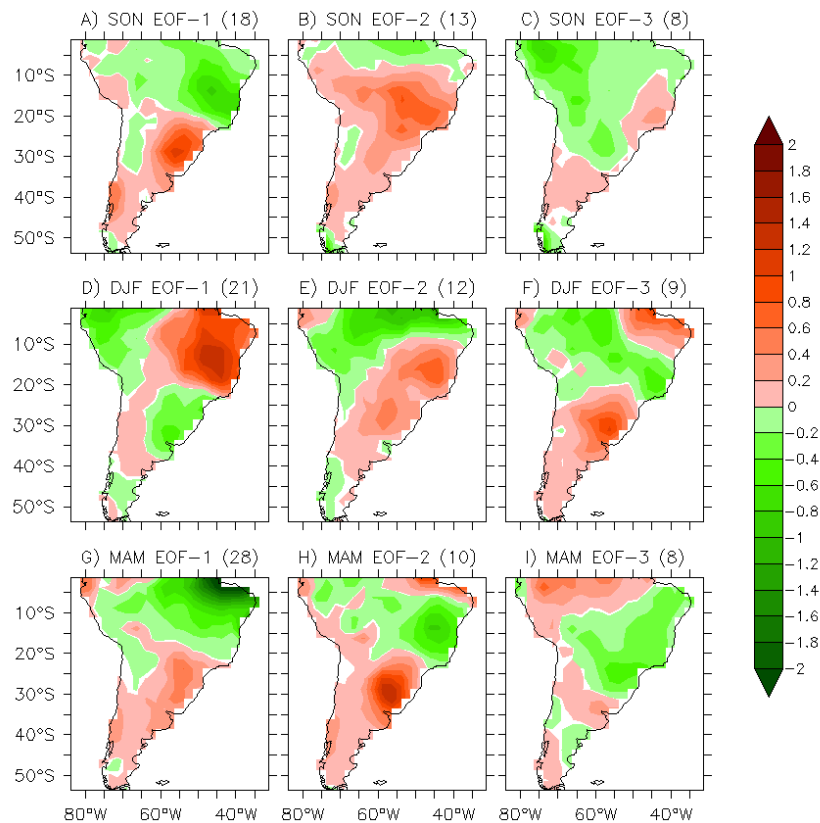


Figure 3.2: Spatial patterns of the first three EOF modes of variability for SON (top three panels), DJF (middle three panels) and MAM (bottom three panels) in the PREC/L dataset. The Eigenvectors here presented have been multiplied by the standard deviation of their corresponding PC time series, so that the shading at each gridpoint represents the amount of loading contributed by that gridpoint to the variance of that mode.

The first three EOF modes of variability present in the PREC/L data set account respectively for 21.4, 11.7 and 8.9 percent of the observed variance in the anomaly field. According to the EOF separation rule of thumb of North et al. (1982), the first mode is well

separated from all the others while the second and third mode show a magnitude of the difference in their eigenvalues comparable to the magnitude of the typical sampling error indicating some possible degeneracy in these two modes. The spatial patterns of the first three DJF EOF modes are shown in the middle panels of 3.2 (panel D, E and F) while figure 3.3 shows the Principal Component time series of the first three EOF modes as well as their power spectra.

The first DJF mode is characterized by strong positive precipitation anomalies over central eastern Brazil and negative anomalies western South America and most of the continent north of the Equator, as well as negative anomalies over South East South America south of the SACZ. We will refer to this type of spatial pattern as a continental tripole pattern. Panel D of 3.4 shows the correlation pattern of the DJF EOF1 to global SST anomalies. The SST anomaly pattern associated with this first DJF EOF mode has little significant signature over the the tropical Pacific showing only significant positive correlations to SSTAs over the southern Pacific between 40 and 60S and South Eastern Indian Ocean. Negative SST anomalies associated with the first DJF EOF mode are observed over the subtropical Atlantic off the coast of South America underlying the SACZ. Similar negative correlation between SACZ precipitation and the SSTA in the underlying Atlantic have been previously observed by (Robertson et al., 2003) and have been proposed to be indicative of atmospheric control over the underlying ocean in this region. The first DJF EOF has significant spectral peaks for 3 and 5 year periodicities as well as a long periodicity peak at about 20 years period. The time series of the first DJF EOF clearly shows the presence of a strong decadal part of this mode to which the higher frequency variability is superimposed. The extreme positive phase of this mode appear to be more frequent than its negative counterpart with predominant positive peaks during the DJF seasons of 1964-65, 1980-81 and 1984-85 while only having one negative peak of comparable magnitude during 1971-72. This mode is equivalent to the first DJF EOF mode reported by Grimm and Zilli (2009) and accounts for a similar fraction of the total observed variance (22% in their case). This mode appears as the fourth mode of variability in Paegle and Mo (2002) rotated EOF

results and is not present in the results of Zhou and Lau (2001).

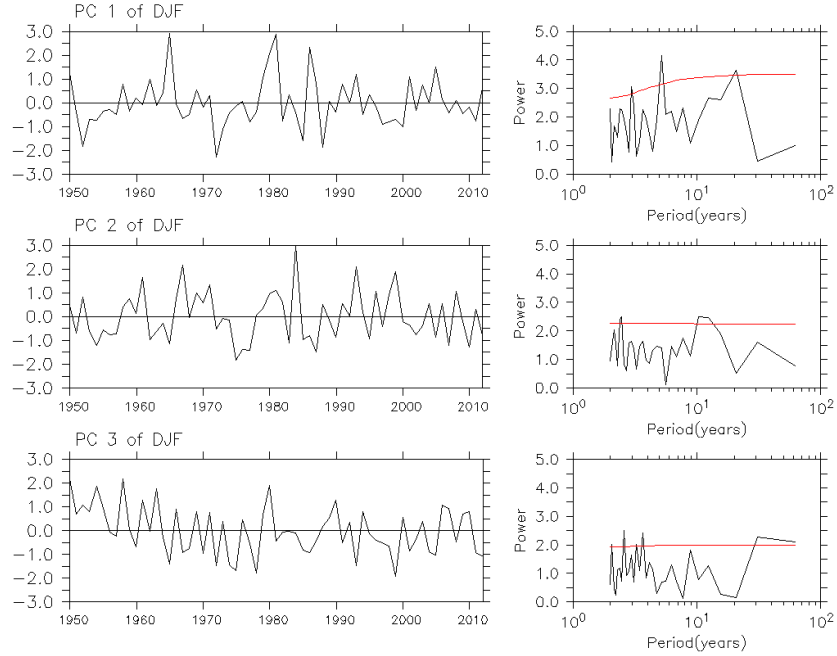


Figure 3.3: PC time series of the first three DJF EOF modes present in PREC-L data along with the power spectrum corresponding to each time series. PC time series presented here have been normalized by their corresponding standard deviation. The red curves in the power spectra represent the spectra of a red noise process fitted to each time series.

The second DJF EOF (3.2 panel E) constitutes a north-south dipole of precipitation anomalies between the Nordeste and Equatorial Amazon region close to the equator and eastern Brazil and the SESA region further south. This structure is similar to the SON meridional dipole mode with northern negative anomalies extending further south than during SON and positive anomalies to the south showing a two maxima structure, a stronger over the southern part of Eastern Central Brazil and a weaker positive maxima to the south over SESA. This mode has a strong ENSO type pattern of SSTA as shown in panel E of 3.4 also showing some significant positive correlation to Indian Ocean SSTs. The second DJF EOF shows a significant peak for 2.5 year periodicity and a broad peak for 10-12 year periodicity and strong time series peaks during 1965-66, 1982-83 and 1997-98 suggesting a strong link of this time series to ENSO (see 3.3). The time series of the DJF EOF2 mode shows strong decadal variability before the early 1990's while for the period from the

1990's to present the decadal part of the variability appears greatly diminished suggesting a change in the ENSO-South American Monsoon relationship around this period. This mode is reported as the first mode of variability in Zhou and Lau (2001) with some minor differences in the spatial pattern of variability associated with the mode, mainly the presence of a single positive center of variability over the southern part of the continent over SEAS. The rotated EOF analysis of Paegle and Mo (2002) capture this mode as the first mode of variability but with the major difference of covering the entire north of the South American continent with negative anomalies missing the positive anomalies over the Ecuadorian coast. This second DJF mode strikingly similar to the second DJF EOF mode reported by Grimm and Zilli (2009) sharing the same two maxima structure for the positive anomalies over the southern part of the continent and accounting for a similar fraction of the observed variability as in the results presented here.

The third EOF DJF modes shows a three band structure with anomaly bands extending in a northwesterly to southeasterly direction over the South American continent with positive anomalies over SESA, negative anomalies over the SACZ and extending inland towards the central Amazonia and positive anomalies over the Nordeste region. This mode has spectral peaks at 2, 2.5 and 3.5 years as well as a broad peak that occupies the 30 years and higher periods of the periodogram. The time series of this mode (3.3) is dominated by what could be a strong negative trend period from the late 1940s to the late 1970s and by a period of very little to no trend afterwards. SST anomaly correlation maps show in 3.4 panel F show significant positive correlations to SSTAs over the tropical Atlantic and eastern tropical and south Pacific as well as widespread positive correlation over the Indian Ocean. This mode has little in common in terms of spatial patterns of the variability with the third mode reported by Zhou and Lau (2001) which for them is also a decadal mode of variability. Paegle and Mo (2002) report a very similar third rotated EOF in terms of spatial pattern, but they discard it because it was only present in their satellite derived dataset and not in their rain gauge dataset. Finally Grimm and Zilli (2009) have a third DJF mode of very similar spatial and associated SST patterns leading us to conclude that

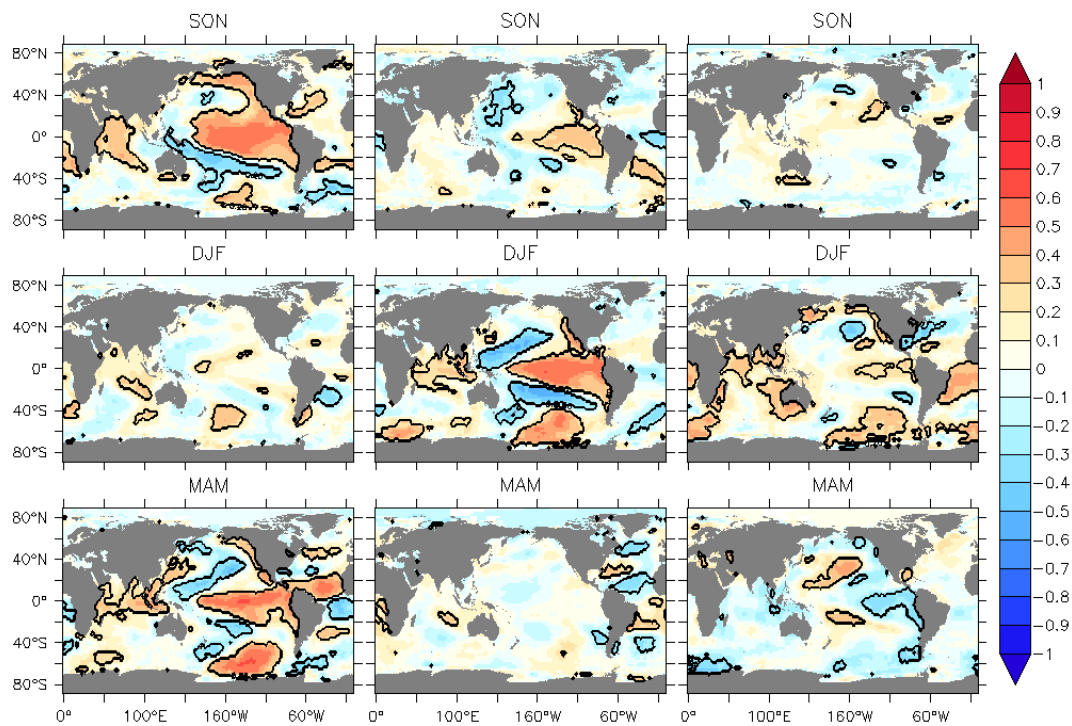


Figure 3.4: Spatial maps of correlation to SST anomalies. Panels A, B and C show the correlations of SON EOF 1, 2 and 3 to contemporary SON SST anomalies. Panels D, E and F, correlations of DJF EOF 1, 2 and 3 to contemporary DJF SSTAs. Panels G, H and I, correlations of MAM EOF 1, 2, and 3 to contemporary MAM SSTAs. Contours represent areas where the correlations are significant at the 90% test level according to a non-naive Student t-test with a modified sample size at each grid-point according to the procedure shown Chapter 2.

these modes are equivalent.

For the MAM season the three leading EOF modes in the PREC/L dataset account for 28%, 10% and 7.8% of the observed variability of the MAM season. The first MAM EOF mode, also a meridional dipole type mode, captures the variability of precipitation over the Nordeste region of Brazil (northeastern states of Brazil such as Pariba, Rio Grande do Norte and Ceara) which is characterized by peaking precipitation during the MAM season (Kousky (1988)). The precipitation in this area is associated with the southward migration of the Atlantic ITZC that reaches its southernmost position during the MAM season lagging a season to the southernmost location of the insolation maxima and following the equatorial SST ridge (Kousky (1988), Sun et al. (2005), Zhou and Lau (2001)). SSTA correlation maps shown in panel G of Figure 3.4 show the relationship of this mode with ENSO SST Anomalies over the Pacific as well as a strong influence of Atlantic SSTs. ENSO type SST anomalies are strongly linked, via anomalous Rossby wave teleconnections which are stronger during MAM than DJF (Cazes-Boezio et al. (2003)), to the precipitation anomalies over SESA (?), and also play a role in the modulation of the intensity of precipitation over the Atlantic ITCZ via walker circulation anomalies. The cross equatorial SSTA gradient observed over the Atlantic Ocean (as opposed to the SST anomalies alone) associated with the first MAM EOF mode plays a key role in determining the meridional displacement of the ITCZ and it's final position during the MAM season (Hastenrath and Heller (1977), Nobre and Shukla (1996)) and thus is likely to be the strongest governing factor of Nordeste rainfall during the MAM season. This first MAM EOF mode is equivalent on terms of spatial pattern and SSTAs associated with it as the first MAM EOF reported by Grimm (2011).

The second MAM EOF mode is a SESA-SACZ dipole type mode with some similarity in terms of spatial pattern with the third DJF EOF mode shown earlier, with similar a banded structure of three alternating positive-negative-positive anomaly bands that tilt from northwest to southeast with the differences being chiefly the intensity of the anomaly centres and their geographical extension with less intense negative anomalies over the central part of the continent and smaller positive anomaly region over the Nordeste region. SST

		DJF		
		EOF 1	EOF 2	EOF 3
SON	EOF 1	0.21*	0.23**	-0.02
	EOF 2	-0.10	0.29***	0.13
	EOF 3	0.06	-0.11	0.27***

		MAM		
		EOF 1	EOF 2	EOF 3
DJF	EOF 1	-0.02	0.30***	0.10
	EOF 2	0.55***	-0.13	-0.19*
	EOF 3	-0.02	-0.31***	-0.24**

Table 3.1: Correlation tables between the first three modes of SON and DJF (top table) and DJF and MAM (bottom table). The correlation values with one, two and three asterisks are significant at the 80, 90 and 95 % test level according to a non-naive student t test with a corrected sample size calculated as shown in chapter 2.

anomaly patterns for this mode (3.4 panel F) show weakened positive SST anomalies south of the equator and stronger negative anomalies to the north of the equator and in the subtropical Atlantic as compared to those related the third DJF EOF mode (3.4 panel H). The third MAM EOF mode shows strong negative precipitation anomalies over most of the South American continent with strong positive anomalies confined the Amazon Basin near the equator and weak positive anomalies over SESA. The SST patterns that accompany this MAM mode show cold anomalies over the eastern Pacific Ocean in a pattern that could indicate the relationship of this mode to developing La Nina conditions.

The strong similarities between our first two SON EOF modes, our first three DJF EOF modes and our first MAM EOF mode for the PREC/L data to those same modes presented by Grimm and Zilli (2009) and Grimm (2011) for EOF analysis carried out on gridded precipitation observations collected from Brazilian and other South American meteorological agencies give us the confidence that we are observing the same modes of variability as reported in those studies and thus we may carry on with the comparison of our results to those published in those studies in a fair manner.

Table 3.1 shows the correlations between the first three SON EOF modes and the first three DJF EOF modes and between the first three DJF EOF modes and the first three MAM

EOF modes calculated from PREC/L data. The statistical significance of the correlations shown in this table is calculated according to a two tailed Student t-test with a sample size adjusted for each pair of time series according to the procedure shown in Chapter 2.

For the SON and DJF seasons we find that in general our correlations between SON and DJF modes are weaker than the correlations reported by Grimm and Zilli (2009). We observe strong, highly significant, correlation between the third mode of SON to the third mode of DJF with these modes not being significantly correlated to any other EOF modes, suggesting a straightforward relationship of seasonal evolution from the third SON EOF mode to the third DJF EOF mode.

We find that the DJF meridional dipole mode (DJF EOF 2), which represents the direct effects of ENSO over South America is significantly correlated to the SON meridional dipole mode (SON EOF 2) (95% level), which has an ENSO-like SST anomaly pattern, and less significantly to the SON SESA-SACZ dipole mode (SON EOF 1), which appears to represent the direct ENSO influence over South America during the SON season. This correlation of the DJF EOF 2 to both the SON EOF 1 and 2 could likely be due to the degeneracy of the SON 1 and SON 2 modes.

The relationship between the SON SESA-SACZ dipole mode (SON EOF 1) and the DJF continental tripole mode (DJF EOF 1), that serves as one of the basis for the hypothesis of local surface-atmosphere processes as drivers of the main mode of variability of DJF proposed by Grimm and Zilli (2009), we find that this correlation though present with a value of 0.21, is only valid at the 80% test level according to our significance testing procedure. We also find that the SON meridional dipole mode (SON EOF 2) has a weak correlation to the DJF continental tripole mode (DJF EOF 1) making it difficult to assess from this analysis if any of the SON EOF modes of variability serve as precursors for the DJF continental tripole mode.

For the MAM season we find strong correlation between the DJF meridional dipole mode (DJF EOF 2), which is the DJF ENSO mode, to the MAM meridional dipole mode (MAM EOF 1) which represents the ENSO influence over South America during MAM as

expected, with the DJF EOF 2 being the only contribution to the MAM EOF 1. The MAM EOF 2 we find to be strongly correlated to the DJF EOF 1 and EOF 3, this relationship most likely due to the somewhat similar SST anomalies that the three modes have over the tropical Atlantic. The third MAM EOF mode, which is accompanied by cold SST anomalies in the tropical eastern Pacific has significant correlations to the third DJF EOF mode (associated with warm SSTs confined to the eastern Pacific) and to a lesser extent to the second DJF EOF mode (ENSO mode). The SST anomaly patterns associated with the third DJF EOF mode and third MAM EOF mode show some similarities over the eastern Pacific with opposite sign.

As we can see from these correlation relationships between EOF modes of SON and DJF and of DJF and MAM, multiple EOF modes are correlated to each other, for example the SON EOF 1 and EOF 2 being significantly correlated to the DJF EOF 2, making the relationships between the modes difficult to interpret and hence making a clear understanding of the seasonal evolution of the modes of variability over the South American continent difficult. It is for this reason that we resort to the use of Seasonal EOF (S-EOF) analysis with the hopes of better separating the interactions between seasonal modes and hopefully give a more clear picture of the seasonal evolution of variability over the region.

3.2.2 Comparison between the variability captured by EOF analysis in PREC/L, CMAP and GPCP precipitation datasets and the importance of the EOF domain used to study the South American Monsoon

In this section we will extend the EOF analysis to GPCP and CMAP data. This is a relevant step because it lets us to check for the robustness of the modes of variability found in the PREC/L data in the previous section but also lets us have a more direct comparison of our results with those found in the conflicting literature such as Zhou and Lau (2001) for CMAP. Here we will only discuss the first two SON modes, the first two DJF modes and the first MAM mode because they are found to be the most relevant for our results.

It is important to note that here we compare the EOF analysis for GPCP and CMAP data for the period spanning 1979-2010 (30 years for each season) with the EOF results for PREC/L data spanning the period 1948-2010 (63 years for each season). This comparison although not direct, may shed some clues as to the change of the behaviour of these modes of variability and most importantly possible changes in the behaviour of the relationship between the modes of different seasons.

Figure 3.5 shows the first two SON EOF modes of GPCP and CMAP data for the period from 1979-2009. The first EOF mode in GPCP and CMAP data account for 23.3% and 19.87% of the observed variability in each dataset respectively. The PCs of first EOF modes of GPCP and CMAP have a correlation value of 0.92 to each other and correlation values of 0.88 and 0.82 to the contemporary years of the PC of SON EOF 1 of PREC/L data discussed in the previous section (all of these values are significant at the 99% test level). The first SON EOF mode of GPCP is well separated from the second EOF mode (which accounts for 11.8% of GPCP variability), while for CMAP it is slightly degenerate with its second mode (11.71% of CMAP variability).

The first SON EOF mode in both datasets captures the precipitation dipole between SESA and the SACZ, and are in good agreement with each other in terms of temporal variation and spatial pattern, with only some differences in magnitude for the anomalies over the western part of the South American continent, over Ecuador and Peru. This mode is also represented by the first EOF mode of PREC/L data (3.2 panel A). In terms of associated SSTAs the differences with our PREC/L results are more noticeable with this mode in these datasets being linked to strong localized central Pacific warming in both datasets instead of the broad SST anomalies linked to the PREC/L SON EOF 1 shown in panel a of figure 3.4. Over the Atlantic this mode is characterized by warm SSTAs over the subtropical South Atlantic south of 20S and cold SSTAs south of 40S in all datasets.

The second SON EOF mode in both datasets captures the same meridional precipitation dipole as the SON EOF 2 of PREC/L (figure 3.2 panel B) and their PC time series show correlation values of 0.86 and 0.57 to the contemporary part of the PC of the second EOF

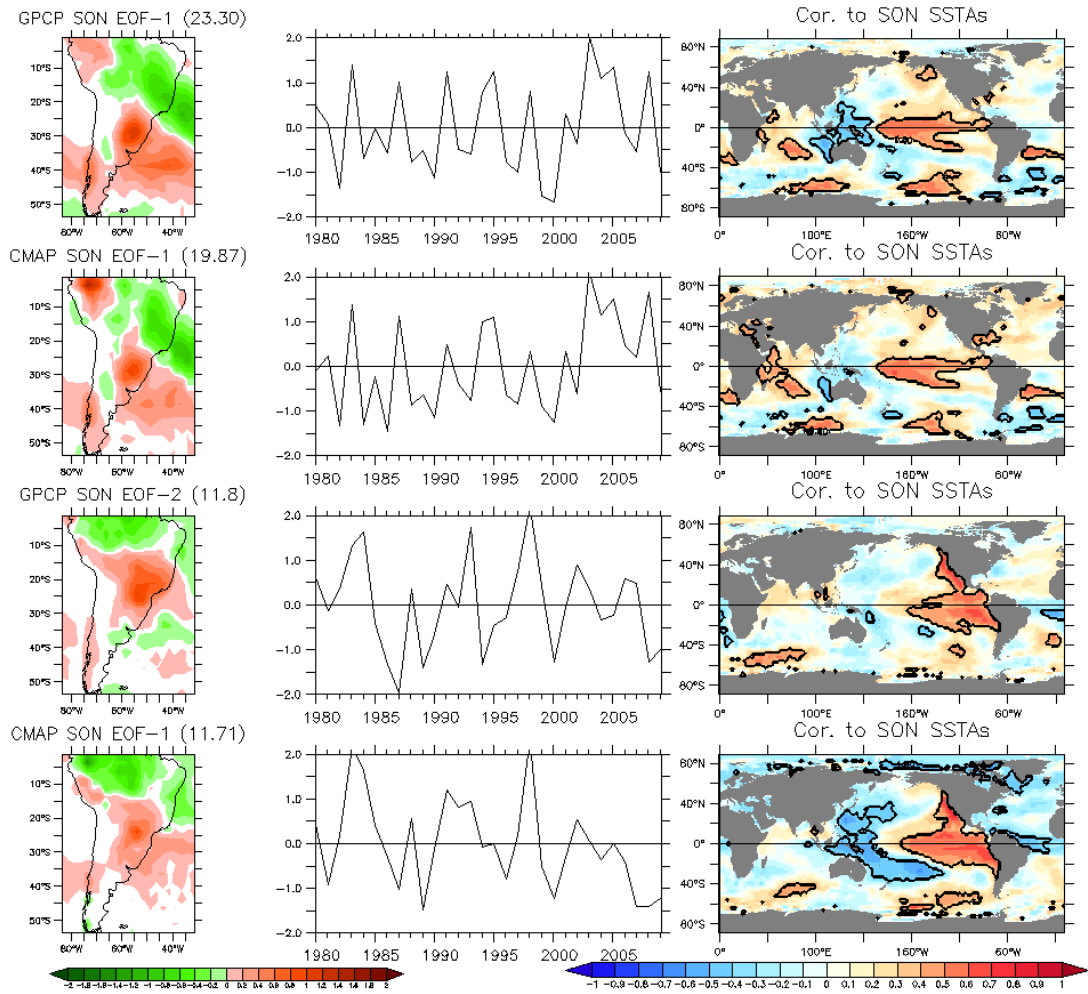


Figure 3.5: Eigenvector maps, principal components and maps of correlation between PCs and SSTAs for the first two SON modes of GPCP and CMAP data. PCs presented here are normalized by their corresponding standard deviation. SST maps show contours of 95% significance level.

mode of PREC/L data. These two GPCP and CMAP EOF 2 modes differ from each other very little in both spatial pattern and temporal variability (correlation to each other is 0.75, significant at the 99% test level). SST patterns accompanying this mode in both datasets shown eastern Pacific warming and western Pacific cooling (much stronger in the SST anomalies associated with the CMAP SON EOF 2) in a more traditional El Niño pattern.

The spatial patterns of the first two SON EOF modes in PREC/L, GPCP and CMAP data are very similar but it seems clear that the relationship between these two SON EOF modes has changed from the 1948-2010 period contained in the PREC/L analysis to the 1979-2010 period of the GPCP and CMAP analysis. In the analysis of the most recent years provided for GPCP and CMAP the first two EOF modes appear as well separated (in GPCP data) or with little degeneracy (in CMAP data) while in PREC/L data, these modes appear as more strongly degenerate, this in spite of a longer time period used which should reduce sampling errors and improve the separation of the modes. The SST patterns associated with the first and second GPCP and CMAP EOFs also differ strongly from the SST anomalies associated with the first two PREC/L EOF modes. While both SON EOF mode 1 and 2 are linked to Pacific SSTs in all datasets, GPCP and CMAP show SST patterns associated with their first two SON EOF modes that clearly identify that different regions of the Pacific Ocean have impact on these modes while in PREC/L data this distinction is much less clear.

Figure 3.6 shows the spatial maps, PC time series and SST correlation maps of the first two DJF EOF modes for GPCP and CMAP. The first DJF EOF modes of GPCP and CMAP capture the same continental tripole pattern as the first PREC/L EOF mode (fig 3.2 panel D). These first EOF modes of GPCP and CMAP account for 22.92% and 22.55% of the explained variance in each dataset respectively. For GPCP the first DJF EOF mode is not well separated from the second DJF EOF mode which accounts for 16.57% of explained variance whereas for CMAP, the first EOF mode (22.55% of variance) is well separated from the second DJF EOF mode (with 12.20% of variance). The first DJF EOF mode in

both GPCP and CMAP shows almost no associated SST anomalies with only some positive anomalies over the southern Pacific ocean, which could be a persistence signal from the SST anomalies seen over the same region for the first SON EOF mode, and local cold anomalies off the coast of Brazil in the region underlying the SACZ.

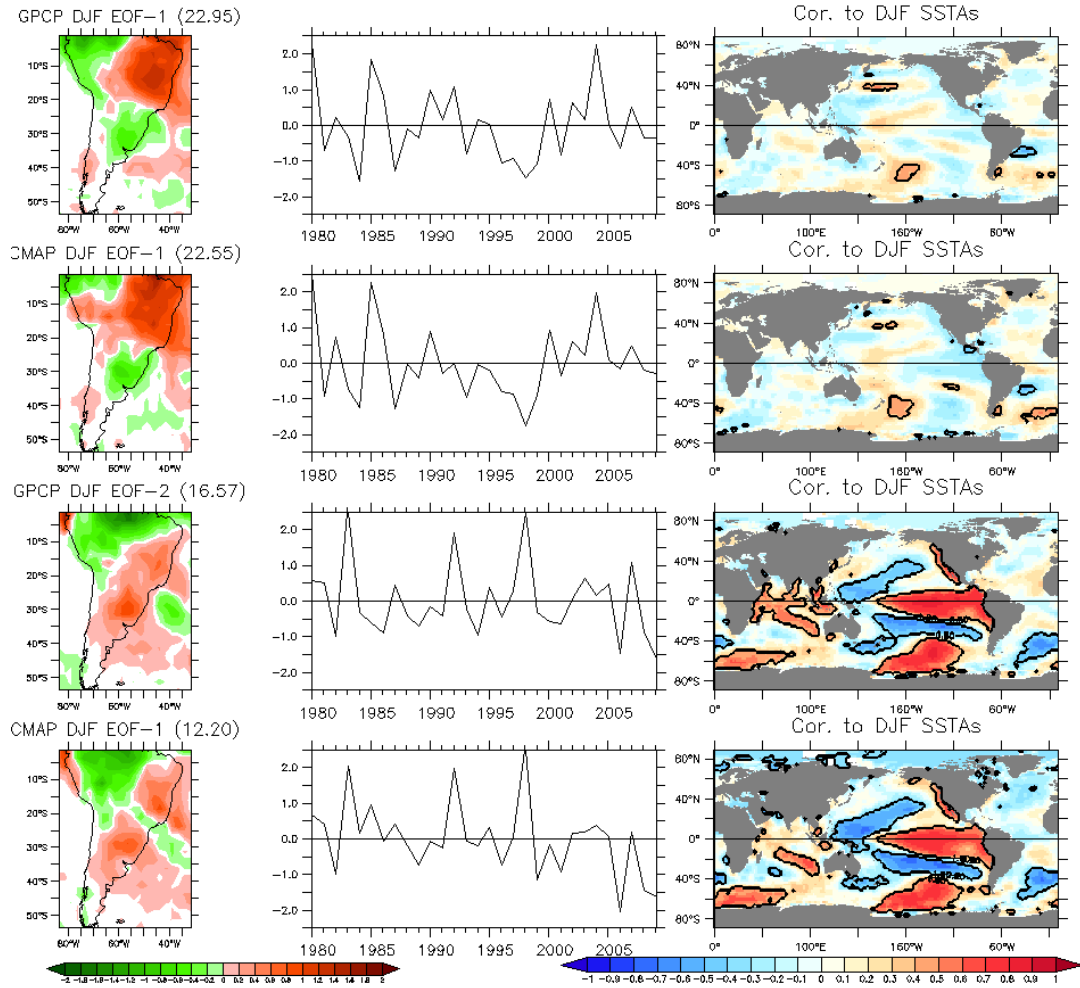


Figure 3.6: Same as in figure 3.5 but for DJF EOF mode 1 and 2.

The second DJF EOF of both datasets shows the strong meridional precipitation dipole pattern that is characteristic of ENSO influence over the region. This is clear from the associated SST anomaly maps as well as clear peaks in the PC time series for 82/83, 91/92 and 97/98. Both datasets show that this mode is accompanied by negative precipitation anomalies over the Atlantic ocean off the coast of Brazil at approximately 30S (present in

both datasets but more intense in GPCP).

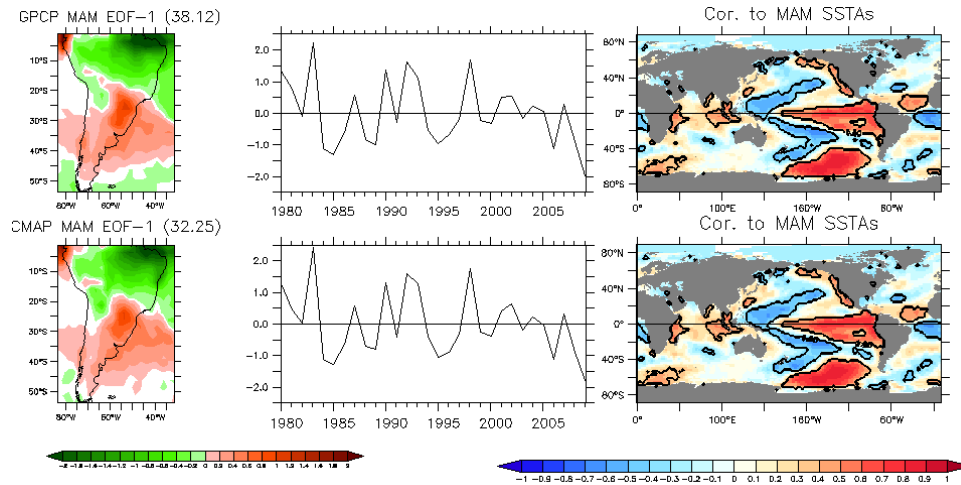


Figure 3.7: Same as in figure 3.5 but for DJF EOF mode 1.

For MAM, figure 3.7 shows the first EOF mode of GPCP and CMAP precipitation which account for 38.12% and 32.25% of the explained variance of their corresponding dataset and their corresponding PC time series show a correlation value of 0.99. This mode is characterized in both datasets by strong meridional dipole with negative precipitation anomalies over the northern part of the continent and positive anomalies over SESA. This EOF mode captures the same spatial pattern of variability, temporal behaviour and pattern of SST anomalies as the first MAM PRE/L EOF mode (the PC time series for this mode in GPCP and CMAP show correlation values of 0.96 and 0.95 to the contemporary part of the MAM EOF 1 PC time series of PREC/L data).

Now that we have seen that the modes of variability captured by EOF analysis in GPCP, CMAP and PREC/L data are in good agreement in all datasets, we will discuss the seasonal evolution of these modes. Table 3.2 shows the correlation tables between the EOF modes here discussed separately for GPCP and CMAP data. From this table the most important result is the fact that for both of the datasets studied in this section, the first DJF EOF which represents the continental tripole of precipitation variability shows no significant correlations to the any EOF modes of the preceding SON season. The correlations between the SON SESA-SACZ dipole mode and DJF continental tripole mode are of 0.07 in GPCP

		GPCP				
		SON EOF 1	SON EOF 2	DJF EOF 1	DJF EOF2	MAM EOF 1
SON EOF 1	1	0.00	0.07	0.38*	0.19	
SON EOF 2		1	0.23	0.46*	0.40*	
DJF EOF 1			1	0.00	0.11	
DJF EOF 2				1	0.77**	
MAM EOF 1					1	

		CMAP				
		SON EOF 1	SON EOF 2	DJF EOF 1	DJF EOF2	MAM EOF 1
SON EOF 1	1	0.00	0.06	0.17	0.12	
SON EOF 2		1	0.17	0.64**	0.49**	
DJF EOF 1			1	0.00	0.05	
DJF EOF 2				1	0.67**	
MAM EOF 1					1	

Table 3.2: Correlation tables between the first two SON EOF modes, the first two DJF EOF modes and the first MAM EOF mode for GPCP (top) and CMAP (bottom) data. The correlation values with one and two asterisks are significant at the 99% test level according to a non-naive student t test with a corrected sample size calculated as shown in chapter 2.

data and 0.06 in CMAP data.

From the correlation values in table 3.2, the only clear evidence about the seasonal evolution of these modes of variability is the clear progression of the influence of ENSO over the region as represented by the seasonal evolution of the meridional dipole mode from SON to DJF and later to MAM, with the SON EOF 2 strongly correlated to the DJF EOF 2 and the DJF EOF 2 strongly correlated to the MAM EOF 1, this progression being specially clear in CMAP results. GPCP results also show a relationship between the SON EOF 1 related to central Pacific warming to the DJF EOF 2 which related to classic ENSO SSTs, this relationship being much weaker in CMAP data.

3.3 Results from the S-EOF analysis

Using Seasonal EOF analysis (S-EOF) we find that the first three S-EOF modes of variability of the SON-DJF-MAM seasonal sequence account for 13.9, 10.4 and 5.6 % of the total

variability observed for the three seasons in the PREC/L dataset. We find the first two S-EOF modes to be degenerate but well separated from the following S-EOF modes. Figure 3.8 shows the sequential three season maps that correspond to the spatial patterns of the first three S-EOF modes.

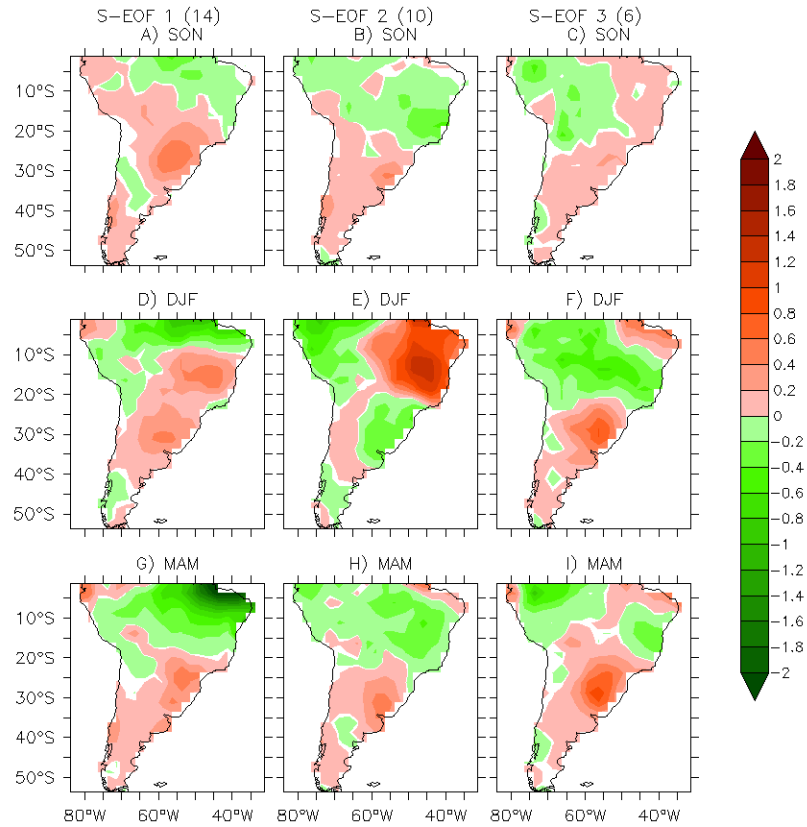


Figure 3.8: Spatial patterns of the first three Seasonal EOF modes of variability in the PREC/L dataset. Each column in this figure represents a single Eigenvector of the S-EOF process which has been remapped into a three season sequence.

The first mode of the Seasonal EOF analysis captures the seasonal evolution of the ENSO induced variability over the South American continent as shown by correlation to SST patterns in figure 3.9 panels A, D and G. The spatial patterns of the S-EOF 1 for the DJF and MAM seasons (figure 3.8 panels D and G) bare close resemblance to the equivalent meridional dipole ENSO modes in DJF (DJF EOF 2 shown in figure 3.2 panel D) and in MAM (MAM EOF 1 shown in figure 3.2 panel G), with small differences in the magnitude of the anomalies specially for the DJF season. For SON, the ENSO mode shows a dipole

of variability with positive anomalies over SESA and negative anomalies to the north over the eastern Amazonia and the mouth of the Amazon river, whereas the SON EOF 1 (SON ENSO mode shown in 3.2 panel A) shows similar positive anomalies but strong negative anomalies over eastern Brazil.

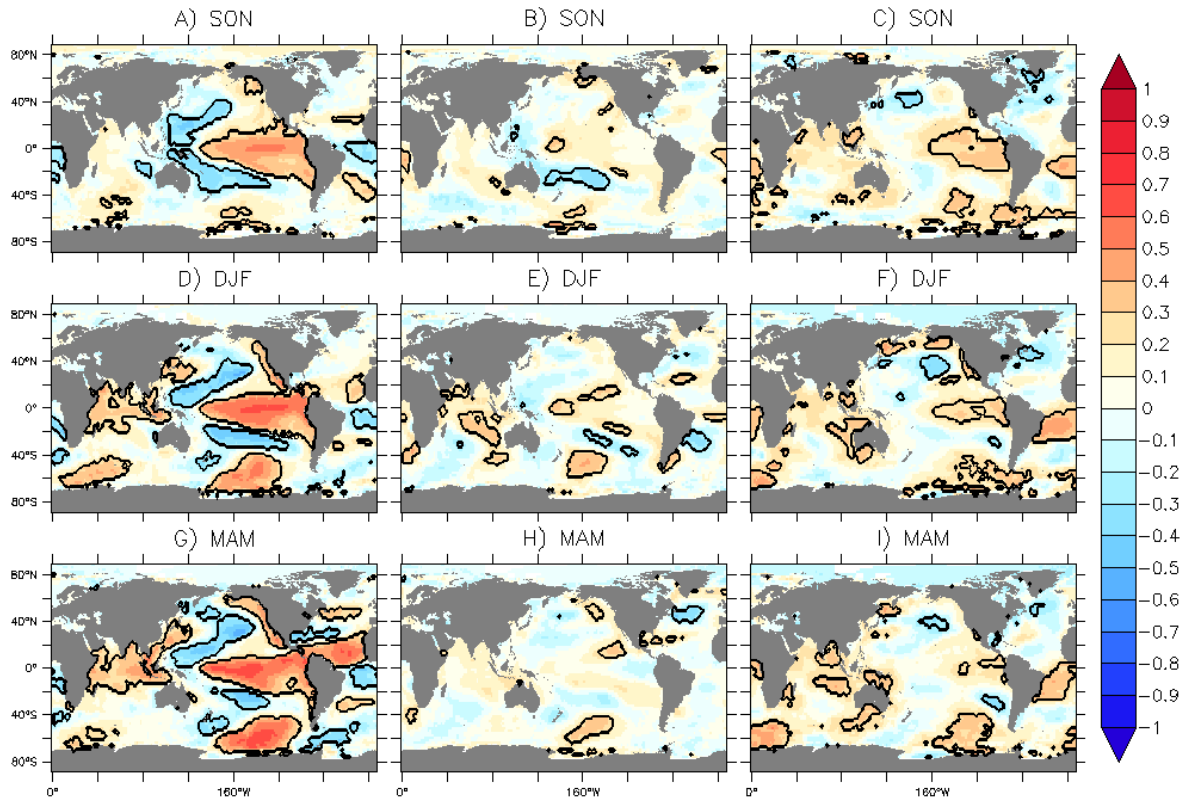


Figure 3.9: Spatial maps of correlation to SST anomalies. Panels A, D and G (left three panels) show the correlation between the S-EOF 1 Principal component and the contemporary SON, DJF and MAM SSTA anomaly at each gridpoint. Panels B, E and H show the same but for the principal component of S-EOF 2 and panels C, F and I for the principal component of S-EOF 3. Contours represent areas where the correlations are significant at the 95% test level according to a non-naive Student t-test with a modified sample size at each grid-point according to the procedure shown Chapter 2.

Figure 3.9 (panels A, D and G) shows that ENSO SST anomalies correlated with this mode are present over the Pacific Ocean during the SON season and intensify through DJF and MAM. The PC time series associated with this mode (shown in figure 3.10) is dominated by strong positive peaks (above 1 standard deviation) during the 57/58, 65/66,

82/83, 91/92, 97/98 and 2009/2010 El Niño events and significant spectral peaks for periods of 2.5, 3.5 and 10 to 12 years. The SST anomalies observed over the Atlantic Ocean are also present during the SON season and intensify peaking during the MAM season. To further understand the relationship between the S-EOF modes and El Niño, Figure 3.11 shows the lead-lag correlations of each S-EOF PC to the Niño 3.4 index. We see that for the S-EOF 1 the relationship between the PC and the Niño 3.4 index peaks during MAM as suggested by the SST anomalies associated with this mode, indicating that the El Niño influence over South America is it's strongest during the turn around and beginning of it's decay.

We can see from the S-EOF 1 patterns that over the southern part of South America (south of 20S) positive anomalies associated with En Niño events are constant as the seasons progress with peak intensity during SON, consistent with previous EOF studies for the SON, DJF and MAM (Paegle and Mo (2002), Grimm (2011)) and rain gauge studies over Uruguay (?). Negative anomalies during SON are more similar to those captured in the SON EOF 2 and are associated with a suppressed ITCZ during El Niño events. These negative ITCZ anomalies migrate southward as the season progress to form the previously know patterns of DJF and MAM variability associated with ENSO during these seasons.

The second S-EOF mode, shown in figure 3.8 panels B, E and H, captures the strong precipitation variability during DJF that characterizes the first DJF EOF mode. We see that during SON, the anomalies captured by this S-EOF mode are dipolike with negative precipitation anomalies over eastern Brazil and positive precipitation anomalies over SESA (figure 3.8 panel B). These anomalies resemble in terms of spatial pattern the SON EOF 1 anomalies but with much weaker intensities for both positive and negative anomalies. From DJF to MAM we see that the dipole of anomalies over SESA and eastern Brazil reverses again leading to a MAM pattern that resembles the MAM EOF 2. The reversal of anomalies from DJF to MAM implies that the mechanism driving the DJF precipitation anomalies associated with this mode is strongly restricted to the DJF season. This mode shows strong spectral peaks at 3, 5 and 20 year periods and shows strong principal component peaks for both El Niño and La Niña events shuch as 63/64 and 84/85 respectively. The Principal

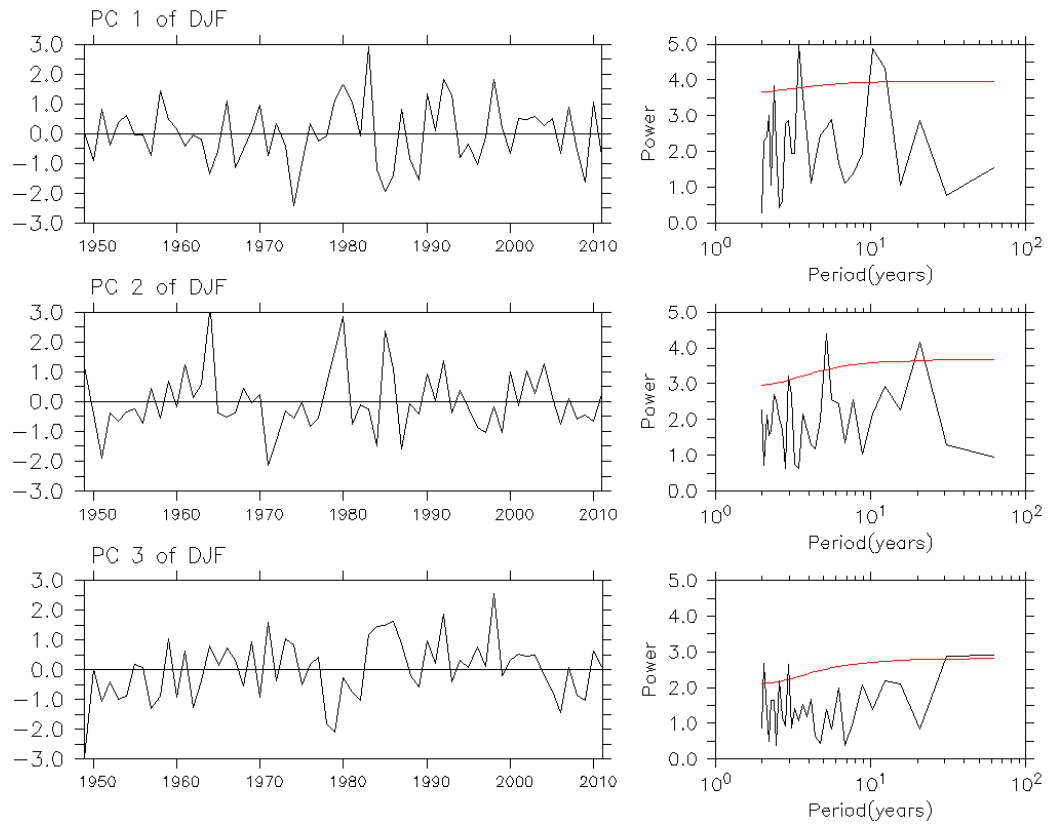


Figure 3.10: Principal Components of the first three S-EOF modes of variability in PREC/L precipitation anomalies and their corresponding power spectra.

component of this S-EOF mode has a correlation value to the DJF EOF 1 of 0.975.

SST anomalies associated with this mode (figure 3.9 panels B, E and H) show a weak meridional SST anomaly tripole during the SON season over the western and southern Pacific Ocean, with cold SST anomalies over the Southern Pacific showing much greater zonal extension than their equatorial and polarward counterparts. During DJF, positive SST anomalies over the equatorial western Pacific intensify while negative anomalies to the south weaken and move eastward. The positive SST anomalies over the southern Pacific greatly intensify and extend in area during DJF. DJF SST anomalies also show strong correlation over the Indian Ocean that did not appear before during the SON season as well as significant anomalies over the Atlantic. As shown in figure 3.11, the correlation between the S-EOF 2 PC and the Niño 3.4 index peaks during the contemporary SON and DJF season, but never reaches levels of statistical significance. Nevertheless, because the relationship between the S-EOF 2 and the Niño 3.4 index peaks during the peak of ENSO (towards the end of the calendar year) as well as the weak SST anomalies over the western Pacific associated with this mode, some influence of ENSO over this mode cannot be discarded, specially during strong ENSO events.

From the second S-EOF mode we see that the SON precipitation anomalies that share joint variability with the strong DJF precipitation anomalies are much less intense than the standard EOF and correlation between PC time series analysis would suggest. Seeing the weak SON precipitation anomalies captured by this S-EOF mode it seems reasonable to wonder if such weak precipitation anomalies could drive, via local surface-atmosphere processes, such a strong dipole of precipitation anomalies during the DJF season, and why do these strong anomalies appear and disappear so quickly.

The third S-EOF mode of variability captures during SON (Figure 3.8 panel C) similar widespread negative precipitation anomalies over the western part of the South American continent as the third SON EOF (figure 3.2 panel C) but with positive anomalies south of 20S. The SST pattern that accompanies this S-EOF mode during SON shown in figure positive SST anomalies over the eastern Pacific Ocean in a pattern somewhat similar to

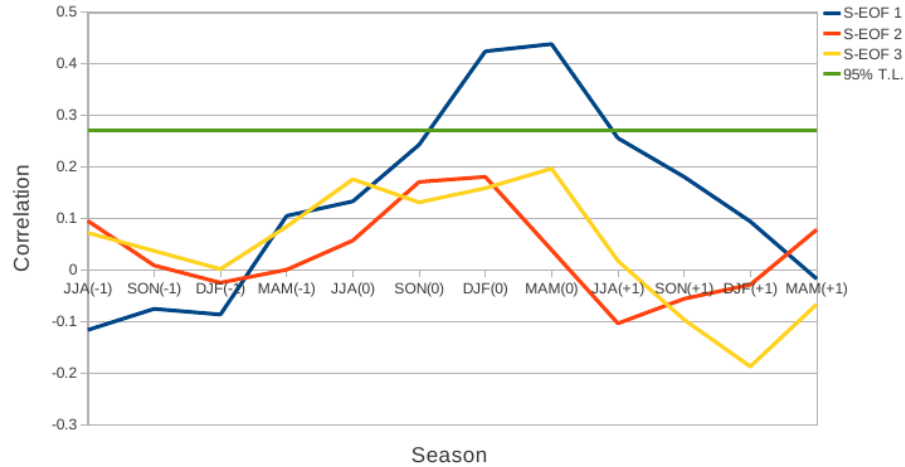


Figure 3.11: Lead-lag correlation coefficients of Niño3.4 SST index to the first three PC of the S-EOF analysis of PREC/L precipitation over South America. The green line represents the 95% significance level according to a naive Student t test.

ENSO SST anomalies but with the most intense anomalies confined to the western coast of South America. This type of SST pattern over the Pacific is associated with the SON EOF 2 (compare figure 3.4 panel C and figure 3.9 panel C), but the SST signature over the Atlantic Ocean for these two modes of variability is quite different. During DJF, this S-EOF mode shows the same strong banded structure as the DJF EOF 3 (compare figure 3.2 panel F and figure 3.8 panel F) which then remains into the MAM season (figure 3.8 panel I) but with weakened negative precipitation anomalies over eastern and central Brazil. The SST anomalies associated with this mode show a decrease of the significant anomalies over the Pacific Ocean from SON to DJF and then to MAM while the SST anomalies over the Atlantic increase their significance as the seasons progress. This S-EOF mode may capture the local ocean-atmosphere feedback processes between the SACZ and the Atlantic Ocean.

Figure 3.12 shows the regression of the PCs of the first three S-EOF modes to 200mb wind anomalies. For the first S-EOF mode, the wind anomalies associated with this mode during SON consist of strong upper level easterlies over the Pacific Ocean and westerlies over the northern part of the South American continent as well as an anticyclone over SESA. Over the South Pacific a teleconnection signal can be seen extending from the Pacific warm

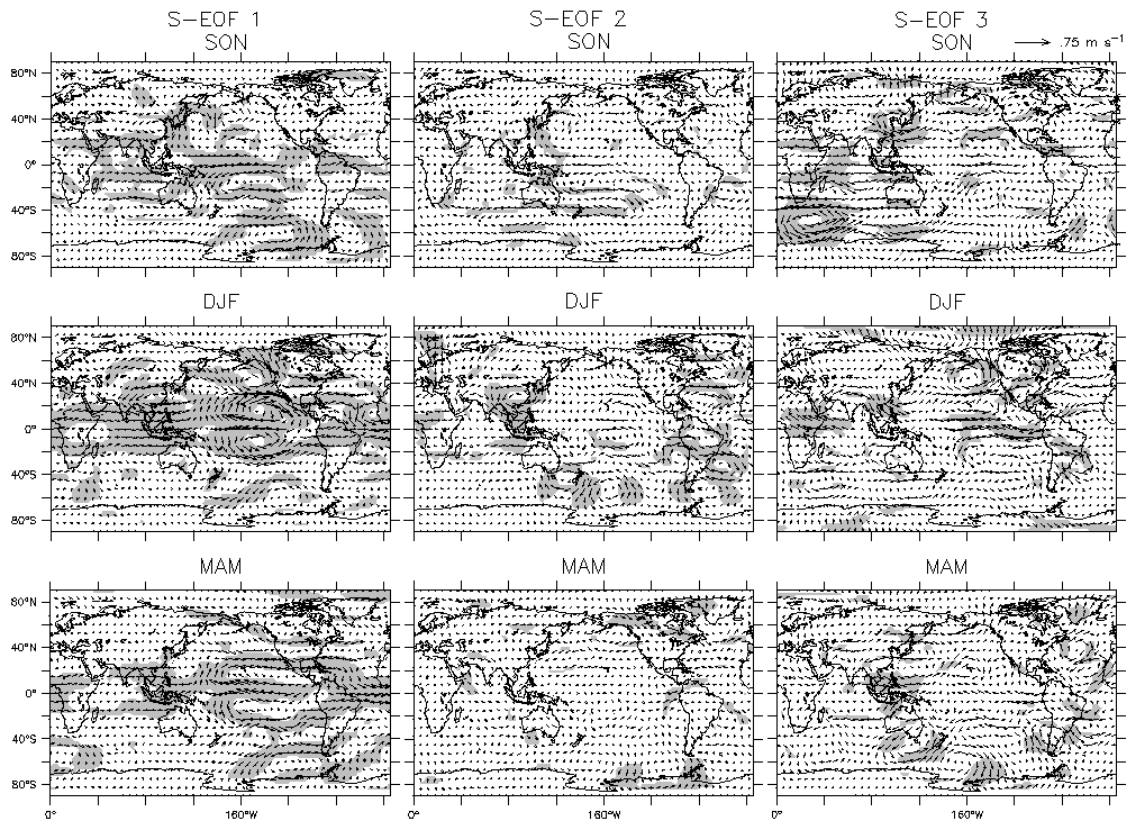


Figure 3.12: Regression of the first three PCs of the S-EOF analysis of PREC/L precipitation over South America to 200mb wind anomalies. Shading shows areas where at least one of the components has a 95% significant correlation to the corresponding PC.

pool region towards the south American continent that generate upper level anticyclonic circulation over SESA and produce the enhanced rainfall over SESA characteristic of El Niño over the region. As the seasons progress, the equatorial wind anomalies associated with this mode greatly intensify during DJF generating upper level convergence over most of northern South America, while the extratropical teleconnection pattern appears weaker during the DJF season. During MAM strong anomalous winds dominate the upper levels over eastern Brazil and the Nordeste region with some teleconnection like anomalies over the southern Pacific. This seasonal change in how ENSO affects the South American region via anomalous winds, with teleconnections predominant during SON and MAM and equatorial winds during DJF, has been previously reported by Cazes-Boezio et al. (2003) using EOF analysis of 200mb seasonal mean winds and is here captured in one S-EOF mode.

For the second S-EOF mode, we see almost no anomalous 200mb winds associated with this mode during SON and MAM while during DJF, we see a clear teleconnection pattern that seems to link the maritime continent to the circulation anomalies over the South American continent. For the third S-EOF mode we observe little associated wind anomalies during SON. During DJF we see some upper level easterlies over the eastern and central Pacific and a clear cyclonic circulation over SESA that remains through to the MAM season.

3.3.1 S-EOF analysis of GPCP precipitation data and comparison to PREC/L S-EOF results.

In this section we will discuss the results for the S-EOF analysis of GPCP data and compare them to S-EOF results for PREC/L data for the complete period 1948-2010 discussed in the previous section and for the subperiod 1979-2010 for which both datasets have coverage. This analysis is limited to GPCP data due to the good agreement between EOF modes shown in GPCP and CMAP shown in subsection 3.2.2.

Figure 3.14 shows the eigenvector maps of the first three S-EOF modes of GPCP and PREC/L data for the period 1979-2010. The percentage variance represented by each of

the first three modes of both analysis is shown in figure 3.13. As we can see the first three modes of both datasets account for very similar fractions of the total variance. The first S-EOF mode of GPCP is well separated from the other modes while the first S-EOF mode of PREC/L shows slight degeneracy with it's following mode.

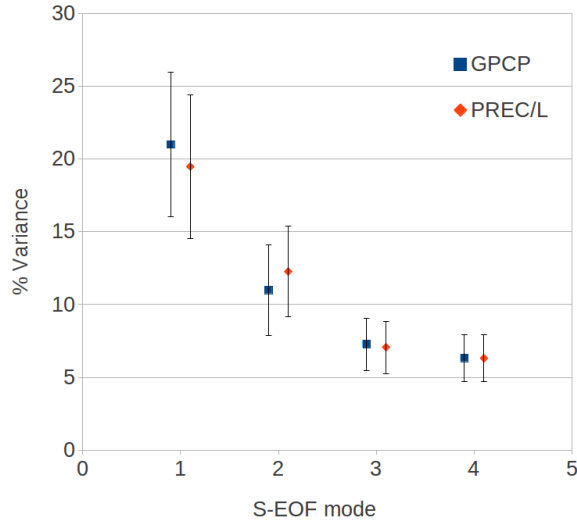


Figure 3.13: Percentage of variance explained by each of the first three S-EOF modes of GPCP and PREC/L for the period 1979-2010. Error bars are calculated according to the North et al. (1982) rule of thumb.

The first mode in both datasets for this period captures the seasonal evolution of the meridional dipole mode (first two columns of figure 3.14) with both patterns being in very good agreement for all the seasons studied. This first mode in both datasets is the same as the S-EOF 1 of PREC/L data for the 1948-2010 period but for the 1979-2010, in both datasets, explains a higher percentage of the variance then for the complete period available. We see that the PC time series corresponding to this mode in both datasets represents almost identical temporal variability with a correlation value between the two of 0.98. SST

anomaly correlation maps for the first three S-EOF modes of GPCP and PREC/L data are shown in figures A.1 and 3.19. For the meridional dipole S-EOF mode, both show the same progression of ENSO SSTs over the Pacific as discussed for this mode in the previous section with some difference, mainly weaker SST anomalies, over the Atlantic Ocean for this shorter period.

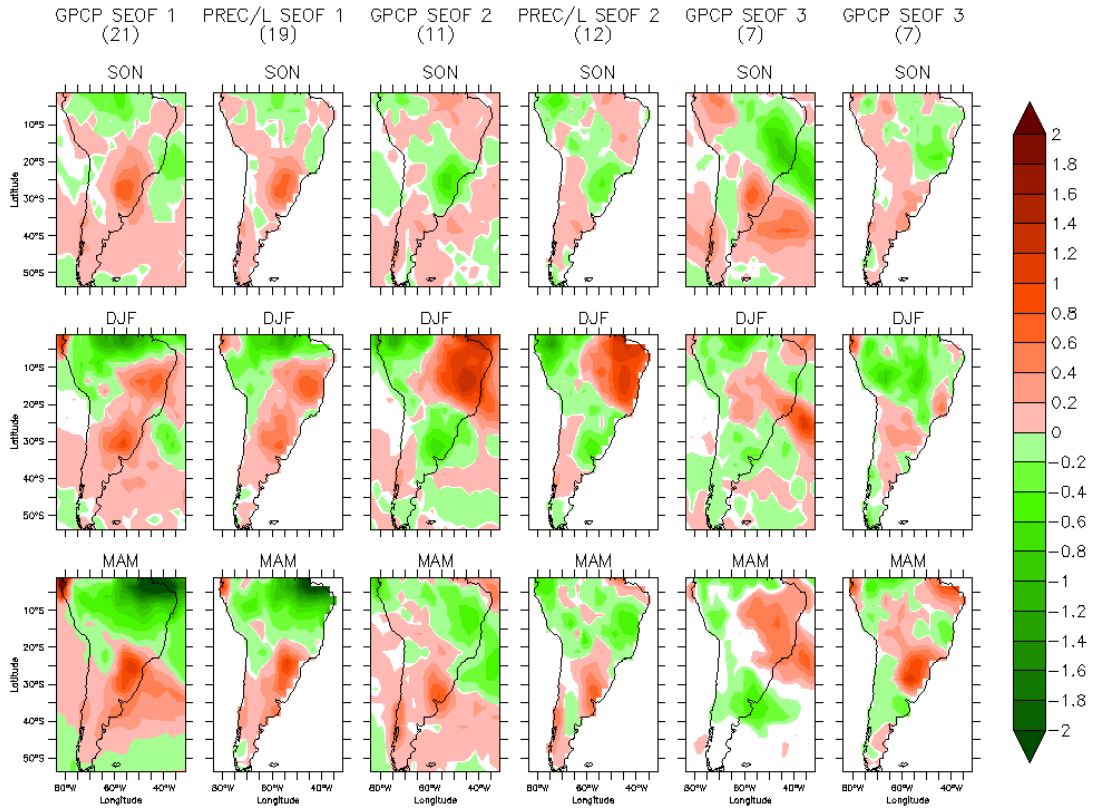


Figure 3.14: Eigenvector maps of the first three S-EOF modes of GPCP and PREC/L data for the period 1979-2010. The numbers inside the parenthesis represent the % variance explained by each mode.

The second S-EOF mode in both datasets is also highly correlated in terms of their time series (mid panel in figure 3.15) with a correlation value of 0.94 between the two time series. This mode accounts for 11 and 12 % explained variance in GPCP and PREC/L respectively. It shows some degeneracy with the following S-EOF mode in GPCP data but in PREC/L it is well separated from the following S-EOF 3 mode.

This second S-EOF mode in both datasets captures the continental tripole pattern

of variability during DJF, but unlike the S-EOF analysis for the 1948-2010 period, the DJF continental tripole mode is not preceded by the SESA-SACZ dipole during SON. This means that for the period 1979-2010 neither GPCP or PREC/L data capture the reversal of precipitation anomalies and instead, show that the DJF continental dipole mode is preceded during SON by a similar tripole pattern with negative anomalies over SESA of comparable magnitude as those seen during DJF and weaker anomalies to the north, with positive precipitation anomalies over eastern Brazil being specially weak. SST patterns for this mode show (central column of panels in figures A.1 and 3.19) no significant correlation to equatorial Pacific SST anomalies during any season and shown only some SST anomalies over the southern Pacific during DJF. Atlantic SST anomalies are weak during SON for this mode in both datasets but significant solid anomalies are seen underlying the SACZ during DJF and over the equatorial North Atlantic during MAM for both datasets.

The SESA-SACZ dipole pattern which is dominant during the SON season in all standard EOF analysis reviewed in this work is captured by here by the third S-EOF mode of both GPCP and PREC/L. In the GPCP S-EOF 3, the pattern is well defined with strong centres of variability over SESA and the SACZ. In PREC/L, this same pattern appears in general weaker and with SESA anomalies being specially weak in this dataset. The PC time series associated with the S-EOF 3 in each dataset have a correlation to each other of 0.23, and it is clear from their PC time series that their temporal evolution is quite different.

The SESA-SACZ dipole pattern during SON evolves very differently into the DJF season in both datasets. For GPCP, the SESA-SACZ dipole modes appears to shift northward with new negative anomalies appearing over SESA. During MAM positive anomalies have extended over most of the eastern Brazil region while negative anomalies over SESA become more intense, completely reversing the polarity of the SESA-SACZ dipole compared to SON. For PREC/L the SON SESA-SACZ dipole evolves into strong negative anomalies over most of the continent north of 20S and weak negative anomalies to the south. During MAM, the northern negative anomalies retreat northward while positive anomalies over SESA intensify and extend north. This mode shows the greatest differences in terms of associated SST

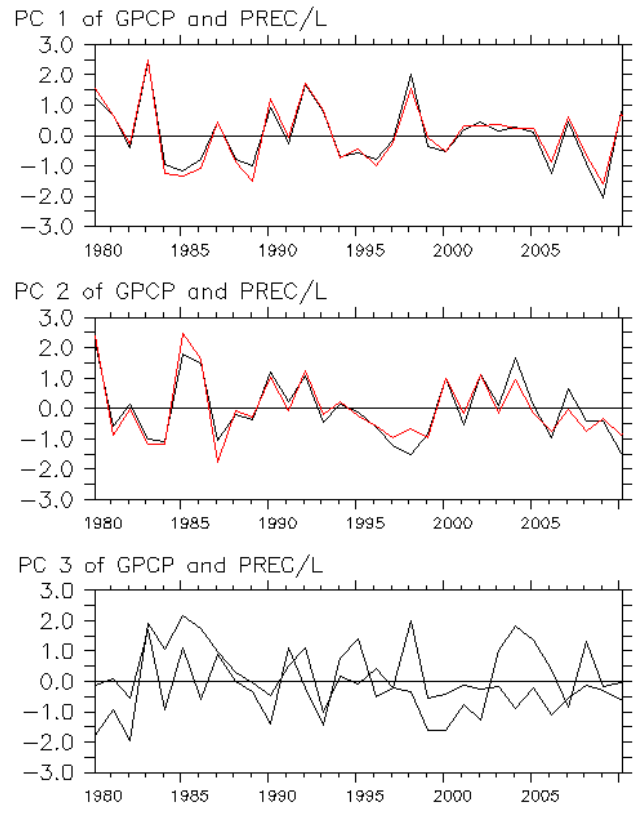


Figure 3.15: PC time series of the first three S-EOF modes of GPCP (black) and PREC/L (red) data for the period 1979-2010. Correlations between the PC time series are 0.98 for S-EOF 1, 0.94 for S-EOF 2 and 0.23 for S-EOF 3.

anomalies specially over the Pacific, where GPCP shows significant SST anomalies during SON and DJF over the central Pacific while PREC/L data shows Pacific SST anomalies more strongly confined to the eastern Pacific.

It seems clear from the results of this section that the relationship between the SESA-SACZ dipole mode during SON and the continental tripole mode during DJF, if existent, is quite different during the last 30 years to that of the 1948-2010 period for which we have available data.

To compare the 1948-1979 period to the 1979-2010 period we perform S-EOF analysis of both sub-periods using PREC/L data. For this comparison we will focus on the differences between the seasonal evolution of variability leading up to the DJF continental tripole mode as well as the characteristics of the ENSO forced variability over the region. The first three S-EOF modes of PREC/L data for the period 1948-1979 account for 13, 12 and 7 % of the observed variance in the dataset. The first important difference between the S-EOF results for both periods is the strong degeneracy between the first two S-EOF modes of the 1948-1979 period.

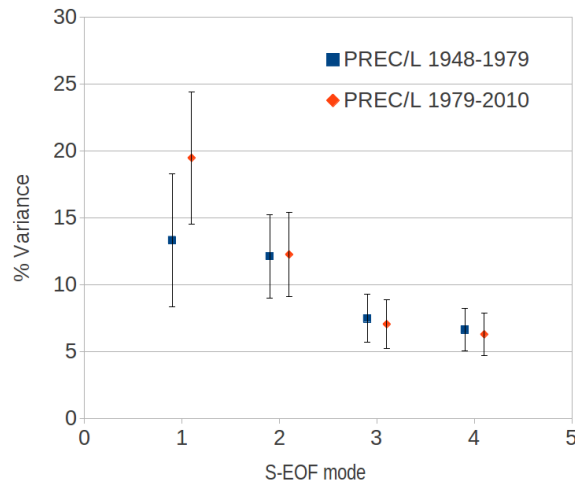


Figure 3.16: Percentage of variance explained by each of the first three S-EOF modes of PREC/L for the periods 1948-1979 and 1979-2010. Error bars are calculated according to the North et al. (1982) rule of thumb.

The spatial patterns for the first three S-EOF modes of each sub-period are resented in

figure 3.17 and correlation maps to SST anomalies for the periods 1948-1979 and 1979-2010 are presented in figures 3.18 and 3.19 respectively.

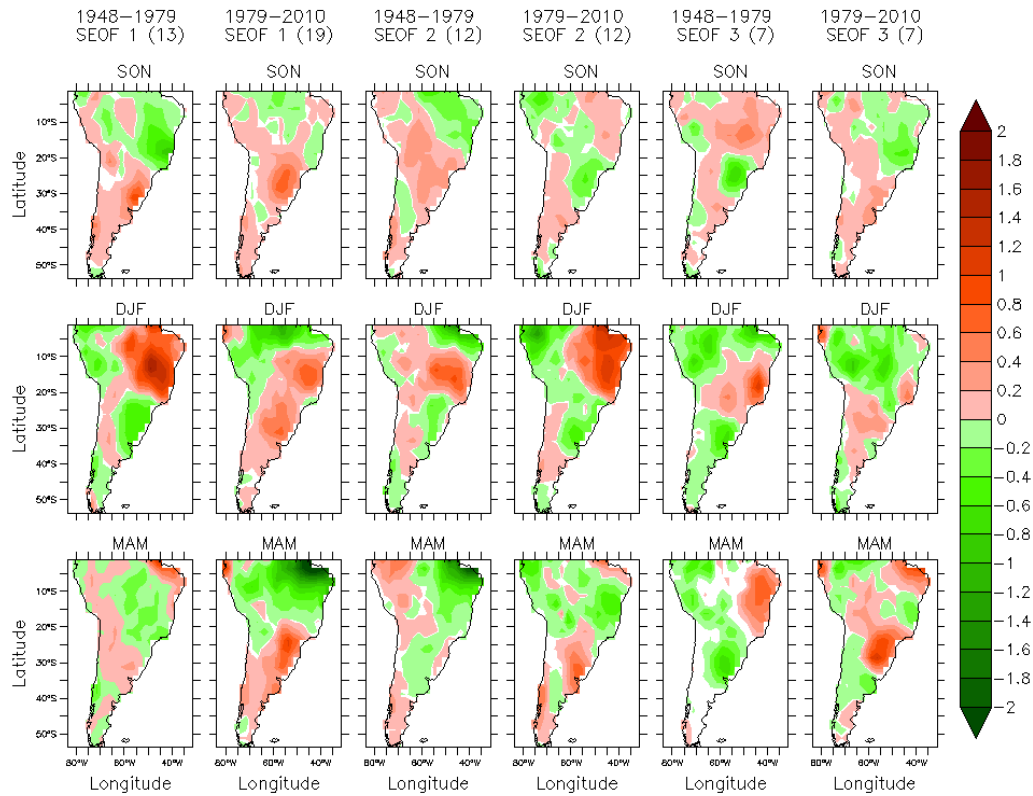


Figure 3.17: Eigenvector maps of the first three S-EOF modes of PREC/L data for the sub-periods 1948-1979 and 1979-2010. The numbers inside the parenthesis represent the % variance explained by each mode.

The leading S-EOF mode for the period 1948-1979 captures the seasonal evolution of the SON SESA-SACZ dipole mode into the DJF continental tripole mode (first column of figure 3.17) and then into a spatial pattern with widespread negative anomalies over the central part of the South American continent. This evolution is the same as captured by the second S-EOF mode of PREC/L precipitation for the complete 1948-2010 period shown in figure 3.8. During the 1979-2010 period on the other hand, the seasonal evolution of the continental tripole mode is quite different from the 1948-1979 period. The continental tripole mode during the second epoch is captured by the second S-EOF mode and shows that the DJF continental tripole mode is preceded by anomalies of the same sign during SON.

Hence, clear change is seen in the relationship of the DJF continental tripole mode with precipitation anomalies during the preceding season. The evolution of the DJF continental tripole mode into MAM is similar for sub-periods of data with the main difference that for the 1979-2010 sub-period anomalies over the La Plata basin are stronger in intensity.

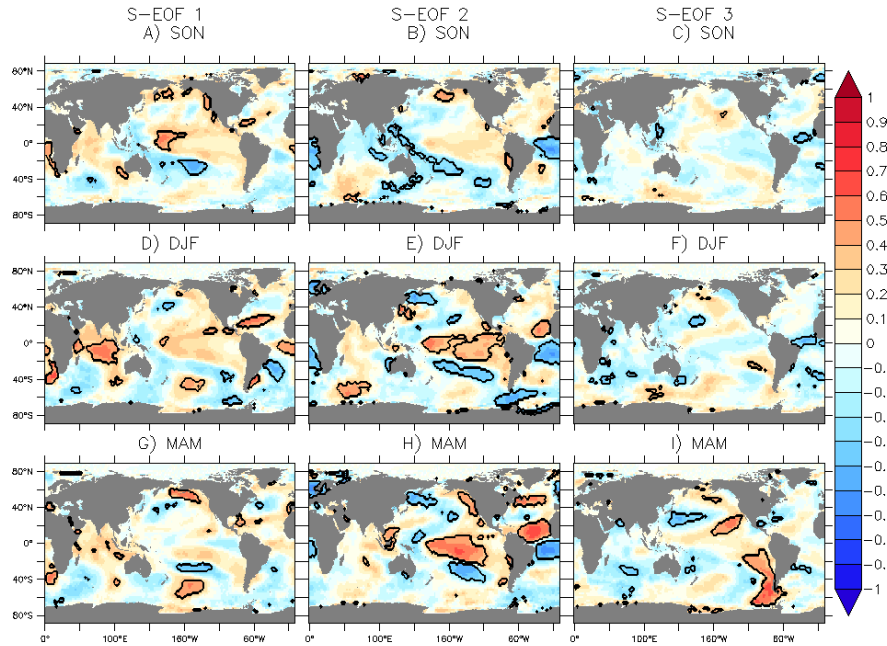


Figure 3.18: SST correlation maps between the PC time series of the first three S-EOFs of PREC/L precipitation for the 1948-1979 period. Contours represent areas where the correlations are significant at the 95% test level according to a non-naïve Student t-test with a modified sample size at each grid-point according to the procedure shown Chapter 2.

The relationship of the S-EOF mode that contains the DJF continental tripole mode to SST anomalies also shows a clear change from the first epoch to the second. This can be seen by comparing the S-EOF 1 SST anomaly correlation maps for the period 1948-1979 (left column of figure 3.18) to the S-EOF 2 SST anomaly correlation maps for the period 1979-2010 (center column of figure 3.19). During the first epoch, central Pacific SST anomalies that accompany the SON SESA-SACZ dipole are captured by the SON and DJF panel of SST anomalies of the S-EOF 1, while during the second epoch, this type of localized SST anomalies over the western Pacific do not appear for any mode, even the

S-EOF 3 of the second epoch which shows an SON pattern most similar to the SESA-SACZ dipole (compare panel A of figure 3.18 to panels B and C of figure 3.19). During DJF, SST anomalies associated with the DJF continental tripole mode over the Southern Atlantic are similar for both sub-periods. Over the Northern Atlantic and Indian Ocean however, the DJF continental tripole mode shows correlated SST anomalies during the first epoch that do not appear in the second (compare panels D of 3.18 and E of 3.19).

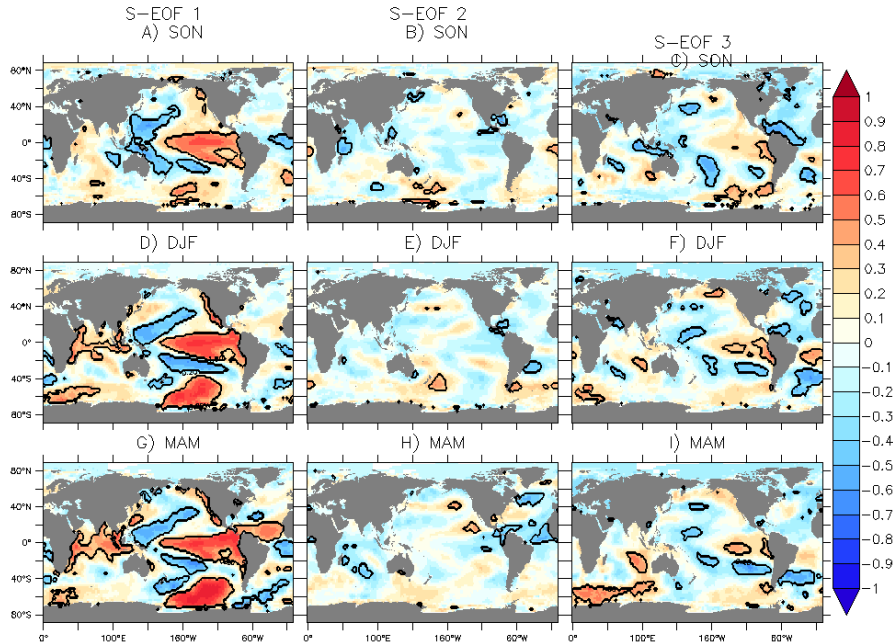


Figure 3.19: Same as in figure 3.18 but for the 1979-2010 period.

Comparing the 200mb geopotential height anomalies associated with this mode in both periods, panels A and D of figure 3.20 for the S-EOF 1 of the first epoch and panels B and E of figure 3.21 we see that the DJF continental tripole mode is associated in both cases with an upper level low pressure anomaly over South East South America. During the first epoch, this anomaly is stronger and is embedded into an anomalous wave train that spans the southern Pacific, from Australia to South America (figure 3.18 panel D). In the previous SON season, no upper level circulation anomaly is seen related to this mode, but considering the strong degeneracy of the two first S-EOF modes of the 1948-1979 epoch, this part of the mode may be captured by the second S-EOF, which does show upper level circulation

anomalies in the area. During the second epoch, the DJF continental tripole mode is associated with the same type of upper level low and cyclonic circulation over SESA as in the first epoch but less intense with the crucial difference that during this epoch, the upper level vortex over South America is not part of the same Southern Pacific teleconnection as in the first epoch (panel E of figure 3.21). During SON, a similar upper level vortex as DJF is seen over South America (panel B of figure 3.21) again with no significant link to the observed anomalous wave activity over the South Pacific. These results make it clear that the DJF continental tripole pattern is strongly dependent on the upper level circulation anomalies over SESA but that these circulation anomalies may appear as part of a forced teleconnection pattern or as a form of local internal variability in the region.

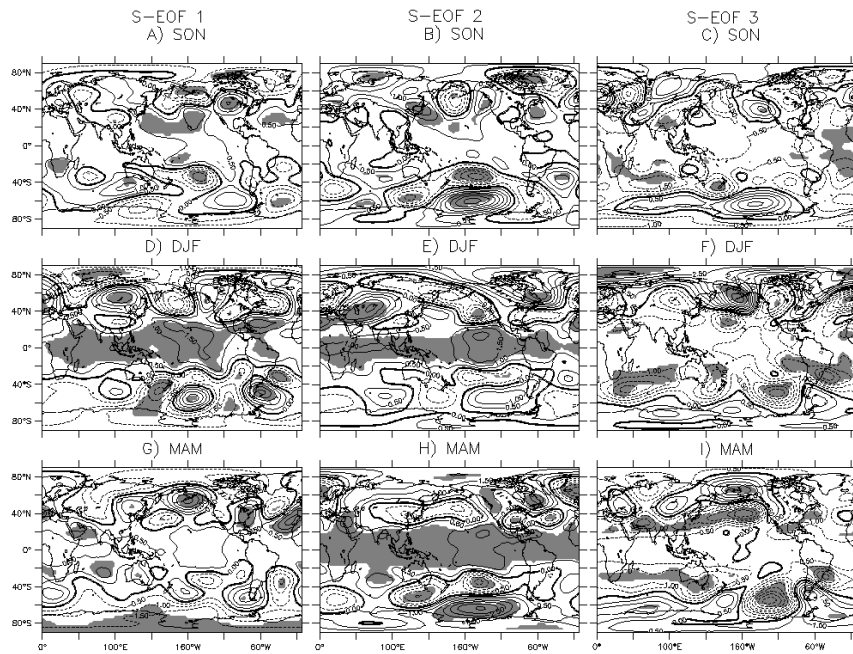


Figure 3.20: 200mb Hgt regression maps between the PC time series of the first three S-EOFs of PREC/L precipitation for the 1948-1979 period. Shading represent areas where the correlations are significant at the 95% test level according to a non-naive Student t-test with a modified sample size at each grid-point according to the procedure shown Chapter 2.

The ENSO influence over South America also shows a marked difference between these two periods as captured by the S-EOF 2 of the 1948-1979 epoch and the S-EOF 1 of

the 1979-2010 epoch. The variance of precipitation over South America explained by the ENSO mode during the early periods studied is much less than for the second period (12 and 19% respectively). During SON, both modes represent a meridional dipole of anomalies with SESA anomalies being more intense during the second period and equatorial South American anomalies dominating during the first period. During DJF, both modes show negative precipitation anomalies over the Nordeste region and positive anomalies to the south over the SACZ, with an important difference being anomalies over SESA, which are negative during the first epoch and positive during the second epoch. During MAM, both modes show negative anomalies over the Nordeste and central Brazil region with these anomalies extending across the complete continent for the second epoch. Over SESA, the MAM ENSO modes show quite different anomalies, with negative anomalies over the region during the first epoch and strong positive anomalies during the second epoch. Comparing the SST patterns of the ENSO modes of both epochs, it is clear that for the first epoch the effects of ENSO over South America are represented by the first two modes, the first capturing the effects of ENSO in its developing phase (during the SON season) while the second mode represents the influence of ENSO in its mature and decaying phase (during the DJf and MAM seasons), while during the second epoch these effects are captured integrally by the first S-EOF mode.

3.4 Summary

In this chapter we have performed the EOF and S-EOF analysis of PREC/L, GPCP and CMAP precipitation datasets with the objective of finding the leading modes of precipitation variability during DJF, test their robustness across datasets and characterize the seasonal evolution of the observed precipitation variability over the region from SON to DJF and on to MAM.

We found that the dominant DJF mode of precipitation variability is what we have denominated the continental tripole mode of variability which appears as the EOF 1 mode in PREC/L data for the period 1948-2010 and sub period 1979-2010, and GPCP and CMAP

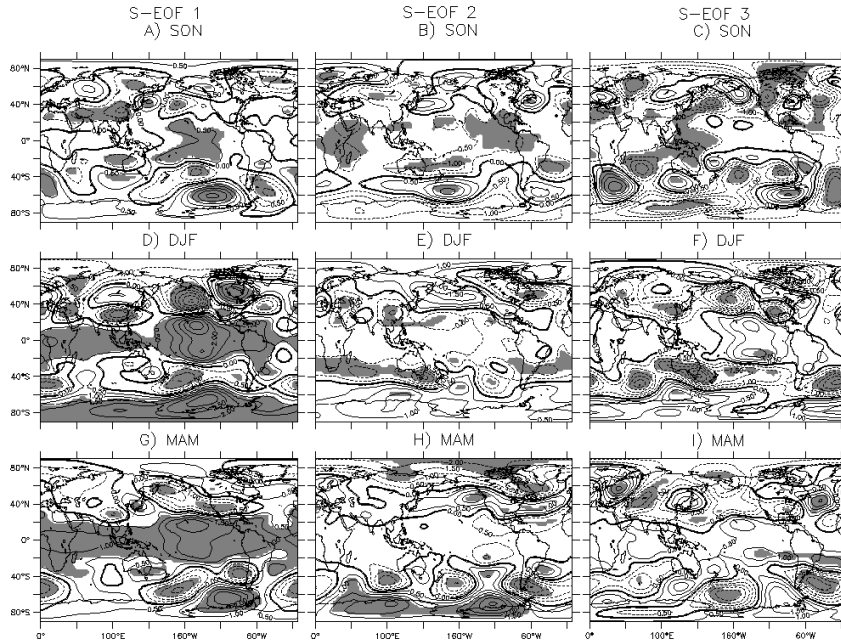


Figure 3.21: Same as in figure 3.20 but for the 1979-2010 period.

data for the period 1979-2010. This mode characterized by strong anomalies over eastern Brazil and opposite anomalies over SESA and the western Amazon basin and by correlated SST anomalies only over the subtropical Atlantic off the Brazilian coast. This DJF mode has been observed before by Paegle and Mo (2002) as the fourth DJF rotated EOF mode and by Grimm and Zilli (2009) as the first mode of DJF variability. This precipitation mode has been strongly linked to an upper level vortex centered over SESA that appears to be the cause of the precipitation anomalies (Zamboni et al. (2009)Zamboni et al. (2011)). This first mode is well separated from other modes in all datasets. The second DJF EOF mode captures the meridional dipole between the Nordeste and tropical continental areas to the north and the SACZ and SESA to the south. This second DJF EOF mode is clearly linked to ENSO SST anomalies.

For SON, the leading mode of variability is characterized by what we have labelled the SESA-SACZ dipole mode due to it's characteristic spatial pattern of precipitation anomalies. It is present in all datasets analysis and appears as well separated in all analysis with the exception of the PREC/L EOF analysis for the period 1948-2010. The SESA-SACZ dipole

mode is correlated to ENSO type SST anomalies for the PREC/L 1948-2010 EOF analysis. In GPCP and CMAP analysis, this mode is related to central Pacific warming type of SST anomalies. The second SON EOF mode is a meridional dipole type mode and is related to SST anomalies over the eastern Pacific Ocean. We observe that these two SON modes are better separated for the analysis done for the 1979-2010 period than in those analysis where the complete 1948-2010 period is used.

The leading MAM mode is a meridional dipole type mode with strong anomalies over the Nordeste region and opposite anomalies over SESA. This leading MAM mode is clearly produced by ENSO and is well separated from all other modes.

In terms of the seasonal evolution of precipitation anomalies we find from EOF analysis of PREC/L data that the previously observed statistically significant correlation between the SESA-SACZ dipole mode and the DJF continental tripole mode (Grimm and Zilli (2009)) is present but appears as a weak correlation only significant at the 80% test level while for GPCP and CMAP data for the period 1979-2010 the correlation is very weak and not significant. A statistical link between the SON SESA-SACZ dipole and the DJF continental tripole pattern would imply that precipitation anomalies over eastern Brazil have a tendency to reverse from SON when anomalies are produced by ENSO, to DJF when ENSO does not act on the region directly and local surface atmosphere processes enhanced by soil moisture anomalies from SON act to reverse the precipitation dipole of anomalies.

Using S-EOF analysis we find similar results to those from standard EOF analysis, namely that the SON SESA-SACZ diople pattern is associated with the DJF continental tripole pattern when using the time period 1948-2010 but that this relationship is not present for the period 1979-2010 in GPCP or PREC/L. To compare the seasonal evolution of the modes separated the PREC/L data into two periods, 1948-1979 and 1979-2010 and performed S-EOF analysis as well as correlation to SST ans regressions to 200mb geopotential height anomalies. For the first epoch, the DJF continental tripole mode is lead by the SESA-SACZ dipole mode during the preceding SON season, for the second epoch however,

this relationship does not hold. These analysis show that the DJF continental tripole mode and it's corresponding upper level vortex over South America may appear both as a part of the influence of ENSO over the region and related to previous SOB SESA-SACZ dipole of opposite anomalies, but also independently of ENSO and correlated to previous SON precipitation anomalies of the same sing over SESA and eastern Brazil.

In light of these results we propose a direct method of Eastern Brazil precipitation anomalies in the next chapter.

CHAPTER 4

DIRECT STUDY OF EASTERN BRAZIL PRECIPITATION ANOMALIES, THEIR INTERANNUAL VARIABILITY AND SEASONAL EVOLUTION.

As the results in chapter 3 show, the study of the seasonal evolution of the modes of variability over South America using EOF analysis carries with it the difficulty of clearly interpreting the relationships between the EOF modes of each season. S-EOF analysis showed that the major mode of variability during DJF was preceded by very weak precipitation anomalies over the South American region during SON, leading us to conjecture that perhaps the mechanisms that drive this mode are strongly confined to the DJF season. Because of this observation we propose in this chapter two different methods of studying this mode of variability that may give some more insight as to the mechanisms behind this mode.

In section 4.1 we define the Eastern Brazil Precipitation Index (EBPI) to characterize precipitation variability over the region where the DJF EOF 1 mode shows the most intense variability. We use this index in correlation and regression analysis to monthly maps of different atmospheric variables to understand the evolution and mechanisms behind this strong mode of variability. In section ?? we explore the use of S-EOF analysis of bimonthly seasons as a possible way to overcome the degeneracy between the first two S-EOF modes shown in the previous chapter and more clearly isolate the seasonal evolution of each mode of variability.

4.1 The Eastern Brazil Precipitation Index as a tool to understand the variability of precipitation over South America.

The Eastern Brazil Precipitation Index (EBPI) is defined as the area average precipitation anomaly in the region between 0 and 20S and 30W to 55W. As we can see from figure 4.1

this region is to the east of the DJF climatological precipitation maximum and is where we observe the strong positive precipitation anomalies captured in the DJF EOF 1 and in the DJF spatial pattern of the S-EOF 2.

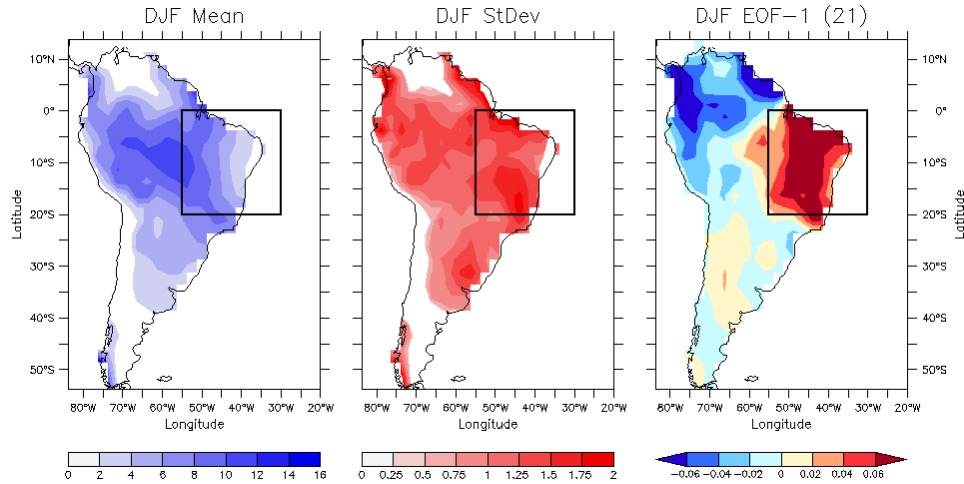


Figure 4.1: Climatological mean DJF precipitation from the PREC/L dataset from 1948-2011, standard deviation of DJF seasonal mean precipitation and first DJF EOF mode of PREC/L data for the same period. The black boxes over the maps represent the area where the EBPI is defined.

The correlations between the Principal components of the DJF EOF 1 and the S-EOF 2 modes to the EBPI time series of the DJF season as well as the individual December, January and February month are shown in 4.1. We can see that the mode of variability captured in the DJF EOF 1 and S-EOF 2 modes is heavily dominated by the January and February precipitation anomalies over the EBPI region, with December precipitation anomalies showing little significant correlations to the PC's of the EOF and S-EOF modes we wish to study further restricting this mode of variability to the January and February months. It is because of this reason that we will from now on, use the EBPI time series of the January and February mean anomalies as the reference time series in our correlation analysis.

	DJF EOF 1	S-EOF 2	DJF EBPI	Dec EBPI	Jan EBPI	Feb EBPI
DJF EOF 1	1	*0.976	*0.973	0.256	*0.702	*0.705
S-EOF 2		1	*0.948	0.281	*0.677	*0.669
DJF EBPI			1	0.280	*0.692	*0.744
Dec EBPI				1	0.271	0.039
Jan EBPI					1	0.309
Feb EBPI						1

Table 4.1: Correlation table between the DJF EOF 1 Principal Component, the S-EOF 2 Principal Component, The DJF EBPI, and the monthly EBPI for December, January and February. Correlations with an star are significant at the 99% test level.

4.1.1 Regression analysis of atmospheric variables onto EBPI.

The regression of monthly precipitation anomalies onto Jan-Feb EBPI anomalies is shown in figure 4.2 and shows, over South America during January and February a precipitation pattern very similar as that captured by both the DJF EOF 1 and the S-EOF 2 for the DJF season. During the previous October, the anomalies over South America show a weak dipole pattern of precipitation that intensifies trough to December. These precipitation anomalies are similar to those captured in the second S-EOF mode for the SON season and imply that if there is any reversal of the precipitation anomalies over eastern South America, this reversal happens from December to January and not from November to December as previously suggested in the literature.

Looking at the global pattern of precipitation associated with this mode, we see that from December to March, precipitation anomalies over the western part of the Indian Ocean, off the coast of Madagascar seem to be strongly related to precipitation anomalies over eastern South America, with suppressed precipitation over both regions during December and March and enhanced precipitation during January and February. Eastern Brazil precipitation anomalies also show a significant link to precipitation anomalies over the tropical West Pacific and Maritime Continent. This relationship to western Pacific precipitation is strongest during the preceding months of October and November, weakens during December and then restrengthens during January to decay again from February onwards.

From the maps of 200mb geopotential height anomalies regressed onto the EBPI time

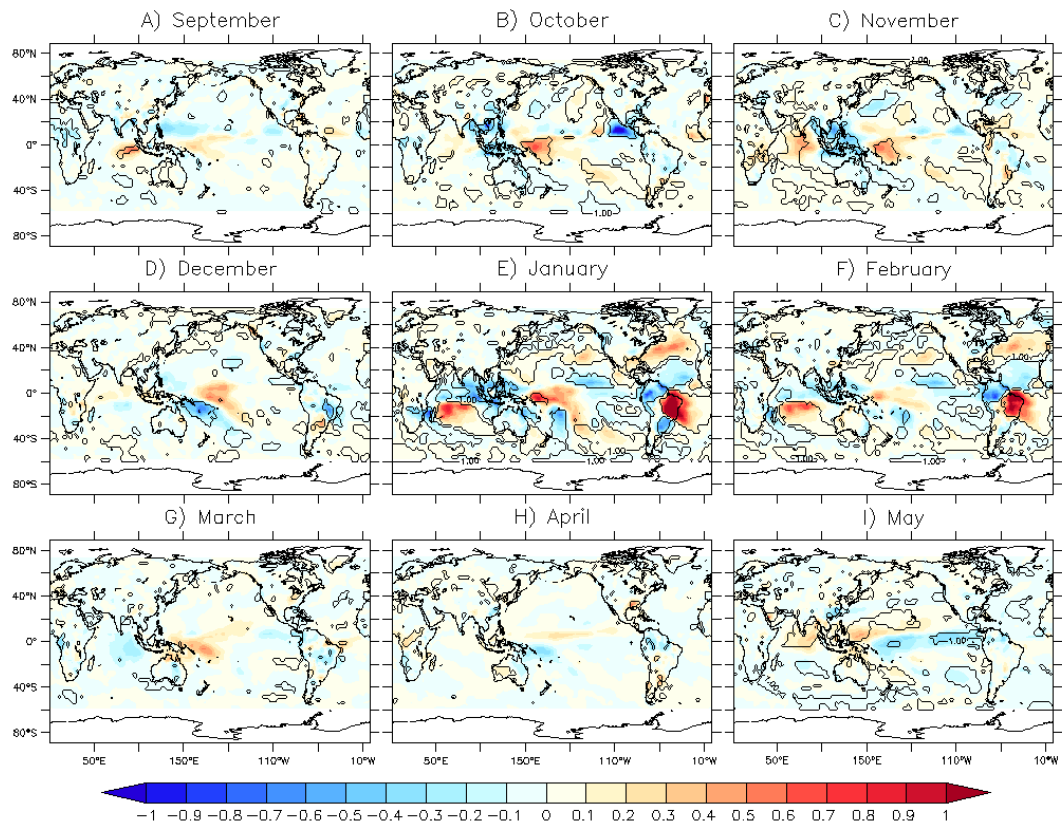


Figure 4.2: Regression maps of monthly precipitation anomalies onto the Jan-Feb EBPI time series, red colors are positive anomalies and blue colors are negative anomalies in units of mm/day. Black contours outline regions where the correlation between precipitation anomaly and EBPI is significant at the 90% test level.

series, we see during January and February a strong southern hemisphere teleconnection pattern that extends from the Indian Ocean region towards South America as well as a very strong meridional teleconnection extending from Eastern Brazil, northwards and southwards and has its strongest pressure anomaly signatures over 40N and 50S. Both the meridional and zonal teleconnection patterns seen during January and February are established rapidly. Both the meridional and zonal teleconnections observed during January and February show an equivalent barotropic structure as shown by the 850mb geopotential anomalies shown in figure B.1. During December, there is no sign of the meridional teleconnection during and, over the Southern Pacific, we observe some seemingly strong geopotential height anomalies that form a wavelike pattern that appears to have origin over the western Pacific and end over the eastern Pacific with little direct effect over South America.

During the previous October, we do see a clear teleconnection pattern extending from the western tropical Pacific to South America, generating upper level anticyclonic anomalies over SESA and cyclonic anomalies to the north, but this pattern dissipates by the November and has little low level signature as shown by figure B.1.

SST anomalies associated with EBPI precipitation are shown in figure 4.4 and are overall very consistent with those associated with the second S-EOF mode with a small area of positive SST anomalies over the western tropical Pacific from October to February and positive SST anomalies over the Indian Ocean from October through to March. SST anomalies over the Indian Ocean cover a large area of the basin with peak intensity during the month of January. We also observe a similar positive SST anomaly center over the south Pacific Ocean as was observed for the Second S-EOF mode and which appears to be present from the preceding September to the following May of the January-February for which the EBPI time series is centered around.

Wind anomalies regressed onto the EBPI time series of anomalies over South America at 200mb and 850mb are shown in figures 4.5 and 4.6 respectively. During January, we see very strong upper level circulation anomalies with a strong anticyclone centered about 50S that spans most of the south Atlantic and to the north, a cyclone anticyclone pair of circulation

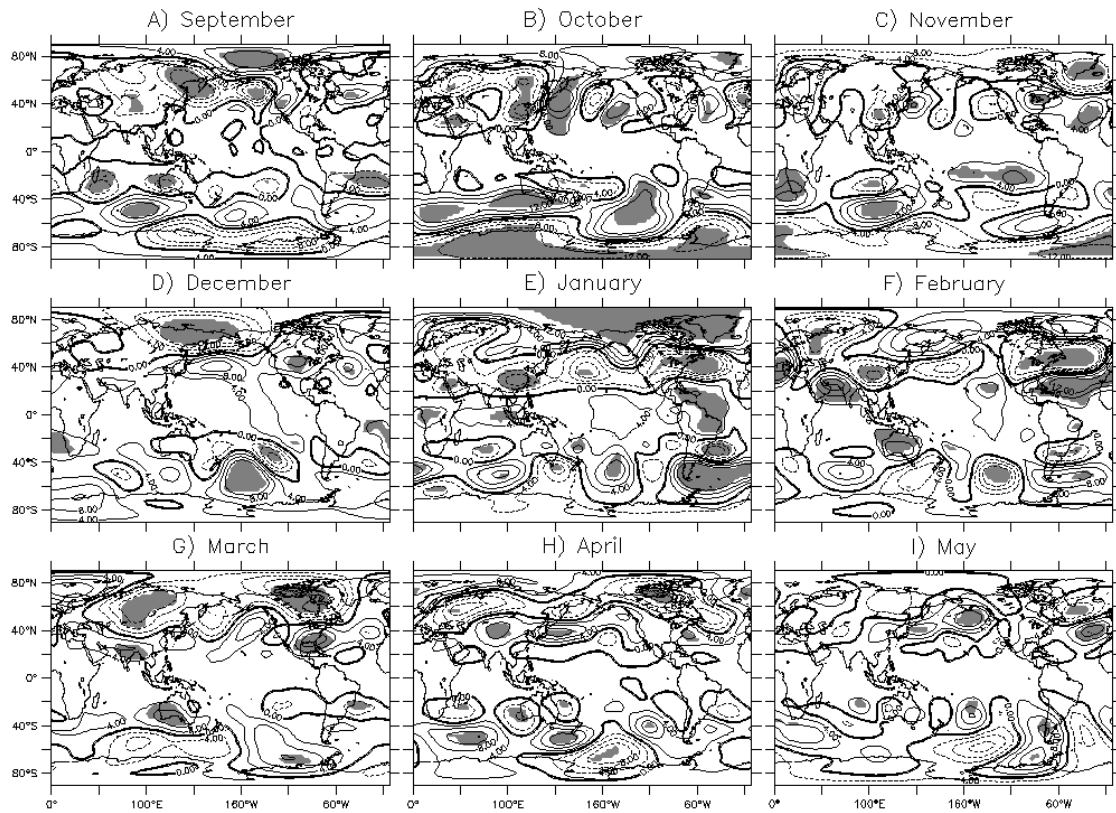


Figure 4.3: Regression maps of monthly 200mb geopotential height anomalies onto the Jan-Feb EBPI time series. Contour interval is 4m and solid and dashed contours represent positive and negative values respectively. Gray shaded areas show regions where the correlation between geopotential height anomaly and EBPI is significant at the 90% test level.

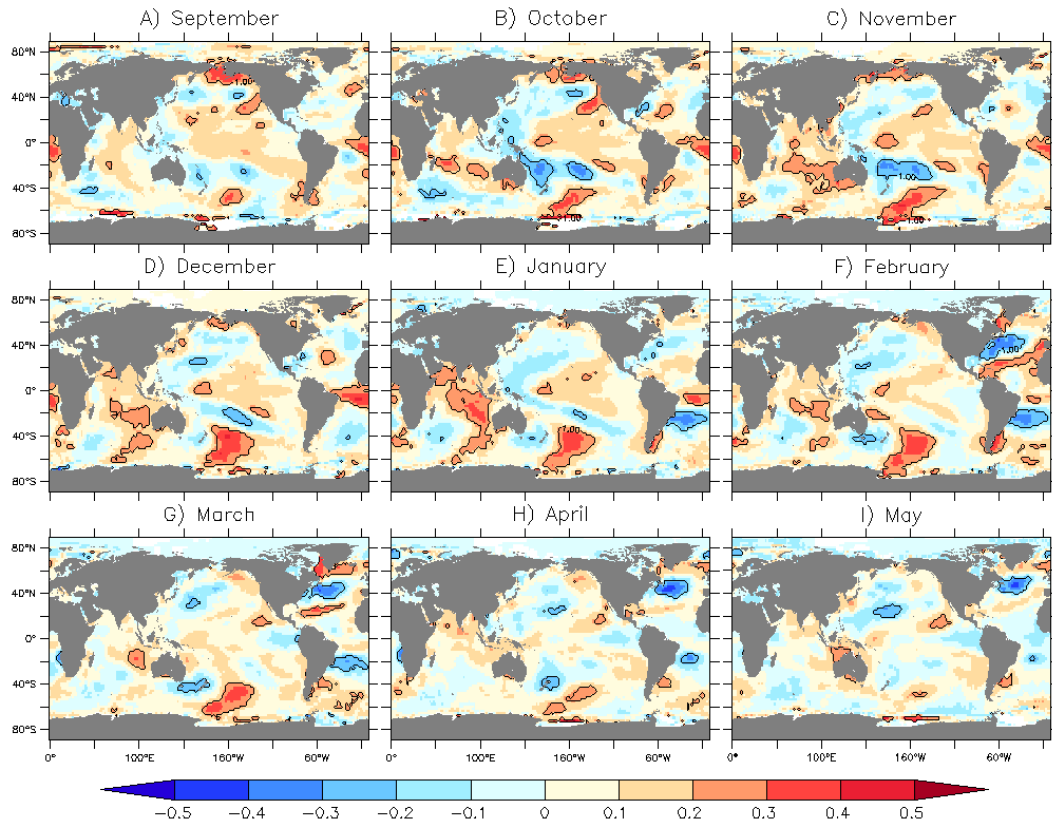


Figure 4.4: Map of SST correlations to EBPI precipitation time series. Contoured areas show regions where the correlation between SST anomaly and EBPI is significant at the 90% test level.

centers centered at about 30S over SESA and 10S over Central Brazil respectively and that dominate the South American upper level circulation anomalies. At lower levels during January, the circulation over the region is dominated by the South Atlantic anticyclone and the SESA cyclonic circulation with the Central Brazil anticyclonic anomalies being replaced by strong northwesterly flow. Upper level circulation anomalies weaken during February but are still visible, while at lower levels little circulation anomaly remains during this month.

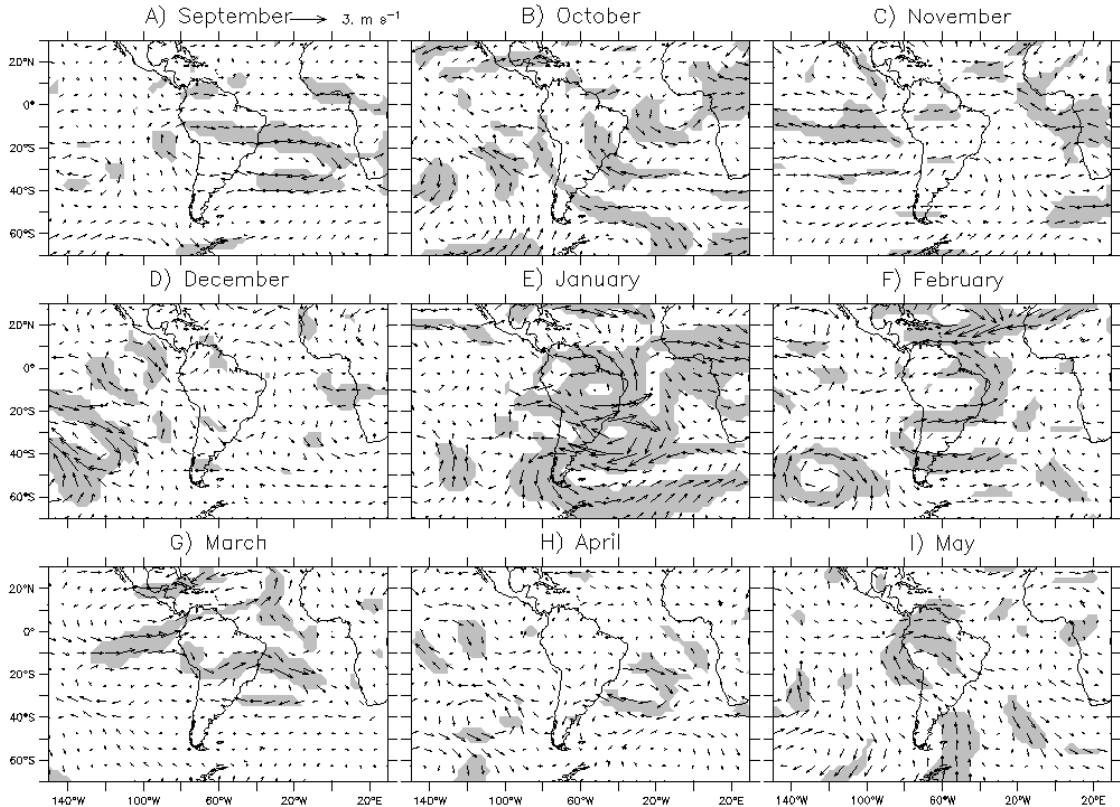


Figure 4.5: Regression of 200mb wind anomalies onto EBPI over the South American continent. Shaded areas show regions where the correlation EBPI and at least one of the wind component anomalies is significant at the 90% test level.

During the months leading up to January and February, we see little upper level anomalous winds associated with the Jan-Feb EBPI time series, the most notable being a cyclone anticyclone pair with centers at about 10S and 40S. The circulation anomalies during October are consistent with the upper level teleconnection observed during the same months in the 200mb anomaly maps discussed above. These upper level anomalies are not clearly

present during the following November and December months making it difficult to form a causal link between them and the circulation, and hence precipitation, anomalies during January and February. At lower levels, we see that from October to December, no clearly significant wind anomaly pattern precedes the Jan-Feb precipitation anomalies captured by the EBPI time series.

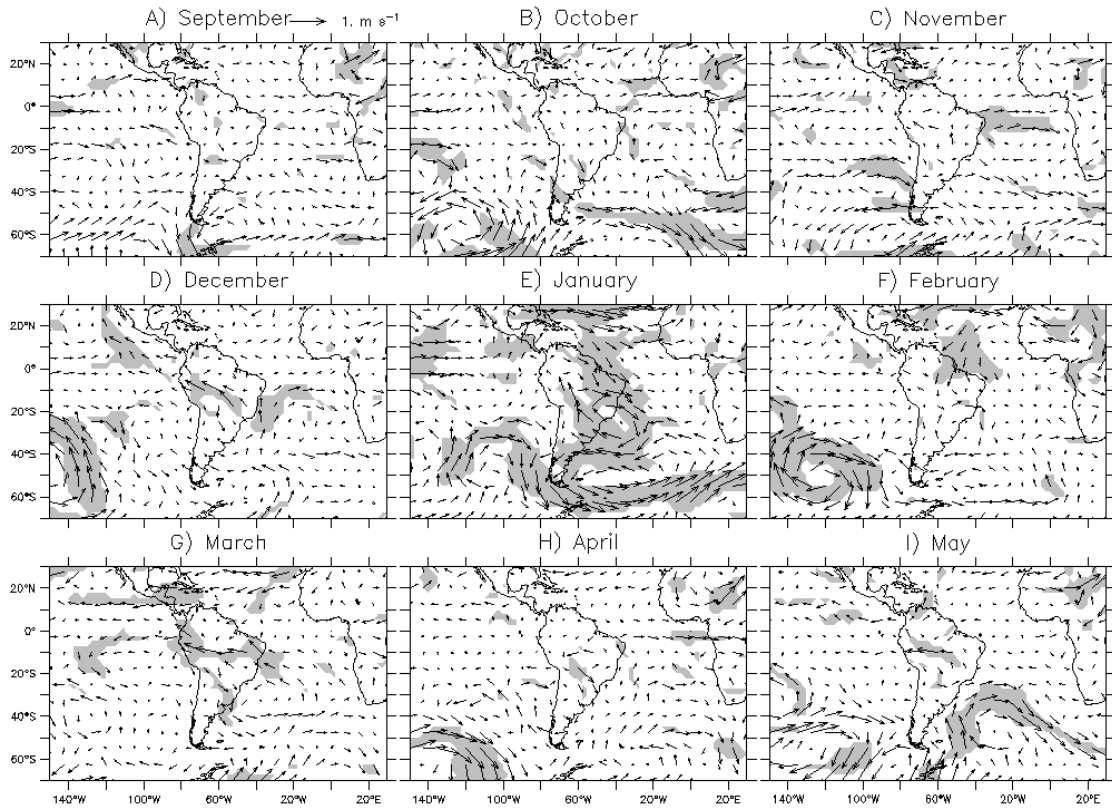


Figure 4.6: Same as in figure 4.6 but for 850mb winds anomalies.

As seen from these analyses the strong Eastern Brazil precipitation variability captured by the first EFO DJF mode and the second S-EOF mode develops even more rapidly than suggested by the second S-EOF mode, with sharply different precipitation and circulation patterns associated with the EBPI precipitation anomalies during the preceding October-November-December and January-February.

To focus on the December to January transition, figure 4.7 shows the regression of 925mb wind and specific humidity anomalies to the EBPI for the months of December, January

and February. During the month of December, we see high anomalous humidity over the region where we see anomalous positive SSTs as one would expect over warm ocean water. These humidity anomalies disappear during January and are again present, throughout a larger area, during February.

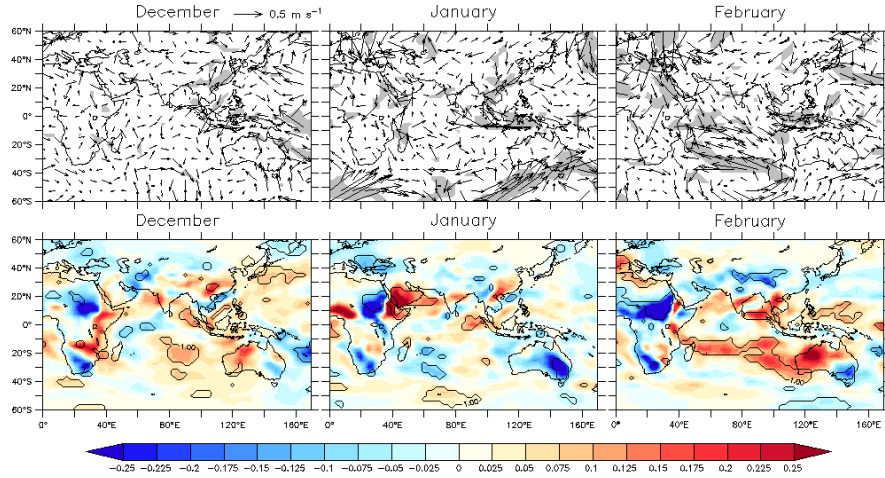


Figure 4.7: 925mb winds (upper panels) and specific humidity (lower panels) regressed onto the EBPI time series for the months of December, January and February. Grey areas in the wind anomaly maps represent areas where the correlation between the EBPI time series and at least one of the wind components is significant at the 90% test level. Specific humidity is in units of grams per kilogram and contours represent areas where the correlation between EBPI and specific humidity anomalies is significant at the 90% test level.

For the anomalous winds at 925mb, we see no significant precursory anomalous wind signature during the month of December and still no anomalous winds during January, where precipitation over the western Indian Ocean is most strongly linked to South American precipitation. The only anomalous winds over the region associated with the South American precipitation anomalies appear during February, a month after South American precipitation anomalies and their Indian Ocean counterparts are established. This may be a sign that the monthly progression of the mean fields of precipitation and low level convergence may be the trigger mechanism behind the observed Indian Ocean-South America teleconnection.

4.1.2 Mean state change over the Indian Ocean From December to January.

The rapid development of precipitation anomalies over the Indian Ocean associated with Jan-Feb EBPI anomalies and the subsequent wavelike pattern of teleconnection that links the Indian Ocean region to South America shown in the previous section, may be suggestive that a rapid change in the climatological conditions over the Indian Ocean from December to January may be the source of this mode of variability and it's strong coupling to the months of January and February. To explore this hypothesis we present a series of mean state difference maps of different atmospheric variables.

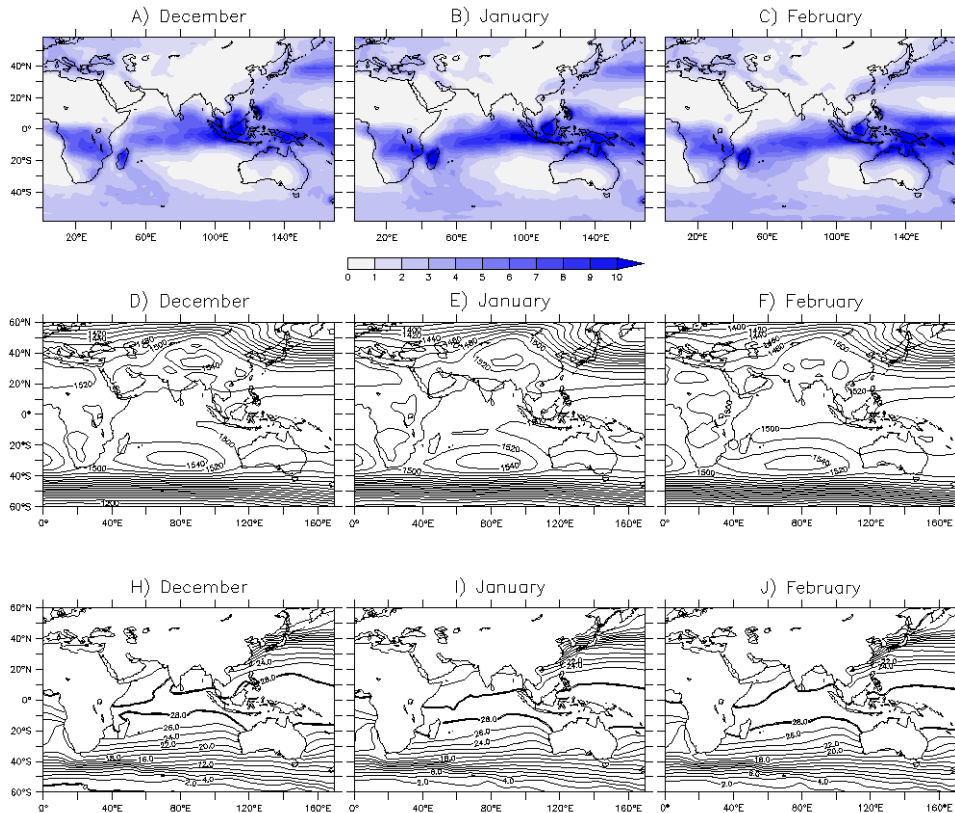


Figure 4.8: December, January and February monthly mean fields of GPCP precipitation from 1979-2010 (top three panels), 850mb geopotential heights from NCEP reanalysis (Mid three panels) and ERSST sea surface temperatures (bottom three panels). Precipitation is in units of mm/day, geopotential heights in units of meters with contour intervals every 20 meters and SST in Celsius with contour intervals every two Celsius.

Figure 4.8 shows the monthly mean maps of precipitation (from GPCP data 1979-2010), 850mb geopotential heights and SST for the months of December, January and February. Precipitation over the eastern Indian Ocean is plentiful from September to May (as shown by figure B.2), but from December to January we observe a rapid westward extension of the low level trough from the eastern Indian Ocean towards Madagascar (mid panels in figure 4.8) and strong development of convection over the region from 50E to 80E (region associated with Eastern Brazil precipitation anomalies). This development is also accompanied by strong warming of the underlying SSTs in the region.

To make more evident this shift in mean state from December to January, figure 4.9 shows difference maps of precipitation, 850mb geopotential heights and 925mb specific humidity and convergence, with the difference defined as the January mean state minus the December mean state. We see that precipitation over the western Indian Ocean increases from December to January by about 2mm/day accompanied by falling pressure over the region. We also see a strong rise in specific humidity and wind convergence at the 925mb level in the western Indian Ocean off the coast of Madagascar. This strong low level moisture convergence in the western Indian Ocean serves as the driver for the rapid development of convection in the region. This strong precipitation may serve to produce the observed teleconnection pattern between the western Indian Ocean and South America that is linked to the Eastern Brazil precipitation anomalies. This climatological moisture convergence may be enhanced by the transport of anomalous low level moisture seen during December (4.7) by the monthly mean convergence. The December low level moisture anomalies are likely transported by the mean January flow to enhance the precipitation over the western Indian Ocean and thus depleted during January. As the convection in the western Pacific intensifies, local anomalous winds appear during February and re-establish moisture anomalies over the region as shown in figure 4.7 for February wind and specific humidity anomalies over the Indian Ocean.

We also observe an intensification of the upper level jet at 200mb from December to January. Figure 4.10 shows the January 200mb geopotential Hgt anomalies regressed onto

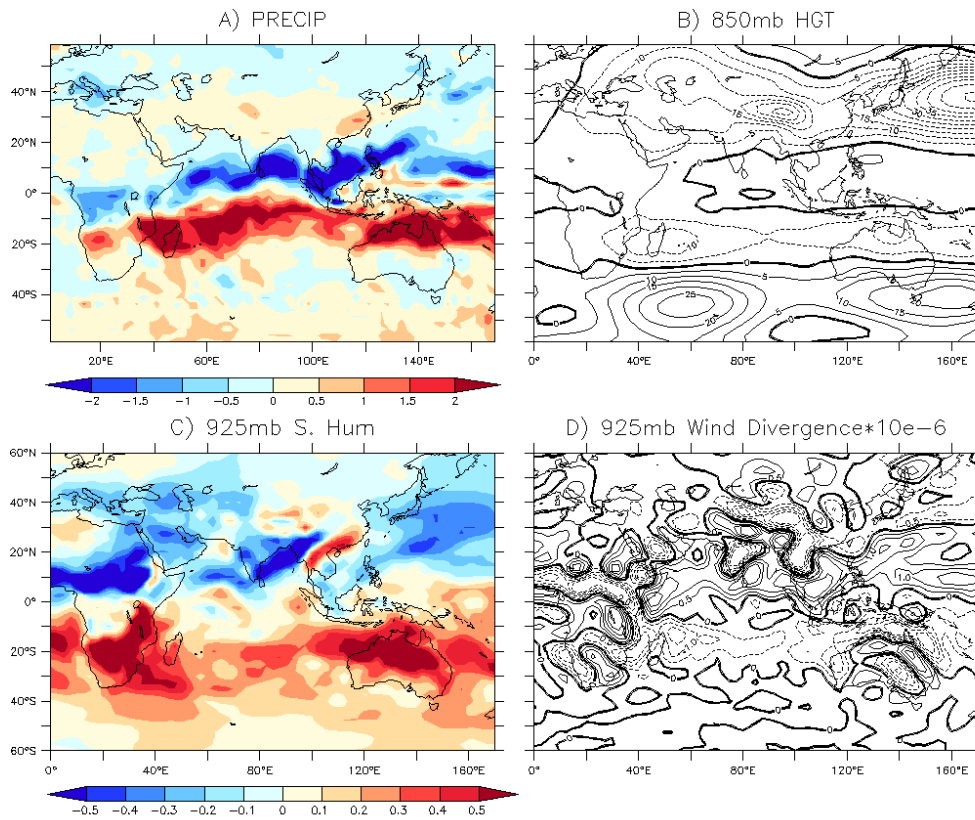


Figure 4.9: Spatial maps of January mean state minus December mean state for precipitation (units of mm/day), 850mb height (units of meters with contour intervals every 5 meters), 925mb specific humidity (in units of grams/kilogram) and 925mb wind divergence (in units of $10^{-6} s^{-1}$)

the EBPI time series (same as for the January panel of figure 4.3) superimposed to the 200mb zonal wind change from December to January (Jan mean state minus Dec mean state). Over the southern hemisphere we observe that the upper level westerlies intensify from December to January located at about 45 South and from 100 East to about 140 West. This is the region where we see strong anomalous wave activity linking the Indian Ocean to South America.

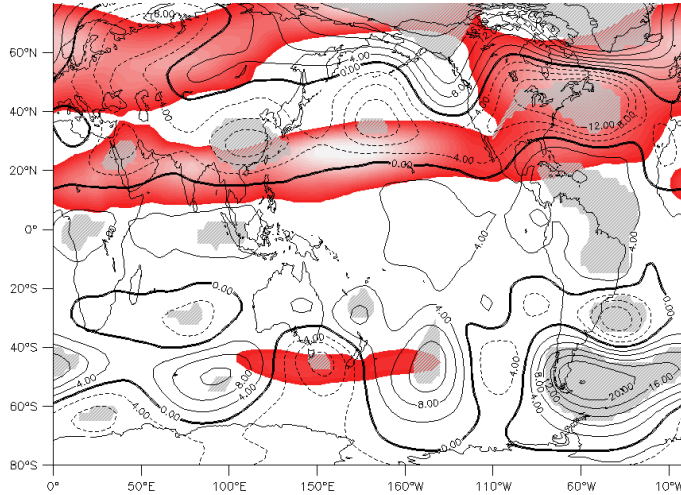


Figure 4.10: EBPI regressed to 200mb anomalies (contours) and January-December 200mb zonal wind (red shading). Gray hashing regions shows regions where the correlation between EBPI and 200mb geopotential height anomalies are significant at the 90% test level.

These results lead us to propose that western Indian Ocean precipitation anomalies play an important role in the life cycle of precipitation anomalies over Eastern Brazil as captured by the EBPI anomaly time series. The mechanism proposed is as follows; SST anomalies over the Indian Ocean during the months leading up to January-February generate low level moisture anomalies over the region that, advected by the mean flow, generate anomalous precipitation in the western Indian Ocean that serve to excite anomalous Rossby wave activity that reaching South America generates anomalous upper level circulation that in turn generates precipitation anomalies over eastern Brazil. The reason why eastern Brazil precipitation anomalies become established rapidly from December to January even when Indian Ocean SST anomalies are already present during the previous September may be due

to the rapid development from December to January of the western portion of the Indian Ocean ITCZ off the coast of Madagascar. This rapid set up of seasonal precipitation in that region makes it so that precipitation anomalies in the region can then generate the type of teleconnection pattern observed in the regressed fields of 200mb geopotential heights and are carried eastward by an intensified upper level jet towards South America.

4.1.3 Eastern Brazil Precipitation Index analysis of GPCP.

Because of the observed link to Indian Ocean precipitation observed from the regression analysis using the EBPI index, we will explore the possibility that Indian Ocean precipitation anomalies have a causal relationship with the precipitation anomalies over South America captured by the EBPI time series. We carry out this analysis for two main reasons. The first is that if we wish to establish a causal link between Indian Ocean precipitation anomalies and South American precipitation anomalies we will need to make use of pentad precipitation data to calculate lead and lagged regressions with higher temporal resolution that may permit us to observe the development of precipitation over the Indian Ocean, the establishment of the teleconnection pattern and consequently the development of South American precipitation anomalies. The second is that the previous analysis used as precipitation anomaly data over the oceans for the period 1948-2011 NOAA's Precipitation Reconstruction (PREC) dataset (Chen et al. (2002)), which for oceanic precipitation anomalies uses a reconstruction method based on the EOFs of satellite estimates of oceanic precipitation from 1979-present to reconstruct the precipitation anomalies over oceans for the years the data is not available. For this reason, the observed link between the Indian Ocean and South American precipitation observed in the previous section may be misleading and must be corroborated by using a non-reconstructed precipitation dataset with coverage over the oceans.

Figure 4.11 shows the regression of monthly GPCP precipitation anomalies onto the EBPI time series calculated from GPCP data for the period spanning 1980-2010. The patterns of precipitation over South America associated with the January-February EBPI

index are in good agreement with those observed for PREC/L data. GPCP precipitation data shows the same type of link between eastern South American precipitation with enhanced rainfall in both areas during January and February and suppressed rainfall during December and March. This link is nonetheless much weaker than observed for the analysis done using PREC and PREC/L data implying this link may be at least partially an artefact of the dataset.

Over South America, where GPCP rainfall estimates are heavily weighted by rain gauge observations we see that rainfall anomalies of the opposite sign to those of Jan-Feb are visible, but only during December and are not present during November and September. In fact, it appears from this analysis that, apart from small precipitation anomalies over the SPCZ and over the western tropical Pacific during December, the precipitation anomalies over eastern Brazil during January and February are not linked to preceding precipitation anomalies over any remote region, this becomes even more obvious when looking at correlation maps of EBPI to global precipitation as shown in figure C.1. The strongest remote precipitation anomalies associated with the Jan-Feb EBPI time series are over the Indian Ocean during February and over the western Pacific during March.

Correlations maps of GPCP EBPI to SST anomalies (fig C.3) show no significant SST anomalies over the Indian Ocean during January and February and weak anomalies during the preceding November and December and no significant SST anomalies are seen for this mode from September to January over the equatorial Pacific ocean. Over the south Pacific, the same persistent warm SST anomalies associated with this mode both in the REPC/L EBPI analysis and in EOF analysis are present. Atlantic SST anomalies associated with this mode have the same interesting behaviour as seen in the PREC/L analysis with positive SST anomalies over the tropical Atlantic during September to December leading EBPI precipitation anomalies and strong negative anomalies over the subtropical South Atlantic centred around 25S from January to May for contemporary and lagging months. Regression maps of GPCP EBPI to 200mb geopotential height (figure C.2) show a remarkably similar wave pattern during January as for the PREC/L analysis including the zonal teleconnection

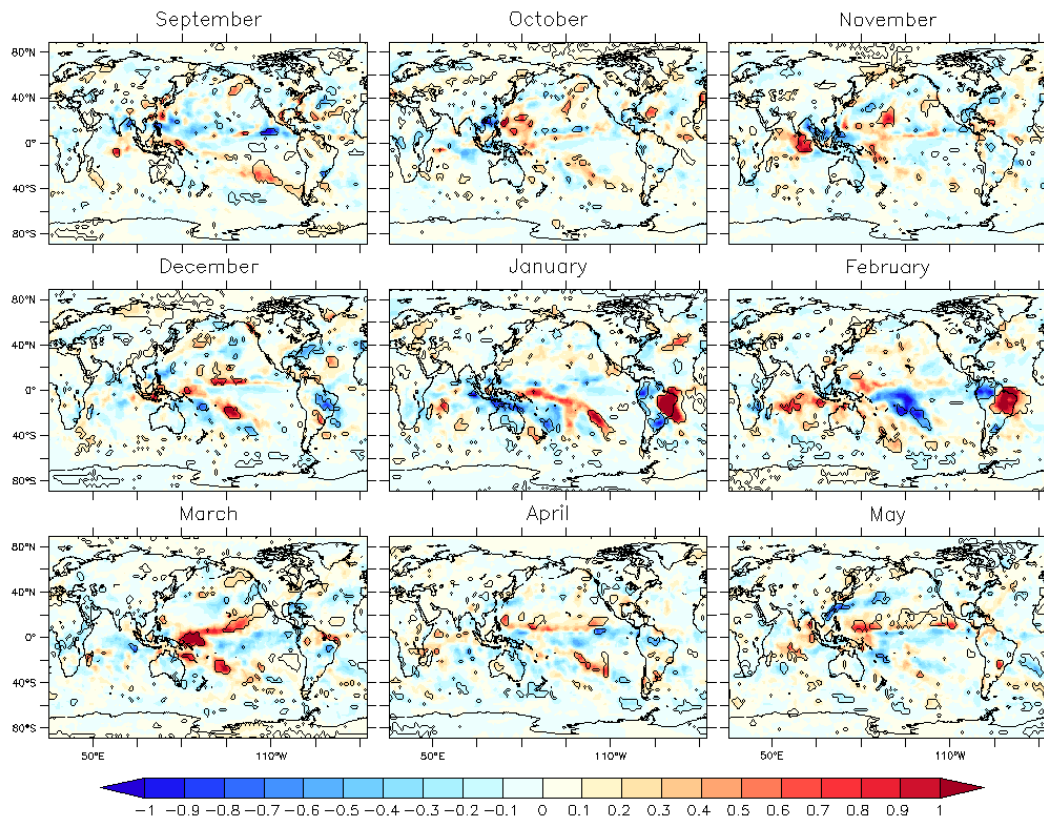


Figure 4.11: Regression maps of monthly GPCP precipitation anomalies onto the Jan-Feb EBPI time series calculated from GPCP data for the period 1980-2010. Red colors are positive anomalies and blue colors are negative anomalies in units of mm/day. Black contours outline regions where the correlation between precipitation anomaly and EBPI is significant at the 90% test level.

pattern observed over the Atlantic but this pattern does not persist during February as it does for the PREC/L EBPI analysis. During the preceding October we do not see the same strong PSA1 type pattern as seen for PREC/L data.

To perform the lead lag analysis for the GPCP pentad data we first calculate the correlation between the JanFeb EBPI to each individual pentad of the year, starting from pentad 36 (mid June) of the previous year (lagging pentads) to pentad 35 of the following years (leading pentads). This is done to maintain the Southern Hemisphere rainy season intact contiguous in the middle of the year. These correlation values are shown in figure 4.12.

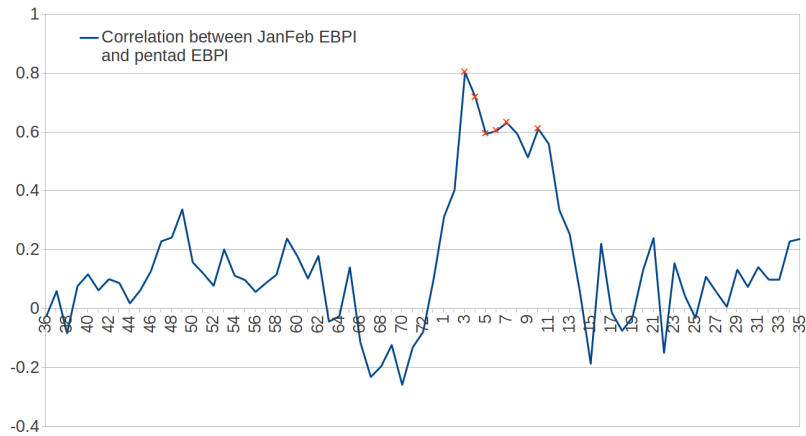


Figure 4.12: Correlations of the JanFeb. EBPI index to individual pentads. Points marked with orange Xs show pentads for when the correlation between JanFeb EBPI and the EBPI for that individual pentad is significant at the 95% test level.

As we can see, the precipitation variability captured by the EBPI index is most faithfully represented by the precipitation of pentads 3 through 7, or the days between January 16 and February 9. The EBPI time series calculated using the mean precipitation anomalies in the Eastern Brazil region defined in figure 4.1 shows a correlation of 0.67 to the January February EBPI time of GPCP data. Using this pentad time series we calculate the regression onto individual pentad precipitation anomalies shown in figure 4.13. The numbers in parenthesis in figure 4.13 represent the time shift of the pentad with respect to the EBPI time series, hence panel D represents the regression of the EBPI index to pentad 2 and

panel B the regression to pentad 73 of the previous year. Likewise for lead regressions, panel J represents the regression of the EBPI time series for pentads 3 to 7 to pentad 8 precipitation anomalies.

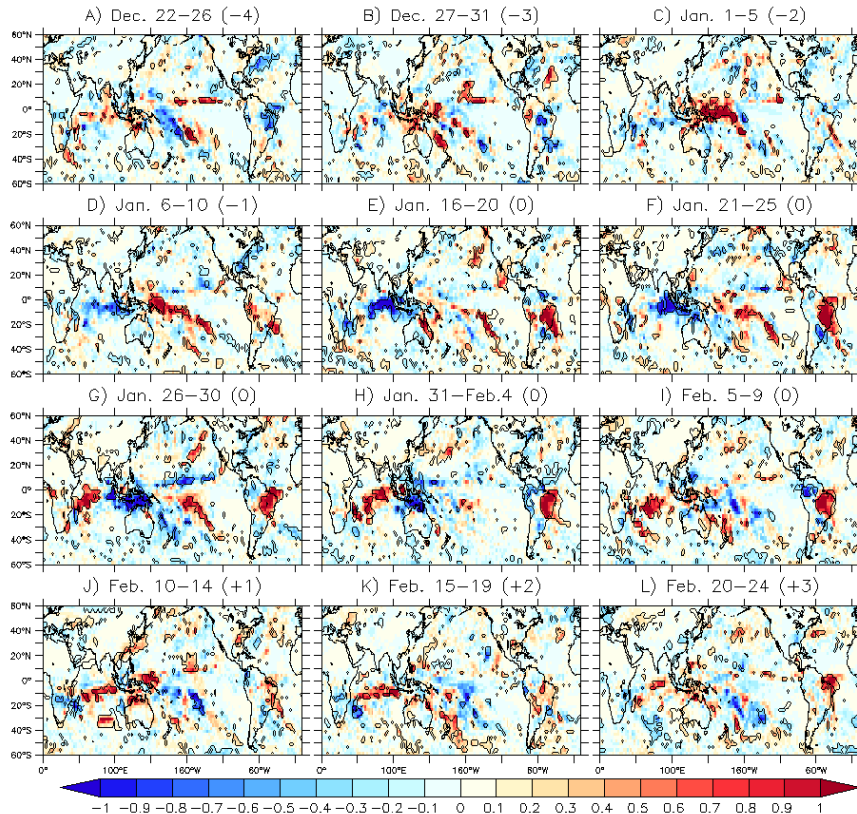


Figure 4.13: Regression maps of GPCP pentad anomalies to the EBPI calculated from GPCP for the pentads spanning from Jan 16 to Feb 9 (pentads 3 to 7 of the year). The numbers in parenthesis represent the lead of lag of the pentads with respect to the EBPI time series, see text for details. Contours indicate areas where correlations between the EBPI and the pentad precipitation anomalies are significant at the 90% test level.

From figure 4.13 the development of the strong precipitation anomalies over Eastern Brazil is lead by negative anomalies over the region during lags -4 and -3 which then develop into positive anomalies over the SACZ for lags -2 and -1. These SACZ anomalies the greatly intensity over the continental land mass and extend northward. As the precipitation anomalies associated with this mode evolve, they loose intensity over the SACZ and become predominant over the continent (panels G, H and I of figure 4.13).

On a pentad time scale over the Indian Ocean, no significant precipitation leads EBPI

precipitation anomalies up to a lag of 4 pentads and remote precipitation anomalies leading up to EBPI precipitation anomalies are only seen over the western tropical Pacific. Precipitation anomalies over the Indian Ocean appear two pentads after the precipitation anomalies over Eastern Brazil have been established (figure 4.13 panel G) and linger until three pentads after pentad 7, Feb. 5-9, which is the last pentad incorporated to the EBPI index (figure 4.13 panels J, K and L). Negative precipitation anomalies over the Maritime Continent are observed for pentads 3-7, Jan 16 to Feb 4, contemporary with the Eastern Brazil anomalies.

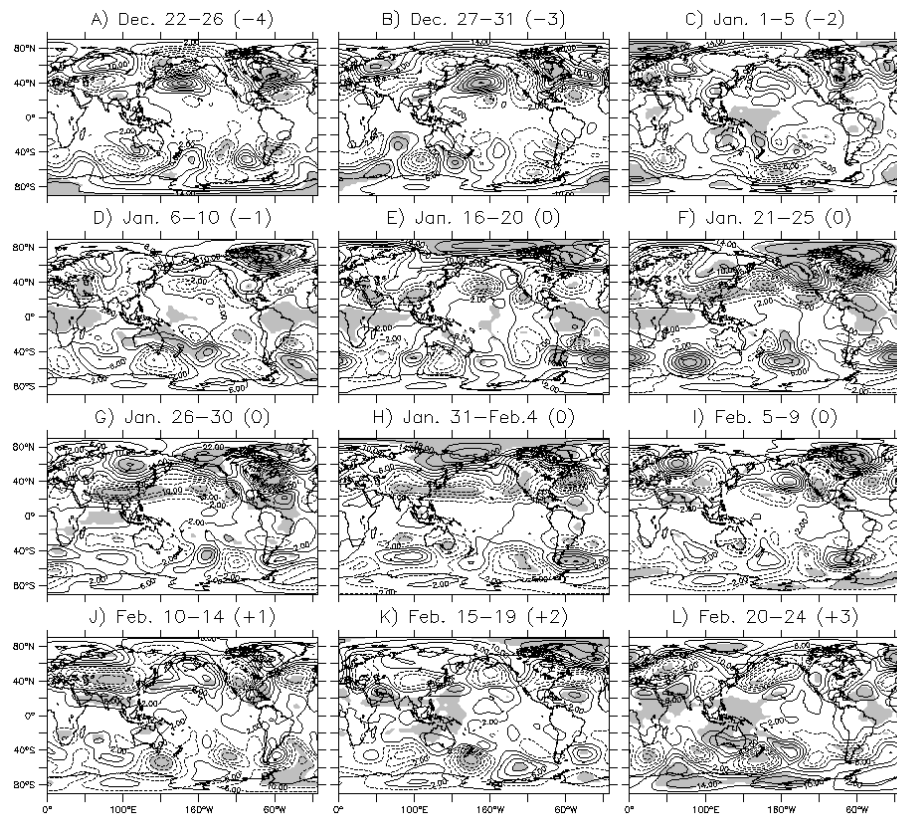


Figure 4.14: Regression maps of NCEP 200mb geopotential height pentad anomalies to the EBPI calculated from GPCP for the pentads spanning from Jan 16 to Feb 9 (pentads 3 to 7 of the year). The numbers in parenthesis represent the lead of lag of the pentads with respect to the EBPI time series, see text for details. Shading indicate areas where correlations between the EBPI and the pentad precipitation anomalies are significant at the 90% test level.

Figure 4.14 shows NCEP 200mb geopotential height pentad anomalies regressed onto

our pentad EBPI index. For pentads leading by -4 and -3 (panels A and B) we observe anomalous wave activity emanating from the SPCZ (lag -4) and the tropical western Pacific (lag -3) that produce anomalous upper level anticyclonic circulation anomalies over South America that likely generate as a response the negative precipitation anomalies seen over Eastern and central Brazil during these same pentads (figure 4.13 panels A and B). During lag -2, when leading precipitation anomalies are the strongest over the Pacific, no clear teleconnection pattern to the Pacific is seen, but strong upper level cyclonic circulation is seen over South America. This upper level cyclone intensifies during lag -1 aided by anomalous Rossby wave activity originating from the SPCZ (coinciding with precipitation anomalies over the SPCZ 4.13 panel D) and remain during pentads 3-7, sometimes remaining independent from large scale patterns (panels E and F) and sometimes becoming embedded into large scale wave patterns (panels G, H and I). These upper level cyclonic anomalies are similar to what Zamboni et al. (2011) describe as the Vortex Over South America, VOSA, that was discussed in section 1.3.2. The origin of this mode of upper level circulation is still not well understood but it's link to Eastern Brazil precipitation anomalies is clear.

The same type of analysis was done using only pentad 3, Jan. 16-20 to calculate the EBPI time series and results from such analysis (shown in figure C.4) show good agreement in terms of the spatial patterns of precipitation with precipitation anomalies over the western Pacific leading South American precipitation and anomalies over the Indian Ocean lagging it. The spatial patterns captured in the analysis using the EBPI of pentad 3 show less intense remote precipitation anomaly patterns.

From this analysis it seems clear that Indian Ocean precipitation anomalies are not causally related, as suggested in the previous section and that in fact, Indian Ocean precipitation anomalies appear after precipitation anomalies over South America have been established. The relationship between the precipitation anomalies in both regions is nonetheless clear and may become a topic of future study.

There is a revealing result from this analysis and it is the fact that the upper level vortex over South America that has been a the upper level circulation signature of the

strong precipitation anomalies over eastern Brazil and of the DJF continental tripole mode does in fact lead the establishment of precipitation anomalies over eastern Brazil by two pentads. We can see from figure 4.14 panel for lag -2 (Jan. 1-5) that the upper level cyclone centred over SESA at about 30S is already clearly visible albeit with correlations that are not yet significant. During the Jan 1-5 pentad this upper level circulation mode appears independently from any remotely forced teleconnection mode. During the lag -1 (Jan.6-10) pentad, this upper level circulation intensifies likely aided by transient wave activity and remains the dominant upper level circulation anomaly over the region until our fifth contemporary pentad, pentad 6 (Jan.31-Feb.4) when it is no longer present over South America and subsequently precipitation anomalies over Eastern Brazil begin to die down. This sequential evolution is even more clear for the EBPI regression analysis for pentad 3 only presented in figure C.4.

4.2 Summary

In this section we proposed a simple method for the analysis of Eastern Brazil precipitation anomalies by defining the Eastern Brazil precipitation index as the Area averaged anomaly over the region from the Equator to 20S and between 55 and 30 west. The DJF EBPI time series was shown to capture with good fidelity the temporal variability of the DJF continental tripole mode and furthermore it was shown that this mode was dominated by precipitation over Eastern Brazil during January and February, hence, the reference time series here used was the EBPI time series for January-February averaged anomalies.

Regression analysis of EBPI to precipitation for the 1949-2010 period in using PREC/L data (4.2) reveal that over South America during Jan-Feb the spatial pattern of precipitation anomalies over the continent related to eastern Brazil precipitation is in good agreement with the spatial pattern of the DJF continental tripole mode, showing that this mode is robust and that this analysis is capable of representing it in both temporal and spatial terms. Over SESA, precipitation anomalies of opposite sign are seen during the preceding months of October, November and December while opposite anomalies over eastern Brazil

to those seen in JanFeb are only present for the preceding December.

In terms of global precipitation (global precipitation anomalies from the PREC/Ocean dataset where used) precipitation anomalies over the western Pacific are present during October and November and contemporaneous precipitation anomalies over the Indian Ocean are seen for January and February. This apparent link to Indian Ocean precipitation anomalies was proposed as a possible trigger mechanism for the precipitation anomalies over South America. SST correlation maps show significant SST anomalies associated with this mode over the central Pacific and Indian Ocean as well as over the Atlantic in areas underlying the SACZ. 200mb geopotential height anomalies also suggest that this mode bears some link to Indian Ocean precipitation with a clear teleconnection pattern extending over the South Pacific from the Indian towards South America during the month of January. Regression of 1948-2010 EBPI to 200mb winds shows a strong upper level circulation formed by a cyclonic vortex over South East South America (30 South) and an anticyclonic vortex over the equatorial part of the continent (10 South). At low levels we see the clear surface signature of the upper level cyclone over SESA during January but no clear reversal of low level circulation from September, October, November and December to January as we would expect if the mechanism proposed by Grimm were dominant in this transition.

EBPI analysis for GPCP data shows similar precipitation anomalies during January and February but precipitation anomalies of the opposite sign of those in SESA and eastern Brazil only during December with little significant precipitation anomalies over the South American continent seen for the September, October, November months. This supports the results seen in the S-EOF analysis that during this period the DJF continental tripole mode was not preceded by precipitation anomalies of the opposite sign. In fact, for this period, remote precipitation anomalies linked to this mode are very weak in general with only small areas of significantly correlated precipitation anomalies seen for December over the SPCZ. The contemporaneous relationship to Indian Ocean precipitations is also seen in GPCP data albeit weaker than for the previous results. SST anomalies associated with the GPCP EBPI time series for the period 1979-2010 show almost no SST anomalies over the

equatorial Pacific while over the Indian Ocean, weaker SST anomalies are observed for this period compared to the 1948-2010 period.

Using pentad anomalies of GPCP precipitation and NCEP reanalysis 200mb geopotential height and effort was made to understand the succession of events that leads to the development of the strong Eastern Brazil precipitation mode. We conducted analysis using an EBPI time series calculated for the pentads of January and February which most faithfully represented the variability of the JanFeb EBPI time series. Pentads 3 to 7 all showed correlations of the bimonthly EBPI significant at the 99% test level, for a total of 5 pentads spanning the days Jan 16 to Feb 9. Analysis was performed as well for the single pentad with the highest correlation to the Jan-Feb EBPI time series which was pentad 3 for the days Jan.16-20. Both of these pentad analyses show that precipitation over the Indian Ocean does not lead precipitation over South America and in fact, it lags South American precipitation by 2 pentads. This pentad analysis did reveal that the upper level vortex over South America is established two pentads before the strong JanFeb precipitation anomalies. The relationship between the upper level vortex and precipitation anomalies over eastern Brazil has been established before but clear evidence as to which is the cause and which is the effect is elusive. Here we have a clue that suggest that the upper level circulation anomalies over SESA are antecedent and maybe causally linked to eastern Brazil precipitation anomalies. The origins of this upper level vortex however remain a mystery.

CHAPTER 5

THE SEASONAL EVOLUTION OF PRECIPITATION VARIABILITY AS CAPTURED BY A MULTI-MODEL ENSEMBLE OF COUPLED OCEAN ATMOSPHERE MODELS.

Here we will examine the performance of the Multi Model Ensemble (MME) seasonal forecast of models participating in the DEMETER project.

Figure 5.1 shows maps of correlation skill of the MME seasonal forecast for the period 1982-2005 with respect to GPCP precipitation data for the same period. The MME seasonal forecast has good skill over the tropical Pacific and Atlantic oceans (weakest during SON over the Atlantic) for all seasons, over South America on the other hand, the model skill is heavily dependant on both region and season. During SON we observe significant MME forecast skill over the northern parts of the continent, areas of eastern Brazil and extending south to south eastern Brazil stopping at about 30S and not reaching SESA. During DJF, we observe a large section of central South America, from about 5S to about 25S where the MME shows very poor forecast skill, with positive skill over the continent over the northern parts and over SESA just north of the mouth of the La Plata river. During DJF the MME has poor skill over the region where the Eastern Brazil Precipitation Index used in the previous chapter was defined. During the MAM season, the MME shows good forecast skill over the Eastern Brazil region and South East Brazil (20-30 South), but again negative skill over SESA.

The first three S-EOF modes of PREC/L precipitation and seasonal MME forecast for the period from 1960 to 2005 are shown in figure 5.2. The first three modes of PREC/L precipitation data are in good agreement with those shown in chapter 3, with only minor differences in the spatial patterns represented for each mode. The first mode of observations captures the progression of the meridional dipole of precipitation associated with ENSO. The second S-EOF mode captures the evolution from the SESA-SACZ dipole pattern during SON to the continental tripole pattern during DJF and then again to the dipole pattern

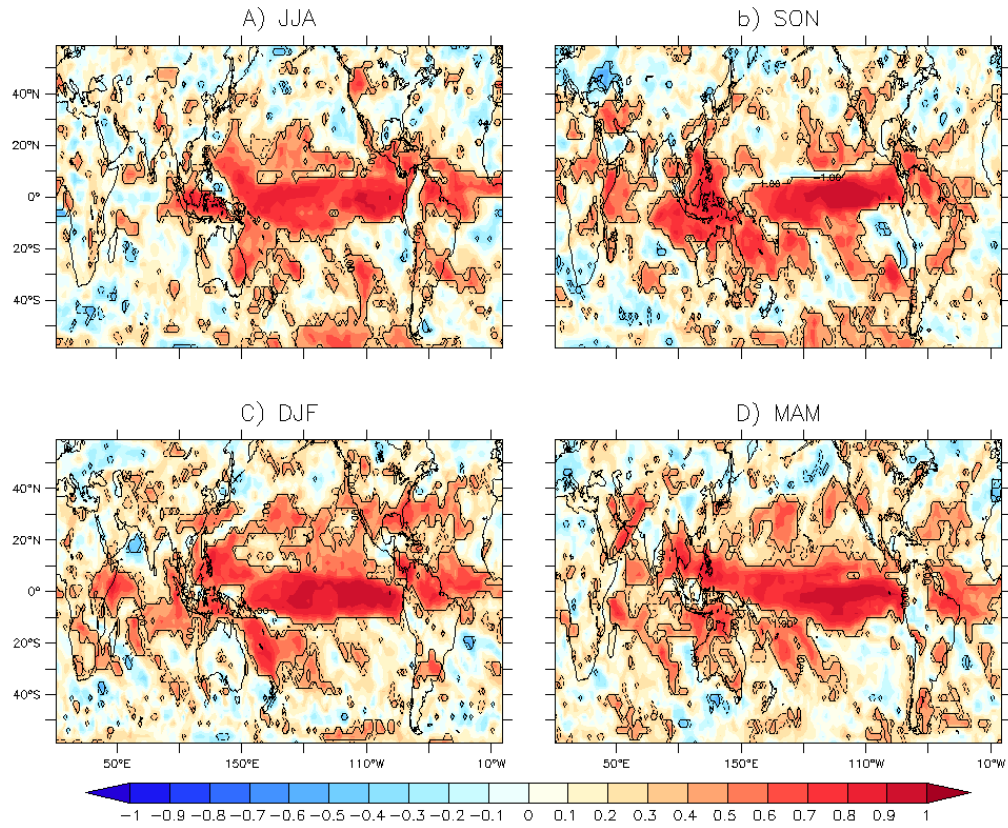


Figure 5.1: Correlation skill maps of MME seasonal precipitation forecast for the period 1982-2005 as compared to GPCP precipitation data for the same period. Dashed contours represent areas of 90% significance while solid contours represent areas of 95% significance.

during MAM. The third S-EOF mode of observations captures the northwest to southeast banded structure of precipitation during DJF and MAM as the third mode for PREC/L precipitation for the complete period 1948-2011. All the S-EOF modes of observations for the period 1960-2005 explain a % of variance equal to their equivalents in the complete period 1948-2011.

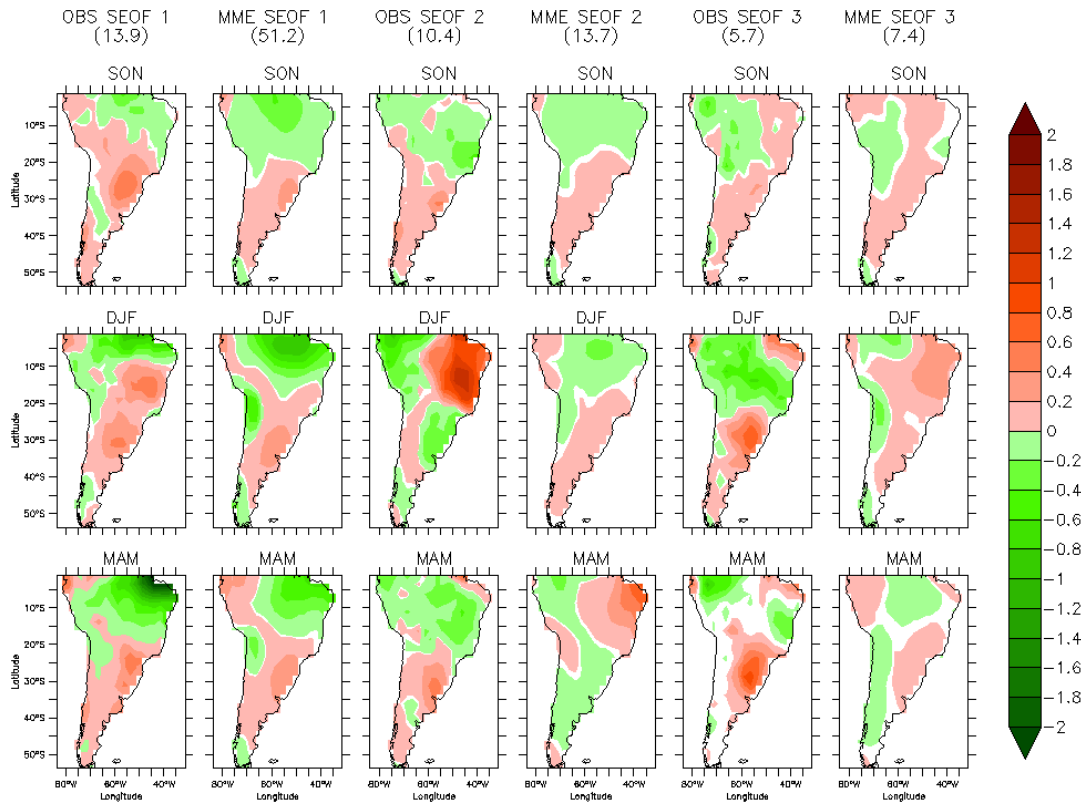


Figure 5.2: Eigenvector maps of the first three S-EOF modes of PREC/L precipitation and MME seasonal forecast for the period spanning 1960-2005. The Eigenvectors here have been multiplied by the standard deviation of their corresponding PC so that the shading represents the amount of loading contributed to a particular mode by a particular grid point in a particular season. Areas with values between -0.01 and 0.01 have been made white to facilitate differentiation between negative and positive areas.

The MME seasonal forecast shown a strong first S-EOF mode that accounts for 51.2% of the observed variability in the dataset that quite faithfully captures the seasonal evolution of the ENSO variability over the South American region captured by the S-EOF 1 of observations being most accurate during MAM. This mode captures in the model the

		MME		
		S-EOF 1	S-EOF 2	S-EOF 3
Observations	S-EOF 1	0.75*	0.35	0.13
	S-EOF 2	0.08	0.19	0.68*
	S-EOF 3	0.15	0.41*	0.21

Table 5.1: Correlation table between the first three S-EOF modes of observations and MME seasonal forecast. Correlations values with an asterisk are significant at the 90% test level.

southward migration of the ITCZ and its modulation by the phase of ENSO. During DJF the MME extends negative anomalies associated with this mode too far south so that the MME fails to capture the second positive maximum centred around 15S that characterizes this mode in observations. During MAM this mode reproduces rainfall variability over the region quite faithfully so that the known predictability of the Nordeste region during this season can be perhaps extended to a broader area of the continent.

It appears that the MME seasonal forecast is unable to capture the strong continental tripole pattern. The third S-EOF of MME precipitation shows positive anomalies over eastern Brazil and negative anomalies to the Northwest but no negative anomalies over SESA during DJF. The second S-EOF of MME precipitation shows during MAM positive anomalies over eastern Brazil and negative anomalies to the Northwest and over SESA, but a season after this pattern of anomalies appears in observations.

Table 5.1 shows the correlation values between the PC time series of the first three S-EOFs of observations and MME seasonal forecast. The strong correlation between the second S-EOF mode of observations and the third S-EOF mode of MME forecast suggest that this may be the mode that captures the DJF continental tripole mode in the MME. If that is the case, the SON part of the third S-EOF of MME does show some weak negative anomalies over the SACZ region, giving some signal that the seasonal evolution of this mode is at least in part captured by the MME simulations.

Figure 5.3 shows correlation maps of MME S-EOFs 1, 2 and 3 to MME SST anomalies. The SST patterns that accompany this mode in the MME are in good agreement with the SST patterns associated with this mode in observations (shown in figure 3.9 panels A, D

and G), specially over the Pacific and Indian Ocean. Over the Atlantic Ocean, the MME reproduces similar SST anomalies during SON to those seen in observations, but during DJF the equatorial SST anomalies over the Atlantic associated with this mode are not captured by the MME. During MAM, the MME reproduces the strong positive SST anomalies seen in observation over the tropical North Atlantic but fails to reproduce the accompanying negative SST anomalies to the south. This may somewhat reduce the performance of the MME forecast to capture the final position of the ITCZ over the equatorial Atlantic and the Nordeste region, which is sensitive to this cross equatorial SST gradient. The 200 mb wind fields generated by the MME for this mode (figure 5.4) show good agreement with the general seasonal evolution of the effect of ENSO over South America (3.12). During SON there is a strong tropical extratropical teleconnection type of response while during DJF and MAM the strongest effect is seen over the equatorial belt.

The second S-EOF mode of the MME shows the weakest coupling to SST anomalies on all the MME S-EOF modes here studied. During SON we see positive SST anomalies over the tropical eastern Pacific and negative to the west. Over the south Pacific, we observe a zonal dipole of SST anomalies similar to those observed during the same season for S-EOF 1 but shifted east. During SON this mode has little Atlantic SST signature. During DJF, SST anomalies for this mode weaken over the Pacific, with the subtropical Atlantic ocean showing a meridional SST pattern centred around 30S. During MAM SST anomalies over the southern Pacific have disappeared for this mode while cold SST anomalies intensified over the western and central Pacific. Over the Atlantic we see strong SST anomalies forming a tripole pattern with strong positive anomalies south of the Equator reaching about 30S and weaker but still very significant cold SST anomalies to the north over the tropical North Atlantic and the South over the subtropical South Atlantic.

The third S-EOF mode of the MME seasonal forecast shows, during SON and DJF widespread SST anomalies over the Pacific ocean in a pattern reminiscent of ENSO but much weaker in intensity than the SST associated with the first S-EOF mode of the MME. These Pacific SST anomalies weaken during the MAM season. Over the Atlantic, positive

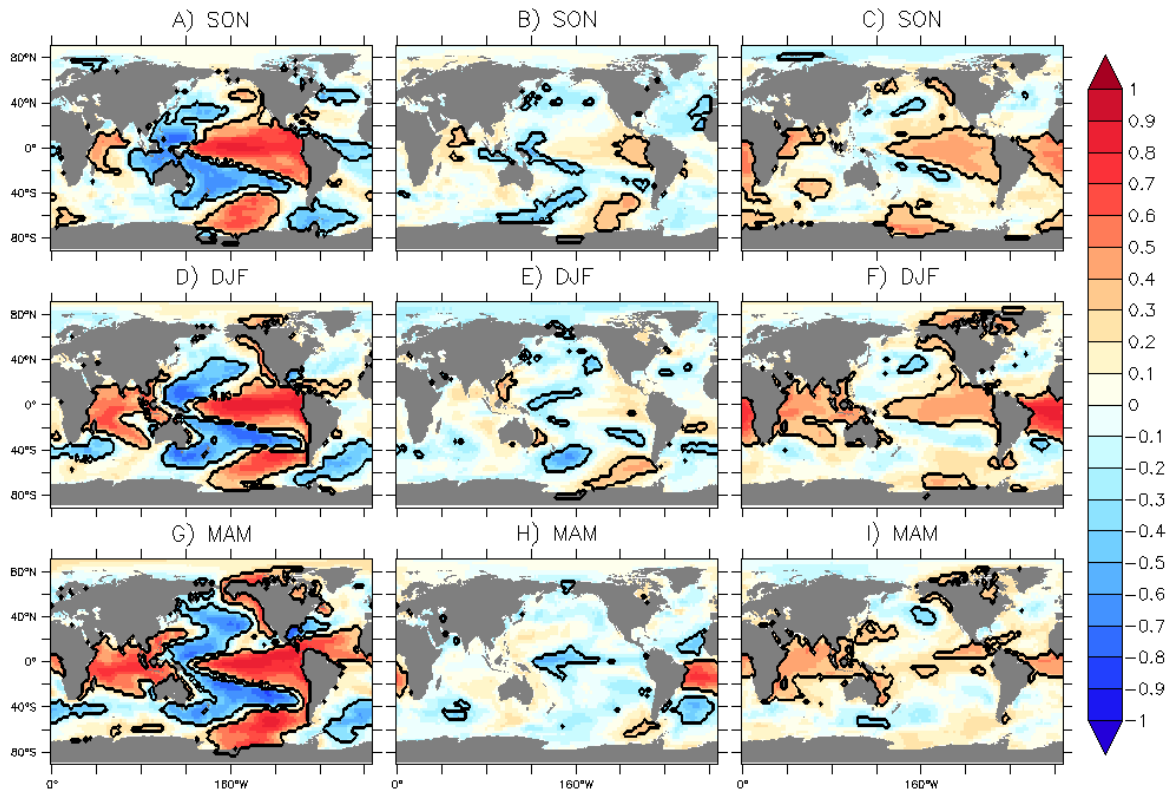


Figure 5.3: Correlation maps of the PC time series of the first three MME seasonal forecast S-EOF modes to MME SST anomalies. Contours denote areas where correlations are significant at the 95% test level.

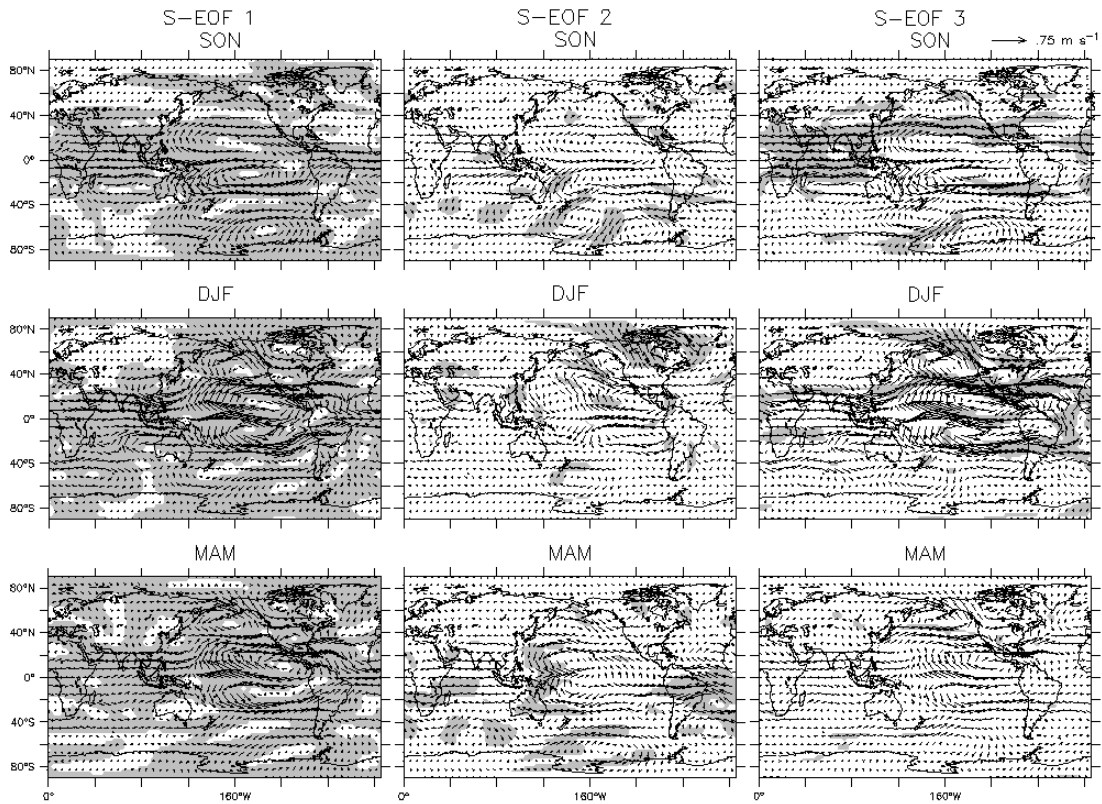


Figure 5.4: Regression maps of the PC time series of the first three MME seasonal forecast S-EOF modes to MME 200mb wind anomalies. Shading denote areas where correlations are significant at the 99% test level for the S-EOF 1 panels and the 90% test level for the S-EOF2 and S-EOF 3 panels.

SST anomalies are observed for this mode during all the seasons, with their largest intensity during the DJF season when they are accompanied by negative SST anomalies off the coast off Brazil to the south.

It is interesting to see that both S-EOF modes that show strong precipitation variability over eastern Brazil (MME S-EOF 2 during MAM and S-EOF 3 during DJF) are accompanied during that same season by strong equatorial and subtropical South Atlantic SST anomalies. It is possible that these Atlantic SST anomalies play a role in the origin of the strong precipitation anomalies over Eastern Brazil and are not just responding to the atmospheric forcing produced by the SACZ. Unfortunately, the MME does not produce upper level vortex anomalies for these modes (MAM panel for S-EOF 2 and DJF panel for S-EOF 3 in figure ??) that are similar to the upper level vortex associated with precipitation anomalies over eastern Brazil.

5.1 Summary

This chapter was dedicated to the comparison of the S-EOF modes of variability in observations to the S-EOF modes captured by a MME of seasonal forecasts performed by coupled ocean-atmosphere GCMs.

We see that the MME has good correlation skill for all seasons over the Nordeste and equatorial regions of the South American continent. Over the rest of the continent, the MME forecast skill is highly dependent on the season with JJA showing good skill over the SACZ, DJF showing good MME skill over SESA and the transitions seasons (SON and MAM) showing good skill over larger portions of the eastern parts of the continent and the SACZ.

The first S-EOF of the MME seasonal forecast reproduces the seasonal evolution of the meridional dipole mode of precipitation over South America with good accuracy in terms of spatial distribution of anomalies and temporal variability. The intensity of anomalies associated with this mode in the MME does show some error with dry anomalies over the tropical parts of the continent overestimated and wet anomalies over SESA underestimated.

The MME mode that most resembles the DJF continental tripole mode is the MME S-EOF 3. The PC of the MME S-EOF 3 has a correlation value of 0.68 to the PC of observations S-EOF 2 (continental tripole mode). The MME S-EOF 3 shows positive anomalies over eastern Brazil and negative anomalies over the western tropics over South America. Negative anomalies over SESA are not reproduced. This mode is associated during DJF with strong positive SST anomalies over the equatorial Atlantic and weak negative anomalies to the south. In general the SST pattern associated with the MME S-EOF 3 is more similar to the S-EOF 3 of observations. In terms of upper level circulation, the MME S-EOF 3 shows anticyclonic anomalies centred over eastern Brazil (about 5S) but does not capture the vortex SESA to the south.

From these results we see that not only the cyclonic vortex over SESA is important for the complete formation of the DJF continental tripole mode, but its anticyclonic counterpart to the north is also necessary to generate the widespread positive precipitation anomalies over eastern Brazil that characterize this mode.

CHAPTER 6

CONCLUSION

The objective of this study was to perform an in depth analysis of South American interannual precipitation variability during DJF season with the purpose of establishing the robustness of the previously reported dominant modes of variability of the DJF season over South America. This analysis was extended to the seasonal evolution of the modes of South American precipitation variability in an effort to gather evidence as to what is the source of the major observed mode of DJF variability.

The dominant DJF mode of precipitation variability is characterized by strong anomalies over central and eastern Brazil and anomalies of the opposite sign over south east South America (SESA) and the western tropical areas of South America. This mode has been denominated the continental tripole mode of variability and appears as the EOF 1 mode in PREC/L data for the period 1948-2010 and sub period 1979-2010, and GPCP and CMAP data for the period 1979-2010 and is well separated in all cases, making it a robust feature of the DJF precipitation variability over South America. This mode has been observed before by Paegle and Mo (2002) as the fourth DJF rotated EOF mode and by Grimm and Zilli (2009) as the first mode of DJF variability. This precipitation mode has been strongly linked to an upper level vortex centred over SESA that appears to be the cause of the precipitation anomalies (Zamboni et al. (2009) Zamboni et al. (2011)). Nonetheless, the origins of this precipitation mode or its accompanying upper level circulation are still not well understood. This mode shows no significant correlations to SST anomalies with the exception of modest SST anomalies over the subtropical Atlantic Ocean that have been proposed to be mostly a response of the local SSTs to the atmospheric forcing (Doyle and Barros (2002)) but that have been shown to play an important role via feedbacks in the realistic modelling of the SACZ (Misra (2008)). The second DJF EOF mode captures the meridional dipole between the Nordeste and tropical continental areas to the north and the SACZ and SESA to the south. This second DJF EOF mode is clearly linked to ENSO SST

anomalies.

For SON, the leading mode of variability is characterized by what we have labelled the SESA-SACZ dipole mode due to its characteristic spatial pattern of precipitation anomalies. It is present in all datasets analysis and appears as well separated in all analysis with the exception of the PREC/L EOF analysis for the period 1948-2010. The SESA-SACZ dipole mode is correlated to ENSO type SST anomalies for the PREC/L 1948-2010 EOF analysis. In GPCP and CMAP analysis, this mode is related to central Pacific warming type of SST anomalies. The second SON EOF mode is a meridional dipole type mode and is related to SST anomalies over the eastern Pacific Ocean. We observe that these two SON modes are better separated for the analysis done for the 1979-2010 period than in those analysis where the complete 1948-2010 period is used.

The leading MAM mode is a meridional dipole type mode with strong anomalies over the Nordeste region and opposite anomalies over SESA. This leading MAM mode is clearly produced by ENSO and is well separated from all other modes.

A proposed mechanism for the generation of the leading DJF mode has been proposed in terms surface atmosphere interactions by Grimm (2003) and Grimm and Zilli (2009). It is based on the observed negative correlation between precipitation anomalies over central eastern Brazil from September, October November to December, January and February. This mechanism is described in detail in the introduction but in terms of EOF analysis it implies that the dominant EOF mode of SON, which represents a dipole of precipitation anomalies between SESA and the SACZ is significantly correlated to the leading DJF EOF continental tripole mode so that anomalies over SESA and eastern Brazil appear to invert from SON to DJF.

Using correlations between the PC time series of the corresponding EOF modes we find, for the PREC/L data over the 1948-2010 period, the SON SESA-SACZ dipole mode is weakly correlated to the DJF continental tripole mode, with a correlation value of 0.21, significant at the 80% test level. Furthermore, for GPCP, CMAP and PREC/L data for the period 1979-2010 the SON SESA-SACZ dipole mode and the DJF continental tripole

mode show no significant correlation to each other.

Using seasonal reliant EOF analysis of PREC/L precipitation for the seasons SON-DJF-MAM for the period 1948-2010 we are able to isolate in the first S-EOF mode most of the canonical ENSO generated variability over the South American domain. This S-EOF 1 mode captures the positive precipitation anomalies over SESA during SON (3.8 panel A) generated by ENSO over this region via tropical extratropical teleconnection to the central Pacific (3.12 panel A) as well as the strong suppression of convection over the Nordeste region of Brazil and tropical parts of the South American continent during DJF and MAM (3.8 panels D and G) mediated by strong anomalous walker circulation related to ENSO anomalies during DJF and MAM (3.12 panels D and F).

The second S-EOF mode for the 1948-2010 period captures the seasonal evolution of the DJF continental tripole pattern. During SON, this mode represents a SESA-SACZ dipole pattern with weakened positive anomalies over SESA compared to the SESA-SACZ dipole mode from standard EOF analysis of SON precipitation. This S-EOF mode shows weak, but significant, sst anomalies localized over the western Pacific during SON and DJF. Upper level circulation anomalies show little signal during SON. During DJF, the upper level vortex over South America associated with the DJF continental tripole mode is seen off the coast of SESA centred about 30S and embedded in an anomalous wavetrain that spans the Southern Pacific from Australia to South America.

To understand the origins of the differences between the SON SESA-SACZ dipole pattern and the DJF continental tripole pattern seen for analysis of the 1948-2010 period and for the 1979-2010 period we separated the PREC/L data into two epochs 1948-1979 and 1979-2010. These results are presented in section 3.3.1. For these two epochs, we see marked differences between the behaviour of the dominant modes of precipitation variability and specifically for the seasonal evolution of the DJF continental dipole mode. A striking difference between epoch is the strong degeneracy between the first two S-EOF modes of the 1948-1979 epoch which account for 13 and 12% of variance and forming an "effectively degenerate couplet" as put by North et al. (1982) while during the second epoch, the first

two S-EOF modes show clear separation between them. This makes the interpretation of the S-EOF modes of the 1948-1979 period difficult.

The DJF continental dipole mode appears as the first S-EOF mode for the 1948-1979 epoch and as the second S-EOF mode for the second epoch. During the first epoch, SON anomalies for this mode show the expected SESA-SACZ dipole of anomalies with reversed polarity for SESA and the SACZ from SON to DJF and an upper level vortex over South America that is embedded in the same type of South Pacific wave train as we saw for this mode in the the S-EOF analysis of the 1948-2010 period and that is only present for DJF. During the second epoch, the DJF continental tripole mode does not evolve from an opposite SESA-SACZ dipole during the previous SON, and in fact, anomalies over SESA and eastern Brazil have the same sign in both seasons. In terms of upper level circulation, we see that for the second epoch an upper level vortex is visible over South East South America for SON and DJF. During SON this upper level vortex is linked to anomalous wave activity over the South Pacific but during DJF the vortex appears disconnected to all visible upper level wave trains. From these results we see that the DJF continental tripole mode is always seen accompanied by the upper level vortex over South America regardless of what type of precipitation anomalies precede this mode during SON. We also see that the upper level vortex that characterizes the DJF continental tripole mode can be generated as a part of or independently from remotely remotely forced anomalous wave trains. These results agree with those found by Zamboni et al. (2011) in which they propose that this type of upper level vortex over South America can be both the product of remote forcing or local atmospheric variability.

As a way to study the variability of precipitation over Eastern Brazil, a regional precipitation index called the Eastern Brazil Precipitation Index (EBPI) was defined as the area averaged precipitation anomaly over the region from the equator to 20S and 55W to 30W and was used as the reference time series in regression and correlation analysis to global fields. The EBPI time series captures the temporal variability of the DJF continental tripole mode with good fidelity. It was found that the DJF continental tripole precipitation mode

is most highly correlated to the precipitation anomalies over Eastern Brazil for January and February, thus our choice of these two months to calculate the EBPI reference time series.

EBPI regression analysis for PREC/L and GPCP data show that precipitation anomalies over Eastern Brazil are highly correlated with opposite anomalies over SESA and western tropical South America, so this EBPI time series captures not only the temporal variability of precipitation over South America but the spatial pattern that characterized the DJF continental tripole mode. In PREC/L data for 1948-2010, anomalies over SESA are significantly correlated to anomalies of the opposite sign over the same region as far back as the preceding October while opposite anomalies to those over Eastern Brazil appear only during the previous December.

In this analysis we do see some evidence that fits the description of the mechanism behind the strong DJF precipitation anomalies over South America proposed by Grimm and co-authors in previous works (Grimm and Zilli (2009), Grimm (2011)). Precipitation anomalies over the western tropical Pacific during the preceding October and November months do show a significant relationship to South American rainfall during January and February. Furthermore, during October we see a clear teleconnection pattern between the western Pacific, originating over the correlated precipitation anomalies, and South America, that is able to influence the upper level circulation over the region. We also see how from October to December, precipitation anomalies of opposite sign to those seen during January and February become established and intensify.

On the other hand, we do not see any clear progression of the upper level circulation anomalies from October to January as well as no clear signal that the teleconnection pattern seen during October has any effect on lower level circulation (as seen from 850mb geopotential heights or 850mb winds). We also do not see any clear sign of the reversal of lower level circulation from October, November and December to January and February as the mechanism proposed by the authors would require. Furthermore, for GPCP data, anomalies of opposite sign over Eastern Brazil and SESA are only significant during the previous December and this dataset shows no clear signal of precipitation anomalies over the western

Pacific or their teleconnection towards South America.

Both PREC/L and GPCP EBPI analysis do show however, 200mb geopotential height anomalies associated with the EBPI time series show the clear presence of the upper level vortex over South America during January and February. Regression analysis of GPCP pentad data of the mean EBPI index for pentads 3-7 (Jan16-Feb9, pentads with correlation to JanFeb EBPI significant at the 99% test level) as well as for the EBPI index for pentad 3 (single pentad with strongest correlation to JanFeb EBPI) show that the precipitation anomalies over Eastern Brazil are lead by the establishment of the upper level vortex over South America by two pentads and that the establishment of this upper level circulation anomaly is not linked to any teleconnection pattern. This improves our previous understanding of the relationship between the upper level vortex and the January-February precipitation anomalies that form the continental tripole mode. Until now these two phenomena were understood as simultaneous whereas now, we have some evidence that points to the direction of the precipitation anomalies being generated by the upper level circulation mode and not the upper level circulation as a response to the January February precipitation anomalies.

We see that the MME has good correlation skill for all seasons over the Nordeste and equatorial regions of the South American continent. Over the rest of the continent, the MME forecast skill is highly dependent on the season with JJA showing good skill over the SACZ, DJF showing good MME skill over SESA and the transitions seasons (SON and MAM) showing good skill over larger portions of the eastern parts of the continent and the SACZ.

The first S-EOF of the MME seasonal forecast reproduces the seasonal evolution of the ENSO meridional dipole mode of precipitation over South America with good accuracy in terms of spatial distribution of anomalies and temporal variability but with some error in the intensity of the anomalies.

The MME mode that most resembles the DJF continental tripole mode is the MME S-EOF 3. The PC of the MME S-EOF 3 has a correlation value of 0.68 to the PC of obser-

vations S-EOF 2 (continental tripole mode). The MME S-EOF 3 shows positive anomalies over eastern Brazil and negative anomalies over the western tropics over South America. Negative anomalies over SESA are not reproduced. This mode is associated during DJF with strong positive SST anomalies over the equatorial Atlantic and weak negative anomalies to the south. In general the SST pattern associated with the MME S-EOF 3 is more similar to the S-EOF 3 of observations. In terms of upper level circulation, the MME S-EOF 3 shows anticyclonic anomalies centred over eastern Brazil (about 5S) but does not capture the vortex SESA to the south.

From these results we conjecture that not only the cyclonic vortex over SESA is important for the complete formation of the DJF continental tripole mode, but its anticyclonic counterpart to the north is also necessary to generate the widespread positive precipitation anomalies over eastern Brazil that characterize this mode.

In general these results highlight the complexity of the precipitation variability over South America and its seasonal evolution, with the leading mode of precipitation variability during peak wet season showing little direct dependence to SST anomalies which are the source of most climate predictability. It is clear that an integral understanding of the DJF continental tripole mode hinges heavily on an understanding of the upper level vortex over South America that accompanies it. An improved understanding of this circulation mode would likely greatly improve the predictability of the DJF tripole mode. The causes and origin of this upper level circulation are still an open question and deserving further and thorough study. The understanding of this mode of variability would likely benefit from high level modelling using coupled ocean-atmosphere-land surface models aimed at understanding the relative importance of each of the possible processes involved in the formation of the upper level circulation and the precipitation mode that accompanies it. An effort should also be made to understand the longer time scale variability shown by the DJF continental tripole mode as it could be an important modulation factor and a possible source of predictability for this mode on long time scales.

APPENDIX A
AUXILIARY FIGURES FOR THE S-EOF ANALYSIS OF
GPCP AND PREC/L DATA FOR THE PERIOD 1979-2010.

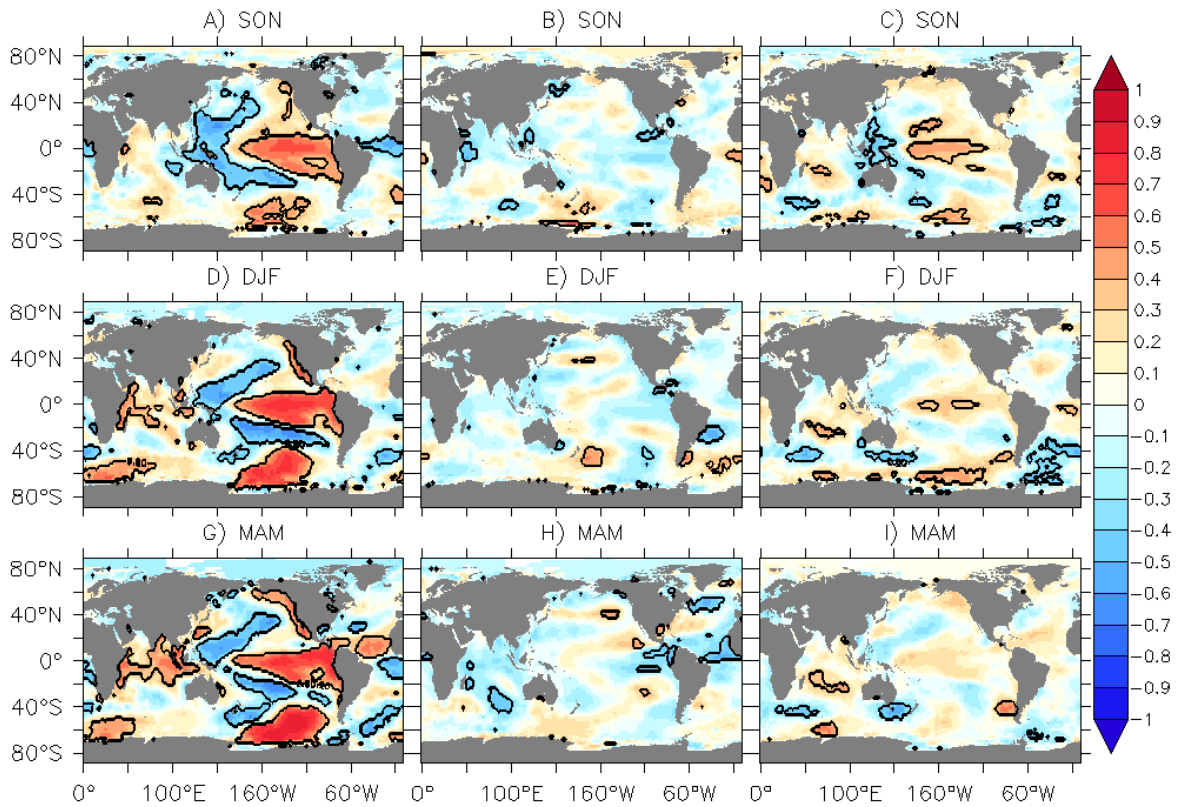


Figure A.1: Correlation maps of the first three S-EOF modes of GPCP data 1979-2010 to seasonal SST anomalies. Maps A, D and G represent the correlation of PC 1 to seasonal SST anomalies. Maps B, E and F represent the correlations for PC2 while C, F and I the correlations for PC3. Contours show areas where the correlations are significant at the 90% test level.

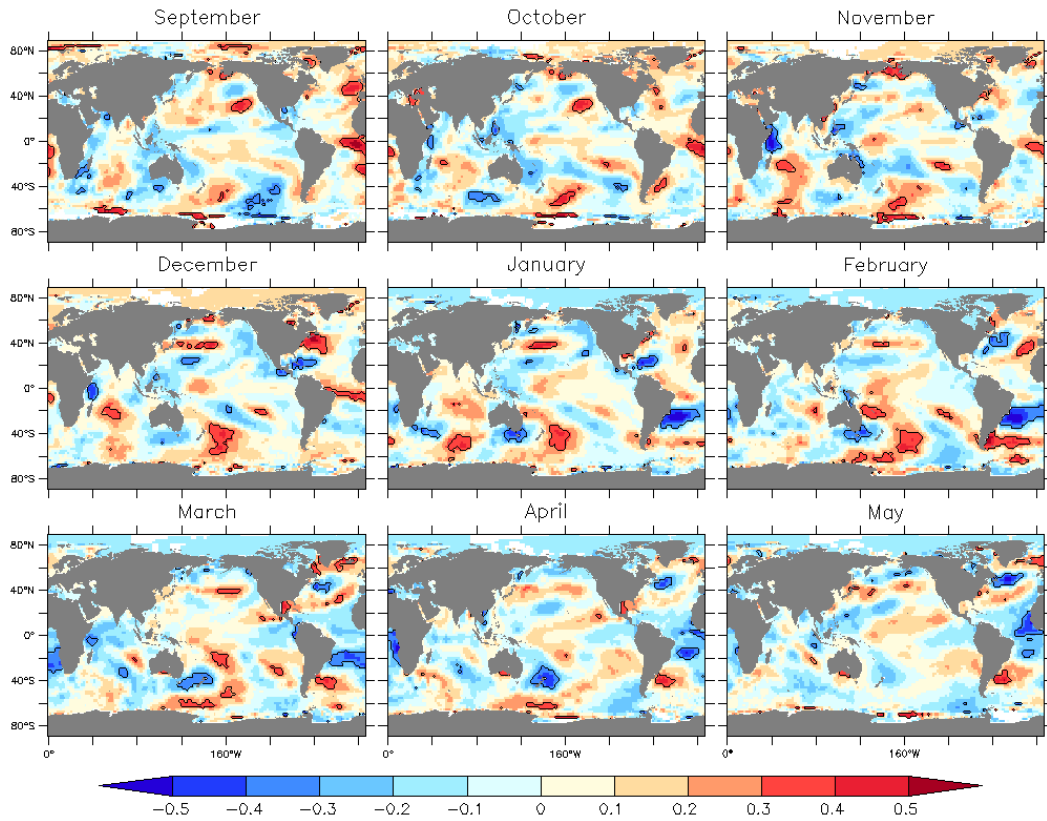


Figure A.2: Correlation maps of the first three S-EOF modes of PREC/L data 1979-2010 to seasonal SST anomalies. Maps A, D and G represent the correlation of PC 1 to seasonal SST anomalies. Maps B, E and F represent the correlations for PC2 while C, F and I the correlations for PC3. Contours show areas where the correlations are significant at the 90% test level.

APPENDIX B

AUXILIARY FIGURES FOR THE EASTERN BRAZIL PRECIPITATION INDEX ANALYSIS

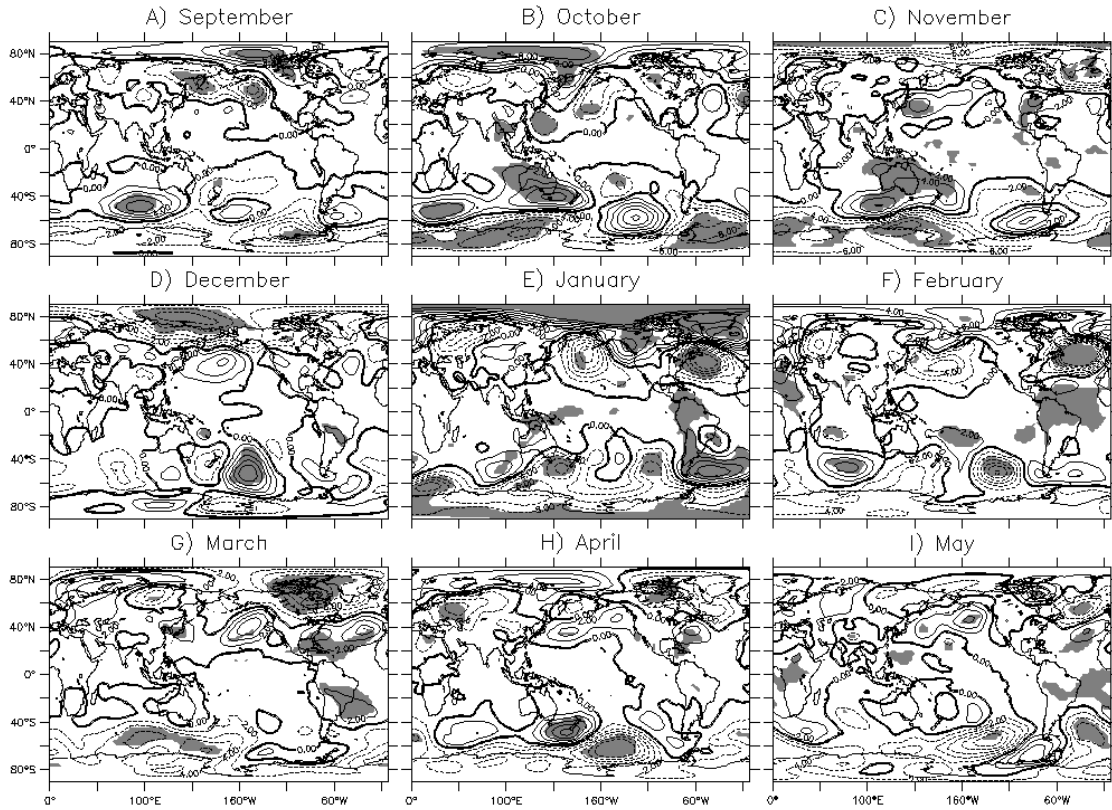


Figure B.1: Regression maps of monthly 850mb geopotential height anomalies onto the Jan-Feb EBPI time series. Contour interval is 4m and solid and dashed contours represent positive and negative values respectively. Gray shaded areas show regions where the correlation between geopotential height anomaly and EBPI is significant at the 90% test level.

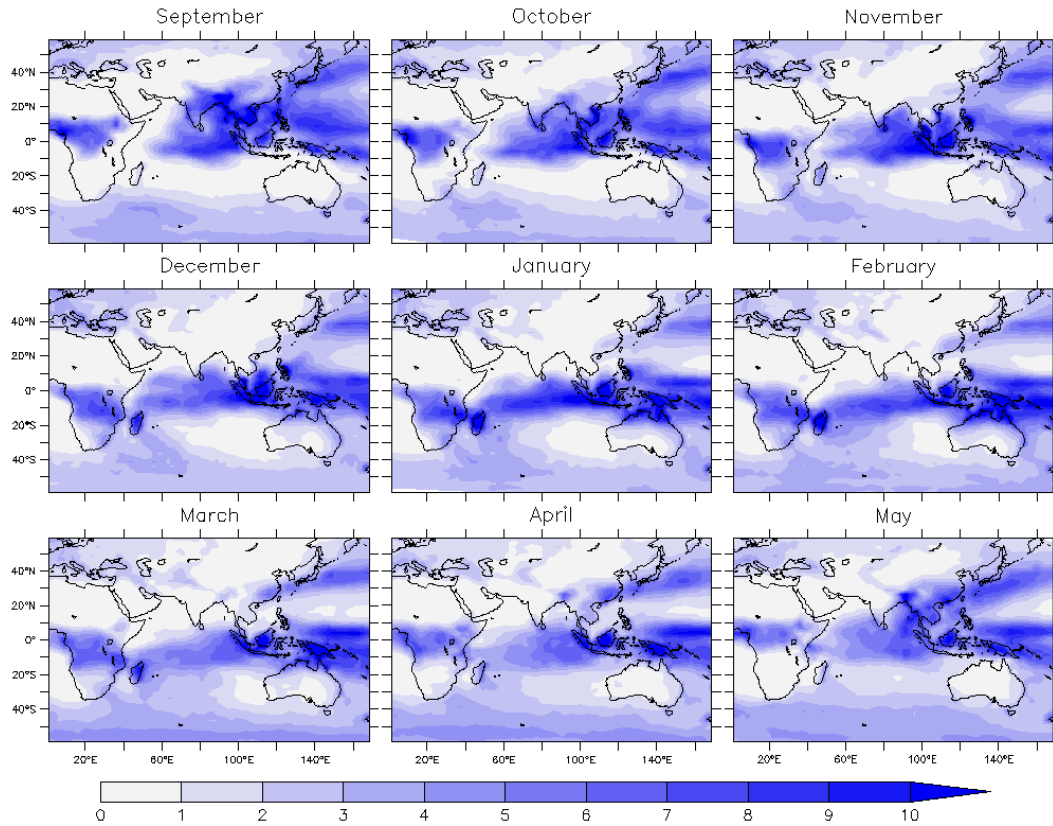


Figure B.2: Monthly mean precipitation maps over the Indian Ocean for the months of September through May from GPCP precipitation data 1979-2010. Precipitation in units of mm/day.

APPENDIX C

AUXILIARY FIGURES FROM CHAPTER 4, SECTION 4.1.3

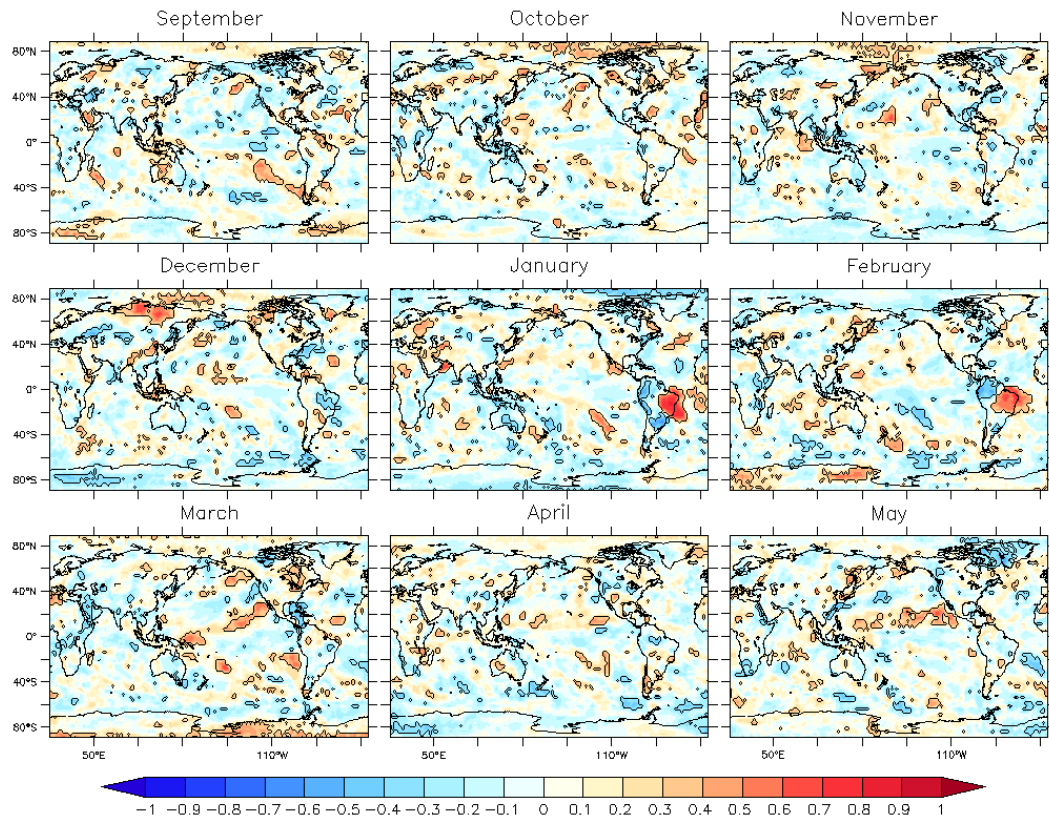


Figure C.1: Correlation maps of GPCP January-February EBPI index to monthly precipitation anomalies. Contours show areas where the correlations are significant at the 90% test level.

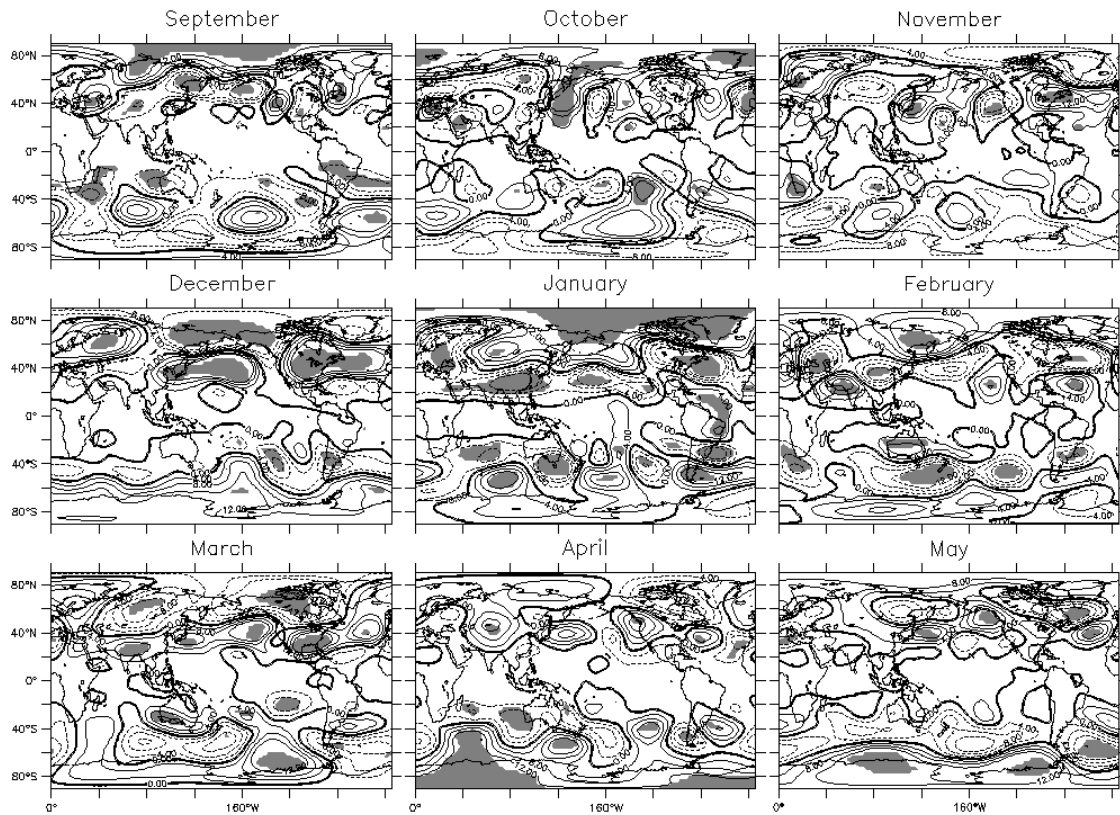


Figure C.2: Regression maps of GPCP January-February EBPI index to monthly 200mb geopotential height anomalies. Shading show areas where the correlations are significant at the 90% test level.

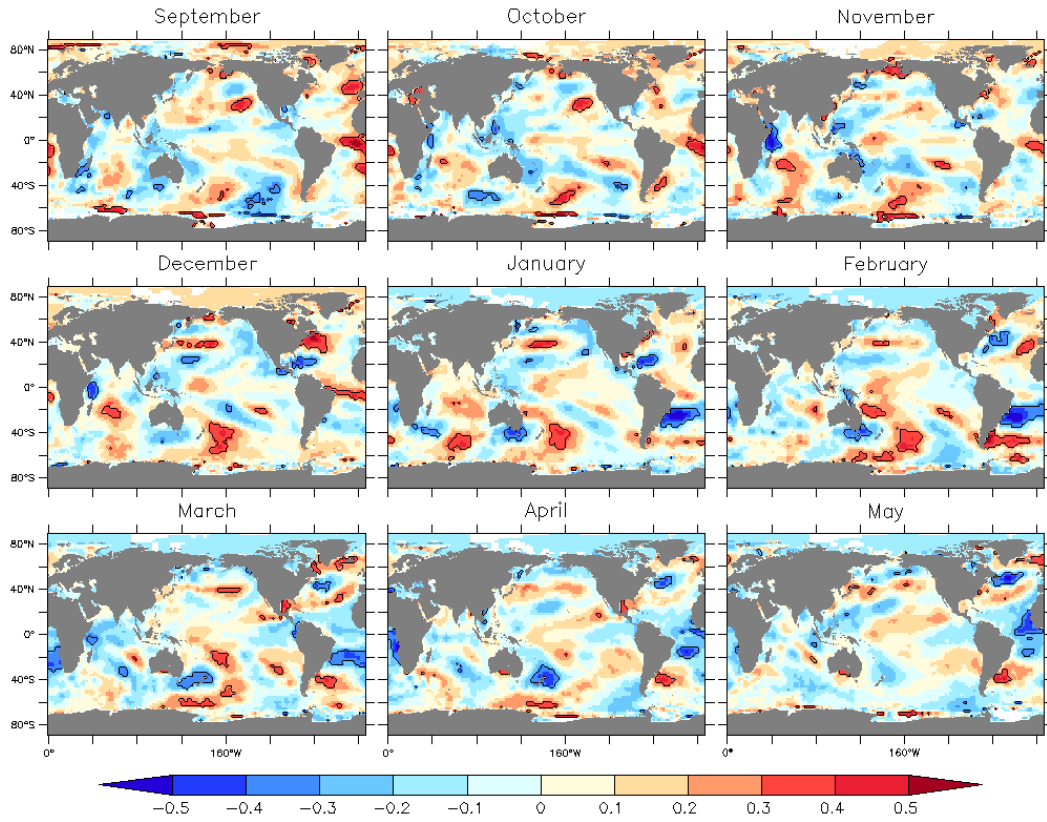


Figure C.3: Correlation maps of GPCP January-February EBPI index to monthly SST anomalies. Contours show areas where the correlations are significant at the 90% test level.

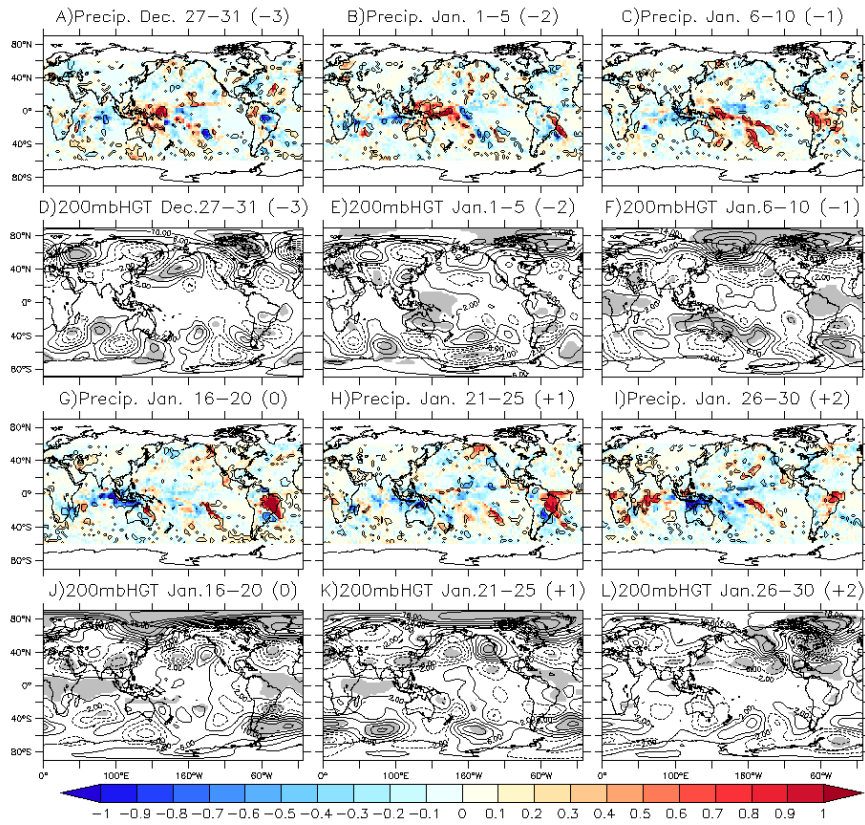


Figure C.4: Regression of the EBPI index calculated using only pentad 3, Jan 16-20 to precipitation and 200mb HGT anomalies. Contours in anomaly maps and shading in geopotential height maps show regions where the EBPI time series and the pertinent variable show correlations significant at the 90% significance level.

BIBLIOGRAPHY

- Patricio Aceituno. On the functioning of the southern oscillation in the south american sector. part ii. upper-air circulation. *J. Climate*, 2(4):341–355, April 1989. ISSN 0894-8755. URL [http://dx.doi.org/10.1175/1520-0442\(1989\)002<0341:OTFOTS>2.0.CO;2](http://dx.doi.org/10.1175/1520-0442(1989)002<0341:OTFOTS>2.0.CO;2).
- Robert F. Adler, George J. Huffman, Alfred Chang, Ralph Ferraro, Ping-Ping Xie, John Janowiak, Bruno Rudolf, Udo Schneider, Scott Curtis, David Bolvin, Arnold Gruber, Joel Susskind, Philip Arkin, and Eric Nelkin. The version-2 global precipitation climatology project (gpcp) monthly precipitation analysis (1979-present). *J. Hydrometeor*, 4(6):1147–1167, December 2003. ISSN 1525-755X. URL [http://dx.doi.org/10.1175/1525-7541\(2003\)004<1147:TVGPCP>2.0.CO;2](http://dx.doi.org/10.1175/1525-7541(2003)004<1147:TVGPCP>2.0.CO;2).
- Marcelo Barreiro, Ping Chang, and R. Saravanan. Variability of the south atlantic convergence zone simulated by an atmospheric general circulation model. *J. Climate*, 15(7):745–763, April 2002. ISSN 0894-8755. URL [http://dx.doi.org/10.1175/1520-0442\(2002\)015<0745:VOTSAC>2.0.CO;2](http://dx.doi.org/10.1175/1520-0442(2002)015<0745:VOTSAC>2.0.CO;2).
- Ernesto Hugo Berbery and Vicente R. Barros. The hydrologic cycle of the la plata basin in south america. *J. Hydrometeor*, 3(6):630–645, December 2002. ISSN 1525-755X. URL [http://dx.doi.org/10.1175/1525-7541\(2002\)003<0630:THCOTL>2.0.CO;2](http://dx.doi.org/10.1175/1525-7541(2002)003<0630:THCOTL>2.0.CO;2).
- Leila M. V. Carvalho, Charles Jones, and Brant Liebmann. Extreme precipitation events in southeastern south america and large-scale convective patterns in the south atlantic convergence zone. *J. Climate*, 15(17):2377–2394, September 2002. ISSN 0894-8755. URL [http://dx.doi.org/10.1175/1520-0442\(2002\)015<2377:EPEISS>2.0.CO;2](http://dx.doi.org/10.1175/1520-0442(2002)015<2377:EPEISS>2.0.CO;2).
- Leila M. V. Carvalho, Charles Jones, and Brant Liebmann. The south atlantic convergence zone: Intensity, form, persistence, and relationships with intraseasonal to interannual activity and extreme rainfall. *J. Climate*, 17(1):88–108, January 2004. ISSN 0894-8755. URL [http://dx.doi.org/10.1175/1520-0442\(2004\)017<0088:TSACZI>2.0.CO;2](http://dx.doi.org/10.1175/1520-0442(2004)017<0088:TSACZI>2.0.CO;2).

- Leila M. V. Carvalho, Charles Jones, Ana E. Silva, Brant Liebmann, and Pedro L. Silva Dias. The south american monsoon system and the 1970s climate transition. *International Journal of Climatology*, 31(8):1248–1256, 2011. ISSN 1097-0088. doi: 10.1002/joc.2147. URL <http://dx.doi.org/10.1002/joc.2147>.
- Christopher Alexander Castro Cunningham and Iracema Fonseca De Albuquerque Cavalcanti. Intraseasonal modes of variability affecting the south atlantic convergence zone. *International Journal of Climatology*, 26(9):1165–1180, 2006. ISSN 1097-0088. doi: 10.1002/joc.1309. URL <http://dx.doi.org/10.1002/joc.1309>.
- Iracema F. A. Cavalcanti, Jose A. Marengo, Prakki Satyamurty, Carlos A. Nobre, Igor Trosnikov, Jose Paulo Bonatti, Antonio Ocimar Manzi, Tatiana Tarasova, Luciano P. Pezzi, Cassiano DAlmeida, Gilvan Sampaio, Christopher C. Castro, Marcos B. Sanches, and Helio Camargo. Global climatological features in a simulation using the cptec cola agcm. *J. Climate*, 15(21):2965–2988, November 2002. ISSN 0894-8755. URL [http://dx.doi.org/10.1175/1520-0442\(2002\)015<2965:GCFIAS>2.0.CO;2](http://dx.doi.org/10.1175/1520-0442(2002)015<2965:GCFIAS>2.0.CO;2).
- Gabriel Cazes-Boezio, Andrew W. Robertson, and Carlos R. Mechoso. Seasonal dependence of enso teleconnections over south america and relationships with precipitation in uruguay. *J. Climate*, 16(8):1159–1176, April 2003. ISSN 0894-8755. URL [http://dx.doi.org/10.1175/1520-0442\(2003\)16<1159:SDOETO>2.0.CO;2](http://dx.doi.org/10.1175/1520-0442(2003)16<1159:SDOETO>2.0.CO;2).
- Rosane Rodrigues Chaves and Paulo Nobre. Interactions between sea surface temperature over the south atlantic ocean and the south atlantic convergence zone. *Geophys. Res. Lett.*, 31(3):L03204, February 2004. ISSN 0094-8276. URL <http://dx.doi.org/10.1029/2003GL018647>.
- Mingyue Chen, Pingping Xie, John E. Janowiak, and Phillip A. Arkin. Global land precipitation: A 50-yr monthly analysis based on gauge observations. *J. Hydrometeor*, 3(3):249–266, June 2002. ISSN 1525-755X. URL [http://dx.doi.org/10.1175/1525-7541\(2002\)003<0249:GLPAYM>2.0.CO;2](http://dx.doi.org/10.1175/1525-7541(2002)003<0249:GLPAYM>2.0.CO;2).

- Tsing-Chang Chen, Shu-Ping Weng, and Siegfried Schubert. Maintenance of austral summertime upper-tropospheric circulation over tropical south america: The bolivian high nordeste low system. *J. Atmos. Sci.*, 56(13):2081–2100, July 1999. ISSN 0022-4928. URL [http://dx.doi.org/10.1175/1520-0469\(1999\)056<2081:MOASUT>2.0.CO;2](http://dx.doi.org/10.1175/1520-0469(1999)056<2081:MOASUT>2.0.CO;2).
- W. Y. Chen. Fluctuations in northern hemisphere 700 mb height field associated with the southern oscillation. *Mon. Wea. Rev.*, 110(7):808–823, July 1982. ISSN 0027-0644. URL [http://dx.doi.org/10.1175/1520-0493\(1982\)110<0808:FINHMH>2.0.CO;2](http://dx.doi.org/10.1175/1520-0493(1982)110<0808:FINHMH>2.0.CO;2).
- Cristiano M. Chiessi, Stefan Mulitza, Jergen Patzold, Gerold Wefer, and Jose A. Marengo. Possible impact of the atlantic multidecadal oscillation on the south american summer monsoon. *Geophys. Res. Lett.*, 36(21):L21707–, November 2009. ISSN 0094-8276. URL <http://dx.doi.org/10.1029/2009GL039914>.
- Ana Elizabethe da Silva and Leila M. Vespoli de Carvalho. Large scale index for south america monsoon (lisam). *Atmospheric Science Letters*, 8(2):51–57, 2007. ISSN 1530-261X. doi: 10.1002/asl.150. URL <http://dx.doi.org/10.1002/asl.150>.
- Russ E. Davis. Predictability of sea surface temperature and sea level pressure anomalies over the north pacific ocean. *J. Phys. Oceanogr.*, 6(3):249–266, May 1976. ISSN 0022-3670. URL [http://dx.doi.org/10.1175/1520-0485\(1976\)006<0249:POSSTA>2.0.CO;2](http://dx.doi.org/10.1175/1520-0485(1976)006<0249:POSSTA>2.0.CO;2).
- Mark DeMaria. Linear response of a stratified tropical atmosphere to convective forcing. *J. Atmos. Sci.*, 42(18):1944–1959, September 1985. ISSN 0022-4928. URL [http://dx.doi.org/10.1175/1520-0469\(1985\)042<1944:LR0AST>2.0.CO;2](http://dx.doi.org/10.1175/1520-0469(1985)042<1944:LR0AST>2.0.CO;2).
- Moiria E. Doyle and Vicente R. Barros. Midsummer low-level circulation and precipitation in subtropical south america and related sea surface temperature anomalies in the south atlantic. *J. Climate*, 15(23):3394–3410, December 2002. ISSN 0894-8755. URL [http://dx.doi.org/10.1175/1520-0442\(2002\)015<3394:MLLCAP>2.0.CO;2](http://dx.doi.org/10.1175/1520-0442(2002)015<3394:MLLCAP>2.0.CO;2).

- Joshua D. Durkee and Thomas L. Mote. A climatology of warm-season mesoscale convective complexes in subtropical south america. *International Journal of Climatology*, 30(3):418–431, 2010. ISSN 1097-0088. doi: 10.1002/joc.1893. URL <http://dx.doi.org/10.1002/joc.1893>.
- Joshua D. Durkee, Thomas L. Mote, and J. Marshall Shepherd. The contribution of mesoscale convective complexes to rainfall across subtropical south america. *J. Climate*, 22(17):4590–4605, September 2009. ISSN 0894-8755. URL <http://dx.doi.org/10.1175/2009JCLI2858.1>.
- Rosana Nieto Ferreira, Thomas M. Rickenbach, Dirceu L. Herdies, and Leila M. V. Carvalho. Variability of south american convective cloud systems and tropospheric circulation during january march 1998 and 1999. *Mon. Wea. Rev.*, 131(5):961–973, May 2003. ISSN 0027-0644. URL [http://dx.doi.org/10.1175/1520-0493\(2003\)131<0961:VOSACC>2.0.CO;2](http://dx.doi.org/10.1175/1520-0493(2003)131<0961:VOSACC>2.0.CO;2).
- M. A. Gan, V. E. Kousky, and C. F. Ropelewski. The south america monsoon circulation and its relationship to rainfall over west-central brazil. *J. Climate*, 17(1):47–66, January 2004. ISSN 0894-8755. URL [http://dx.doi.org/10.1175/1520-0442\(2004\)017<0047:TSAMCA>2.0.CO;2](http://dx.doi.org/10.1175/1520-0442(2004)017<0047:TSAMCA>2.0.CO;2).
- Manoel A. Gan, Vadlamudi B. Rao, and Marley C. L. Moscati. South american monsoon indices. *Atmospheric Science Letters*, 6(4):219–223, 2005. ISSN 1530-261X. doi: 10.1002/asl.119. URL <http://dx.doi.org/10.1002/asl.119>.
- Norberto O. Garcia and Walter M. Vargas. The temporal climatic variability in the rio de la plata basin displayed by the river discharges. *Climatic Change*, 38:359–379, 1998. ISSN 0165-0009. URL <http://dx.doi.org/10.1023/A:1005386530866>.
- S. R. Garcia and M. T. Kayano. Climatological aspects of hadley, walker and monsoon circulations in two phases of the pacific decadal oscillation. *Theoretical and Applied*

- Climatology*, 91:117–127, 2008. ISSN 0177-798X. URL <http://dx.doi.org/10.1007/s00704-007-0301-9>. 10.1007/s00704-007-0301-9.
- Rene D. Garreaud. Intraseasonal variability of moisture and rainfall over the south american altiplano. *Mon. Wea. Rev.*, 128(9):3337–3346, September 2000. ISSN 0027-0644. URL [http://dx.doi.org/10.1175/1520-0493\(2000\)128<3337:IVOMAR>2.0.CO;2](http://dx.doi.org/10.1175/1520-0493(2000)128<3337:IVOMAR>2.0.CO;2).
- Rene D. Garreaud, Mathias Vuille, Rosa Compagnucci, and Jose Marengo. Present-day south american climate. *Palaeogeography, Palaeoclimatology, Palaeoecology*, 281(3-4):180–195, October 2009. ISSN 0031-0182. URL <http://www.sciencedirect.com/science/article/pii/S0031018208005002>.
- M. Gonzalez, C. Vera, B. Liebmann, J. marengo, V. Kousky, and D. Allured. The nature of the rainfall onset over central south america. *Atmosfera*, 20:379–396, 2007.
- Alice Grimm. Interannual climate variability in south america: impacts on seasonal precipitation, extreme events, and possible effects of climate change. *Stochastic Environmental Research and Risk Assessment*, 25:537–554, 2011. ISSN 1436-3240. URL <http://dx.doi.org/10.1007/s00477-010-0420-1>. 10.1007/s00477-010-0420-1.
- Alice M. Grimm. The el nino impact on the summer monsoon in brazil: Regional processes versus remote influences. *J. Climate*, 16(2):263–280, January 2003. ISSN 0894-8755. URL [http://dx.doi.org/10.1175/1520-0442\(2003\)016<0263:TENIOT>2.0.CO;2](http://dx.doi.org/10.1175/1520-0442(2003)016<0263:TENIOT>2.0.CO;2).
- Alice M. Grimm and Tercio Ambrizzi. Teleconnections into south america from the tropics and extratropics on interannual and intraseasonal timescales. In Françoise Vimeux, Florence Sylvestre, and Myriam Khodri, editors, *Past Climate Variability in South America and Surrounding Regions*, volume 14 of *Developments in Paleoenvironmental Research*, pages 159–191. Springer Netherlands, 2009. ISBN 978-90-481-2672-9. URL <http://dx.doi.org/10.1007/978-90-481-2672-9-7>.
- Alice M. Grimm and Renata G. Tedeschi. Enso and extreme rainfall events in south america.

- J. Climate*, 22(7):1589–1609, April 2009. ISSN 0894-8755. URL <http://dx.doi.org/10.1175/2008JCLI2429.1>.
- Alice M. Grimm and Marcia T. Zilli. Interannual variability and seasonal evolution of summer monsoon rainfall in south america. *J. Climate*, 22(9):2257–2275, May 2009. ISSN 0894-8755. URL <http://dx.doi.org/10.1175/2008JCLI2345.1>.
- Alice M. Grimm, Jeremy S. Pal, and Filippo Giorgi. Connection between spring conditions and peak summer monsoon rainfall in south america: Role of soil moisture, surface temperature, and topography in eastern brazil. *J. Climate*, 20(24):5929–5945, December 2007a. ISSN 0894-8755. URL <http://dx.doi.org/10.1175/2007JCLI1684.1>.
- A.M. Grimm. How do la nia events disturb the summer monsoon system in brazil? 22(2-3):123–138–, 2004. ISSN 0930-7575. URL <http://dx.doi.org/10.1007/s00382-003-0368-7>.
- A.M. Grimm, Vera C., and Mechoso R. *The Global Monsoon System: Research and Forecast*, chapter The South American Monsoon System, pages 219–238. WMO/TD - 1266, 2005.
- A.M. Grimm, M.T. Zilli, and I.F. Cavalcanti. Do seasonal forecasts reproduce the link between early and peak monsoon rainfall in south america? *CLIVAR Exchanges*, 12: 16–20, 2007b.
- G. J. Gutman and W. Schewerdtfeger. The role of latent and sensible heat for the development of a high pressure system over the subtropical andes in the summer. *Meteor. Rundsch.*, 18:69–75, 1965.
- Stefan Hastenrath and Leon Heller. Dynamics of climatic hazards in northeast brazil. *Q.J.R. Meteorol. Soc.*, 103(435):77–92, January 1977. ISSN 1477-870X. URL <http://dx.doi.org/10.1002/qj.49710343505>.
- Dirceu L. Herdies, Arlindo da Silva, Maria A. F. Silva Dias, and Rosana Nieto Ferreira. Moisture budget of the bimodal pattern of the summer circulation over south america.

- J. Geophys. Res.*, 107(D20):8075–, September 2002. ISSN 0148-0227. URL <http://dx.doi.org/10.1029/2001JD000997>.
- John D. Horel, Andrea N. Hahmann, and John E. Geisler. An investigation of the annual cycle of convective activity over the tropical americas. *J. Climate*, 2(11):1388–1403, November 1989. ISSN 0894-8755. URL [http://dx.doi.org/10.1175/1520-0442\(1989\)002<1388:AIOTAC>2.0.CO;2](http://dx.doi.org/10.1175/1520-0442(1989)002<1388:AIOTAC>2.0.CO;2).
- Charles Jones and Leila M. V. Carvalho. Active and break phases in the south american monsoon system. *J. Climate*, 15(8):905–914, April 2002. ISSN 0894-8755. URL [http://dx.doi.org/10.1175/1520-0442\(2002\)015<0905:AABPIT>2.0.CO;2](http://dx.doi.org/10.1175/1520-0442(2002)015<0905:AABPIT>2.0.CO;2).
- Charles Jones and Jae-Kyung E. Schemm. The influence of intraseasonal variations on medium- to extended-range weather forecasts over south america. *Mon. Wea. Rev.*, 128(2):486–494, February 2000. ISSN 0027-0644. URL <http://journals.ametsoc.org/doi/abs/10.1175/1520-0493%282000%29128%3C0486%3ATI0IV0%3E2.0.CO%3B2>.
- Charles Jones, Duane E. Waliser, K. M. Lau, and W. Stern. Global occurrences of extreme precipitation and the madden julian oscillation: Observations and predictability. *J. Climate*, 17(23):4575–4589, December 2004. ISSN 0894-8755. URL <http://dx.doi.org/10.1175/3238.1>.
- E. Kalnay, M. Kanamitsu, R. Kistler, W. Collins, D. Deaven, L. Gandin, M. Iredell, S. Saha, G. White, J. Woollen, Y. Zhu, A. Leetmaa, R. Reynolds, M. Chelliah, W. Ebisuzaki, W. Higgins, J. Janowiak, K. C. Mo, C. Ropelewski, J. Wang, Roy Jenne, and Dennis Joseph. The ncep/ncar 40-year reanalysis project. *Bull. Amer. Meteor. Soc.*, 77(3):437–471, March 1996. ISSN 0003-0007. URL [http://dx.doi.org/10.1175/1520-0477\(1996\)077<0437:TNYRP>2.0.CO;2](http://dx.doi.org/10.1175/1520-0477(1996)077<0437:TNYRP>2.0.CO;2).
- K.-Y. Kim. Investigation of enso variability using cyclostationary eofs of observational data. *Meteorology and Atmospheric Physics*, 81(3):149–168, 2002. ISSN 0177-7971. URL <http://dx.doi.org/10.1007/s00703-002-0549-7>.

- V.E. Kousky. Pentad outgoing longwave radiation climatology for the south american sector. *Revista Brasileira de Meteorologia*, 3:217–231, 1988.
- June-Yi Lee, Bin Wang, I.-S. Kang, J. Shukla, A. Kumar, J.-S. Kug, J.K.E. Schemm, J.-J. Luo, T. Yamagata, X. Fu, O. Alves, B. Stern, T. Rosati, and C.-K. Park. How are seasonal prediction skills related to models performance on mean state and annual cycle? *Climate Dynamics*, 35(2-3):267–283–, 2010. ISSN 0930-7575. URL <http://dx.doi.org/10.1007/s00382-010-0857-4>.
- J. D. Lenters and K. H. Cook. On the origin of the bolivian high and related circulation features of the south american climate. *J. Atmos. Sci.*, 54(5):656–678, March 1997. ISSN 0022-4928. URL [http://dx.doi.org/10.1175/1520-0469\(1997\)054<0656:OT00TB>2.0.CO;2](http://dx.doi.org/10.1175/1520-0469(1997)054<0656:OT00TB>2.0.CO;2).
- B. Liebmann and C.R. Mechoso. The south american monsoon system. In *The Global Monsoon System: Research and Forecast*, volume 5 of *World Scientific Series on Asia-Pacific Weather and Climate*. World Scientific Publication Company, 2nd edition, 2011.
- Brant Liebmann and Jose A. Marengo. Interannual variability of the rainy season and rainfall in the brazilian amazon basin. *J. Climate*, 14(22):4308–4318, November 2001. ISSN 0894-8755. URL [http://dx.doi.org/10.1175/1520-0442\(2001\)014<4308:IVOTRS>2.0.CO;2](http://dx.doi.org/10.1175/1520-0442(2001)014<4308:IVOTRS>2.0.CO;2).
- Brant Liebmann, George N. Kiladis, Carolina S. Vera, A. Celeste Saulo, and Leila M. V. Carvalho. Subseasonal variations of rainfall in south america in the vicinity of the low-level jet east of the andes and comparison to those in the south atlantic convergence zone. *J. Climate*, 17(19):3829–3842, October 2004. ISSN 0894-8755. URL [http://dx.doi.org/10.1175/1520-0442\(2004\)017<3829:SVORIS>2.0.CO;2](http://dx.doi.org/10.1175/1520-0442(2004)017<3829:SVORIS>2.0.CO;2).
- J. A. Marengo. Interdecadal variability and trends of rainfall across the amazon basin. *Theoretical and Applied Climatology*, 78:79–96, 2004. ISSN 0177-798X. URL <http://dx.doi.org/10.1007/s00704-004-0045-8>. 10.1007/s00704-004-0045-8.

- J. A. Marengo, B. Liebmann, A. M. Grimm, V. Misra, P. L. Silva Dias, I. F. A. Cavalcanti, L. M. V. Carvalho, E. H. Berbery, T. Ambrizzi, C. S. Vera, A. C. Saulo, J. Noguez-Paegle, E. Zipser, A. Seth, and L. M. Alves. Recent developments on the south american monsoon system. *International Journal of Climatology*, n/a:n/a–n/a, 2010. ISSN 1097-0088. doi: 10.1002/joc.2254. URL <http://dx.doi.org/10.1002/joc.2254>.
- Jose A. Marengo, Brant Liebmann, Vernon E. Kousky, Naziano P. Filizola, and Ilana C. Wainer. Onset and end of the rainy season in the brazilian amazon basin. *J. Climate*, 14(5):833–852, March 2001. ISSN 0894-8755. URL [http://dx.doi.org/10.1175/1520-0442\(2001\)014<0833:0AE0TR>2.0.CO;2](http://dx.doi.org/10.1175/1520-0442(2001)014<0833:0AE0TR>2.0.CO;2).
- Jose A. Marengo, Wagner R. Soares, Celeste Saulo, and Matilde Nicolini. Climatology of the low-level jet east of the andes as derived from the ncep near reanalyses: Characteristics and temporal variability. *J. Climate*, 17(12):2261–2280, June 2004. ISSN 0894-8755. URL [http://dx.doi.org/10.1175/1520-0442\(2004\)017<2261:COTLJE>2.0.CO;2](http://dx.doi.org/10.1175/1520-0442(2004)017<2261:COTLJE>2.0.CO;2).
- Vasubandhu Misra. Simulation of the intraseasonal variance of the south american summer monsoon. *Mon. Wea. Rev.*, 133(3):663–676, March 2005. ISSN 0027-0644. URL <http://dx.doi.org/10.1175/MWR-2877.1>.
- Vasubandhu Misra. Coupled air, sea, and land interactions of the south american monsoon. *J. Climate*, 21(23):6389–6403, December 2008. ISSN 0894-8755. URL <http://dx.doi.org/10.1175/2008JCLI2497.1>.
- Robinson I. Negron Juarez, Wenhong Li, Rong Fu, Katia Fernandes, and Andrea de Oliveira Cardoso. Comparison of precipitation datasets over the tropical south american and african continents. *J. Hydrometeorol*, 10(1):289–299, February 2009. ISSN 1525-755X. URL <http://dx.doi.org/10.1175/2008JHM1023.1>.
- Paulo Nobre and J. Shukla. Variations of sea surface temperature, wind stress, and rainfall over the tropical atlantic and south america. *J. Climate*, 9(10):2464–2479, October

1996. ISSN 0894-8755. URL [http://dx.doi.org/10.1175/1520-0442\(1996\)009<2464:VOSSTW>2.0.CO;2](http://dx.doi.org/10.1175/1520-0442(1996)009<2464:VOSSTW>2.0.CO;2).
- Julia Nogues-Paegle and Kingtse C. Mo. Alternating wet and dry conditions over south america during summer. *Mon. Wea. Rev.*, 125(2):279–291, February 1997. ISSN 0027-0644. URL [http://dx.doi.org/10.1175/1520-0493\(1997\)125<0279:AWADCO>2.0.CO;2](http://dx.doi.org/10.1175/1520-0493(1997)125<0279:AWADCO>2.0.CO;2).
- Gerald R. North, Thomas L. Bell, Robert F. Cahalan, and Fanthune J. Moeng. Sampling errors in the estimation of empirical orthogonal functions. *Mon. Wea. Rev.*, 110(7):699–706, July 1982. ISSN 0027-0644. URL [http://dx.doi.org/10.1175/1520-0493\(1982\)110<0699:SEITEO>2.0.CO;2](http://dx.doi.org/10.1175/1520-0493(1982)110<0699:SEITEO>2.0.CO;2).
- Julia N. Paegle and Kingtse C. Mo. Linkages between summer rainfall variability over south america and sea surface temperature anomalies. *J. Climate*, 15(12):1389–1407, June 2002. ISSN 0894-8755. URL [http://dx.doi.org/10.1175/1520-0442\(2002\)015<1389:LBSRV0>2.0.CO;2](http://dx.doi.org/10.1175/1520-0442(2002)015<1389:LBSRV0>2.0.CO;2).
- L. P. Pezzi and I. F. A. Cavalcanti. The relative importance of enso and tropical atlantic sea surface temperature anomalies for seasonal precipitation over south america: a numerical study. *Climate Dynamics*, 17(2):205–212, 2001-01-08. ISSN 0930-7575. URL <http://dx.doi.org/10.1007/s003820000104>.
- Ieda Pscheidt and Alice Marlene Grimm. Frequency of extreme rainfall events in southern brazil modulated by interannual and interdecadal variability. *International Journal of Climatology*, 29(13):1988–2011, 2009. ISSN 1097-0088. doi: 10.1002/joc.1799. URL <http://dx.doi.org/10.1002/joc.1799>.
- Adma Raia and Iracema Fonseca Albuquerque Cavalcanti. The life cycle of the south american monsoon system. *J. Climate*, 21(23):6227–6246, December 2008. ISSN 0894-8755. URL <http://dx.doi.org/10.1175/2008JCLI2249.1>.

- Gandikota V. Rao and Suat Erdogan. The atmospheric heat source over the bolivian plateau for a mean january. *Boundary-Layer Meteorology*, 46:13–33, 1989. ISSN 0006-8314. URL <http://dx.doi.org/10.1007/BF00118444>. 10.1007/BF00118444.
- Thomas M. Rickenbach, Rosana Nieto-Ferreira, Richard P. Barnhill, and Stephen W. Nesbitt. Regional contrast of mesoscale convective system structure prior to and during monsoon onset across south america. *J. Climate*, 24(14):3753–3763, February 2011. ISSN 0894-8755. URL <http://dx.doi.org/10.1175/2011JCLI3975.1>.
- Andrew W. Robertson and Carlos R. Mechoso. Interannual and interdecadal variability of the south atlantic convergence zone. *Mon. Wea. Rev.*, 128(8):2947–2957, August 2000. ISSN 0027-0644. URL [http://dx.doi.org/10.1175/1520-0493\(2000\)128<2947:IAIVOT>2.0.CO;2](http://dx.doi.org/10.1175/1520-0493(2000)128<2947:IAIVOT>2.0.CO;2).
- Andrew W. Robertson, John D. Farrara, and Carlos R. Mechoso. Simulations of the atmospheric response to south atlantic sea surface temperature anomalies. *J. Climate*, 16(15):2540–2551, August 2003. ISSN 0894-8755. URL <http://journals.ametsoc.org/doi/abs/10.1175/1520-0442%282003%29016%3C2540%3ASOTART%3E2.0.CO%3B2>.
- Daniel Andres Rodriguez and Iracema F. Albuquerque Cavalcanti. Simulations of the hydrological cycle over southern south america using the cptec cola agcm. *J. Hydrometeor*, 7(5):916–936, October 2006. ISSN 1525-755X. URL <http://dx.doi.org/10.1175/JHM534.1>.
- Josyane Ronchail, Gerard Cochonneau, Michel Molinier, Jean-Loup Guyot, Adriana Goretti De Miranda Chaves, Valdemar Guimaraes, and Eurides de Oliveira. Interannual rainfall variability in the amazon basin and sea-surface temperatures in the equatorial pacific and the tropical atlantic oceans. *International Journal of Climatology*, 22(13):1663–1686, 2002. ISSN 1097-0088. doi: 10.1002/joc.815. URL <http://dx.doi.org/10.1002/joc.815>.
- C. F. Ropelewski and M. S. Halpert. Global and regional scale precipitation patterns associated with the el nio/southern oscillation. *Mon. Wea. Rev.*, 115(8):1606–1626, August

1987. ISSN 0027-0644. URL [http://dx.doi.org/10.1175/1520-0493\(1987\)115<1606:GARSPP>2.0.CO;2](http://dx.doi.org/10.1175/1520-0493(1987)115<1606:GARSPP>2.0.CO;2).
- Prakki Satyamurty, Aline de Castro, Julio Tota, Lucia da Silva Gularte, and Antonio Manzi. Rainfall trends in the brazilian amazon basin in the past eight decades. *Theoretical and Applied Climatology*, 99:139–148, 2010. ISSN 0177-798X. URL <http://dx.doi.org/10.1007/s00704-009-0133-x>. 10.1007/s00704-009-0133-x.
- Gyrlene Silva, Anita Drumond, and Tercio Ambrizzi. The impact of el nino on south american summer climate during different phases of the pacific decadal oscillation. *Theoretical and Applied Climatology*, N/A:1–13, 2011. ISSN 0177-798X. URL <http://dx.doi.org/10.1007/s00704-011-0427-7>. 10.1007/s00704-011-0427-7.
- Viviane B. S. Silva and Ernesto H. Berbery. Intense rainfall events affecting the la plata basin. *J. Hydrometeor*, 7(4):769–787, August 2006. ISSN 1525-755X. URL <http://dx.doi.org/10.1175/JHM520.1>.
- Pedro L. Silva Dias, Wayne H. Schubert, and Mark DeMaria. Large-scale response of the tropical atmosphere to transient convection. *J. Atmos. Sci.*, 40(11):2689–2707, November 1983. ISSN 0022-4928. URL [http://dx.doi.org/10.1175/1520-0469\(1983\)040<2689:LSROTT>2.0.CO;2](http://dx.doi.org/10.1175/1520-0469(1983)040<2689:LSROTT>2.0.CO;2).
- Gabriel Silvestri and Carolina Vera. Nonstationary impacts of the southern annular mode on southern hemisphere climate. *J. Climate*, 22(22):6142–6148, November 2009. ISSN 0894-8755. URL <http://dx.doi.org/10.1175/2009JCLI3036.1>.
- Gabriel Silvestri, Carolina Vera, Daniela Jacob, Susanne Pfeifer, and Claas Teichmann. A high-resolution 43-year atmospheric hindcast for south america generated with the mpi regional model. *Climate Dynamics*, 32:693–709, 2009. ISSN 0930-7575. URL <http://dx.doi.org/10.1007/s00382-008-0423-5>. 10.1007/s00382-008-0423-5.
- Gabriel E. Silvestri and Carolina S. Vera. Antarctic oscillation signal on precipitation

- anomalies over southeastern south america. *Geophys. Res. Lett.*, 30(21):2115–, November 2003. ISSN 0094-8276. URL <http://dx.doi.org/10.1029/2003GL018277>.
- Thomas M. Smith and Richard W. Reynolds. Improved extended reconstruction of sst (1854-1997). *J. Climate*, 17(12):2466–2477, June 2004. ISSN 0894-8755. URL [http://dx.doi.org/10.1175/1520-0442\(2004\)017<2466:IEROS>2.0.CO;2](http://dx.doi.org/10.1175/1520-0442(2004)017<2466:IEROS>2.0.CO;2).
- Silvina Solman and Natalia Pessacg. Regional climate simulations over south america: sensitivity to model physics and to the treatment of lateral boundary conditions using the mm5 model. *Climate Dynamics*, N/A:1–20, 2011. ISSN 0930-7575. URL <http://dx.doi.org/10.1007/s00382-011-1049-6>. 10.1007/s00382-011-1049-6.
- Everaldo B. Souza, Tercio Ambrizzi, and Roger S. Pulwarty. The hadley and walker regional circulations and associated enso impacts on south american seasonal rainfall. In Henry F. Diaz and Raymond S. Bradley, editors, *The Hadley Circulation: Present, Past, and Future*, volume 21 of *Advances in Global Change Research*, pages 203–235. Springer Netherlands, 2004. ISBN 978-1-4020-2944-8. 10.1007/978-1-4020-2944-8-7.
- Liqiang Sun, David Ferran Moncunill, Huilan Li, Antonio Divino Moura, and Franciscode Assisde Souza Filho. Climate downscaling over nordeste, brazil, using the ncep rsm97. *J. Climate*, 18(4):551–567, February 2005. ISSN 0894-8755. URL <http://dx.doi.org/10.1175/JCLI-3266.1>.
- Cintia Bertacchi Uvo, Carlos A. Repelli, Stephen E. Zebiak, and Yochanan Kushnir. The relationships between tropical pacific and atlantic sst and northeast brazil monthly precipitation. *J. Climate*, 11(4):551–562, April 1998. ISSN 0894-8755. URL [http://dx.doi.org/10.1175/1520-0442\(1998\)011<0551:TRBTPA>2.0.CO;2](http://dx.doi.org/10.1175/1520-0442(1998)011<0551:TRBTPA>2.0.CO;2).
- C. Vera, J. Baez, M. Douglas, C. B. Emmanuel, J. Marengo, J. Meitin, M. Nicolini, J. Nogues-Paegle, J. Paegle, O. Penalba, P. Salio, C. Saulo, M. A. Silva Dias, P. Silva Dias, and E. Zipser. The south american low-level jet experiment. *Bull. Amer. Meteor.*

Soc., 87(1):63–77, January 2006. ISSN 0003-0007. URL <http://dx.doi.org/10.1175/BAMS-87-1-63>.

Carolina Vera and Gabriel Silvestri. Precipitation interannual variability in south america from the wcrp-cmip3 multi-model dataset. *Climate Dynamics*, 32:1003–1014, 2009. ISSN 0930-7575. URL <http://dx.doi.org/10.1007/s00382-009-0534-7>. 10.1007/s00382-009-0534-7.

Carolina Vera, Gabriel Silvestri, Vicente Barros, and Andrea Carril. Differences in el nino response over the southern hemisphere. *J. Climate*, 17(9):1741–1753, May 2004. ISSN 0894-8755. URL [http://dx.doi.org/10.1175/1520-0442\(2004\)017<1741:DIENRO>2.0.CO;2](http://dx.doi.org/10.1175/1520-0442(2004)017<1741:DIENRO>2.0.CO;2).

Bin Wang and Qinghua Ding. Global monsoon: Dominant mode of annual variation in the tropics. *Dynamics of Atmospheres and Oceans*, 44(34):165–183, March 2008. ISSN 0377-0265. URL <http://www.sciencedirect.com/science/article/pii/S0377026508000055>.

Bin Wang, June-Yi Lee, In-Sik Kang, J. Shukla, C.-K. Park, A. Kumar, J. Schemm, S. Cocke, J.-S. Kug, J.-J. Luo, T. Zhou, B. Wang, X. Fu, W.-T. Yun, O. Alves, E.K. Jin, J. Kinter, B. Kirtman, T. Krishnamurti, N.C. Lau, W. Lau, P. Liu, P. Pegion, T. Rosati, S. Schubert, W. Stern, M. Suarez, and T. Yamagata. Advance and prospectus of seasonal prediction: assessment of the apcc/clipas 14-model ensemble retrospective seasonal prediction (19802004). *Climate D*, 33(1):93–117–, 2009. ISSN 0930-7575. URL <http://dx.doi.org/10.1007/s00382-008-0460-0>.

Hui Wang and Rong Fu. Cross-equatorial flow and seasonal cycle of precipitation over south america. *J. Climate*, 15(13):1591–1608, July 2002. ISSN 0894-8755. URL [http://dx.doi.org/10.1175/1520-0442\(2002\)015<1591:CEFASC>2.0.CO;2](http://dx.doi.org/10.1175/1520-0442(2002)015<1591:CEFASC>2.0.CO;2).

Bryan C. Weare and John S. Nasstrom. Examples of extended empirical orthogonal function

- analyses. *Mon. Wea. Rev.*, 110(6):481–485, June 1982. ISSN 0027-0644. URL [http://dx.doi.org/10.1175/1520-0493\(1982\)110<0481:E0EE0F>2.0.CO;2](http://dx.doi.org/10.1175/1520-0493(1982)110<0481:E0EE0F>2.0.CO;2).
- A. Weisheimer, F. J. Doblas-Reyes, T. N. Palmer, A. Alessandri, A. Arribas, M. Dqu, N. Keenlyside, M. MacVean, A. Navarra, and P. Rogel. Ensembles: A new multi-model ensemble for seasonal-to-annual predictions-skill and progress beyond demeter in forecasting tropical pacific ssts. *Geophys. Res. Lett.*, 36(21):L21711–, November 2009. ISSN 0094-8276. URL <http://dx.doi.org/10.1029/2009GL040896>.
- Pingping Xie and Phillip A. Arkin. Global precipitation: A 17-year monthly analysis based on gauge observations, satellite estimates, and numerical model outputs. *Bull. Amer. Meteor. Soc.*, 78(11):2539–2558, November 1997. ISSN 0003-0007. URL [http://dx.doi.org/10.1175/1520-0477\(1997\)078<2539:GPAYMA>2.0.CO;2](http://dx.doi.org/10.1175/1520-0477(1997)078<2539:GPAYMA>2.0.CO;2).
- Xungang Yin, Arnold Gruber, and Phil Arkin. Comparison of the gpcp and cmap merged gaugesatellite monthly precipitation products for the period 19792001. *J. Hydrometeor.*, 5(6):1207–1222, December 2004. ISSN 1525-755X. URL <http://dx.doi.org/10.1175/JHM-392.1>.
- Laura Zamboni, Carlos R. Mechoso, and Fred Kucharski. Relationships between upper-level circulation over south america and rainfall over southeastern south america: A physical base for seasonal predictions. *J. Climate*, 23(12):3300–3315, December 2009. ISSN 0894-8755. URL <http://dx.doi.org/10.1175/2009JCLI3129.1>.
- Laura Zamboni, Fred Kucharski, and C. Mechoso. Seasonal variations of the links between the interannual variability of south america and the south pacific. *Climate Dynamics*, pages 1–15, 2011. ISSN 0930-7575. URL <http://dx.doi.org/10.1007/s00382-011-1116-z>.
- Jiayu Zhou and K-M. Lau. Does a monsoon climate exist over south america? *J. Climate*, 11(5):1020–1040, May 1998. ISSN 0894-8755. URL [http://dx.doi.org/10.1175/1520-0442\(1998\)011<1020:DAMCEO>2.0.CO;2](http://dx.doi.org/10.1175/1520-0442(1998)011<1020:DAMCEO>2.0.CO;2).

Jiayu Zhou and K.-M. Lau. Principal modes of interannual and decadal variability of summer rainfall over south america. *International Journal of Climatology*, 21(13):1623–1644, 2001. ISSN 1097-0088. doi: 10.1002/joc.700. URL <http://dx.doi.org/10.1002/joc.700>.

E. J. Zipser, Chuntao Liu, Daniel J. Cecil, Stephen W. Nesbitt, and David P. Yorty. Where are the most intense thunderstorms on earth? *Bull. Amer. Meteor. Soc.*, 87(8):1057–1071, August 2006. ISSN 0003-0007. URL <http://dx.doi.org/10.1175/BAMS-87-8-1057>.